Theoretical investigation of Rare-Earth doped optical materials

Optimization and Prediction

Mirzai, Amin

2023

Theoretical investigation of Rare-Earth doped optical materials

Theoretical investigation of Rare-Earth doped optical materials

Optimization and Prediction

by Amin Mirzai

LUND
UNIVERSITY

Thesis for Doctor of Philosophy
Thesis advisors: Prof. Aylin Ahadi
Faculty opponent: Prof. Layla Martin-Samos

To be presented, with the permission of the Faculty of Engineering of Lund University, for public criticism in the M:E lecture hall at the Department of Mechanical Engineering Sciences on Friday, the 17th of November 2023 at 09:00.

Organization	Document name
LUND UNIVERSITY Department of Mechanical Engineering Sciences Box 118, SE-22100 Lund, Sweden	**DOCTORAL DISSERTATION** Date of disputation 2023 - 11 - 17 Sponsoring organization

Author
Amin Mirzai

Title and subtitle
Theoretical investigation of Rare-Earth doped optical materials

Abstract

Rare-earth (RE) doped optical materials are distinguished by their unique optical and electronic properties. These characteristics are essential for various applications, including laser stabilization, and phosphors. However, the sensitivity of these materials to environmental factors and intrinsic defects necessitates a deep understanding. Grasping how these factors influence the refractive index, absorption coefficient, and emission spectra is vital.

This thesis delves into the effects of external loads on substitutional defects in laser host materials. We employ both first principles and additional theoretical methods for our investigations. While we cover materials from both the Orthosilicates and Orthovanadate categories, we place special emphasis on Y_2SiO_5 (YSO). This is due to its rising significance in applications like laser stabilization and quantum memory.

Our discussion is split into two primary sections: ground-state and excited-state properties. In the ground-state section, we introduce a framework to comprehend variations in an optical cavity's optical path. This is especially relevant when the refractive index changes because of mechanical stress, affecting its resonance frequency. Through this lens, we explore the inherent properties of Eu-doped YSO. Our insights span its mechanical and thermodynamic properties, leading us to a multi-scale approach. Our understanding extends to the effects of temperature and pressure, resulting in the identification of two essential ratios: dn/dP and dn/dT. These are vital for RE-doped YSO laser applications.

For the excited-state properties, our focus shifts to the transition energy of the RE dopant within the host material. Current methods for studying the excitation of RE ions in these materials often encounter issues such as extensive computational demands and dependence on empirical data. We underline that techniques like GW+BSE and AIMPs aren't universally applicable to all RE-doped materials. Instead, we advocate for the use of constrained DFT (cDFT), combined with hybrid DFT and spin-orbit coupling (SOC). This method pinpoints the 4f ground state position with less dependence on empirical data, offering a more efficient alternative to the Dorenbos model. It promises the potential to unveil new phosphors and provides a comprehensive analysis of RE-doped laser materials.

Keywords
Rare-Earth, DFT, cDFT, refractive index, multi-scale modeling, optical path length, RE-activated phosphor

Classification system and/or index terms (if any)

Supplementary bibliographical information	Language
	English
ISSN and key title	ISBN
	978-91-8039-849-7 (print) 978-91-8039-850-3 (pdf)
Recipient's notes	Number of pages: 152 / Price
	Security classification

Theoretical investigation of Rare-Earth doped optical materials

Optimization and Prediction

by Amin Mirzai

LUND
UNIVERSITY

A doctoral thesis at a university in Sweden takes either the form of a single, cohesive research study (monograph) or a summary of research papers (compilation thesis), which the doctoral student has written alone or together with one or several other author(s).

In the latter case the thesis consists of two parts. An introductory text puts the research work into context and summarizes the main points of the papers. Then, the research publications themselves are reproduced, together with a description of the individual contributions of the authors. The research papers may either have been already published or are manuscripts at various stages (in press, submitted, or in draft).

Funding information: Wallenberg Foundation

Faculty of Engineering, Department of Mechanical Engineering Sciences

ISBN: 978-91-8039-849-7 (print)
ISBN: 978-91-8039-850-3 (pdf)

Printed in Sweden by Media-Tryck, Lund University, Lund 2023

Dedicated to my parents
Havva — Fazel

Contents

List of publications

I **First-principle investigation of doping effects on mechanical and thermodynamic properties of Y_2SiO_5**
Amin Mirzai, Aylin Ahadi, Solveig Melin, P.A.T Olsson
Mechanics of Materials

II **A theoretical investigation of optical path length variation of Eu:Y_2SiO_5 (Submitted)**
Amin Mirzai, Aylin Ahadi
Optics Express

III **Influence of impurity configuration on electronic and optical properties of Ce-doped YVO_4: Semi-local & Hybrid functionals**
Amin Mirzai, Aylin Ahadi, Solveig Melin
Computational Materials Science

IV **First-principles study of luminescence and electronic properties of Ce-doped Y_2SiO_5**
Amin Mirzai, Aylin Ahadi
The Journal of Chemical Physics

Publications not included in this thesis:

Photoelasticity of YVO_4 through first-principles calculation

Amin Mirzai, Aylin Ahadi and Solveig Melin
Journal for SCIPEDIA

The concentration of gold in gold-catalysed GaAs nanowires (in manuscript)
Jonas Johansson, Amin Mirzai

List of Acronyms

TDDFT Time-dependent density functional theory 22

US Ultrasoft 15

VASP Vienna Ab initio Simulation Package 5

VBM Valence band maximum 48

XC Exchange-Correlation 10

List of Symbols

ν_m	Average sound velocity See Table 1 in section 4.
k_b	Boltzmann's constant
B	Bulk modulus
E_c	Correlation energy
θ_D	Debye temperature
ρ	Density See Table 1 in section 4.
$\epsilon(\omega)$	Dielectric function
B	Dielectric impermeability matrix
e	Electron charge
n(r)	Electron density
V_{ei}	Electron-ion attractive interactions
V_{ee}	Electron-electron repulsive interactions
ε_0	Exact energy
E_{xc}	Exchange-correlation energy
ν_{xc}	Exchange-correlation potential
ν_{ext}	External potential
n_e	Extraordinary refractive index
f	Frequency
R	Gas constant
γ	Grüneisen parameter
H	Hamiltonian
ν_H	Hartree potential
E_{HF}	Hartree-Fock energy
Z_I	Ionic charge
R_I	Ion coordinate
T	Kinetic energy
ν_l	Longitudinal sound velocity See Table 1 in section 4.
m	Mode number
N	Number of particles
G	One-body Green's function
n_o	Ordinary refractive index
L	Physical length
ν	Poisson ratio
α	Portion of exact exchange

G	Reciprocal lattice vector
$\hbar$	Reduced Planck's constant
n	Refractive index
C_ν	Specific heat at constant volume
C_p	Specific heat at constant pressure
c	Speed of light
μ	Screening parameter
ϕ_i	Single particle orbitals
G	Shear modulus
T	Temperature
ν_{KS}	The effective KS potential
κ_{min}	The minimum thermal conductivity
W	The dynamically screened Coulomb interaction
ν_t	Transverse sound velocity See Table 1 in section 4.
Ψ	Wave function
λ	Wavelength
k	Wave vector

There are more symbols in the text whose definitions are given once they are introduced.

Acknowledgements

First and foremost, I would like to extend my gratitude to my supervisors Professor Aylin Ahadi and Professor Solveig Melin for granting me the privilege to pursue this Ph.D. Additionally, I am thankful to Associate Professor Pär Olsson and Professor Dmytro Orlov for their guidance and support during challenging times.

I want to thank my office mates and other colleagues for the cherished moments we shared. I would like to thank specifically Dr. Rikard Hjelm for his help with the last stages of my Ph.D.

Last but not least, I owe a heartfelt thank you to my family for their unwavering mental support over the years, with special mention to my parents.

Popular summary in English

Historically, the earliest known lenses, crafted from polished crystal, notably quartz, trace their roots back to 2000 BC from Crete. The Greeks and Romans advanced these tools by filling glass spheres with water and creating rudimentary lenses. These ancient innovations underscore the significance of optical materials in the world's evolution.

Over the years, the definition and scope of optical materials have expanded. This growth is largely attributed to IT advancements, which, in turn, have fostered rapid growth in optoelectronics applications. Optical materials, as understood today, span a broad spectrum, encompassing traditional principles as well as cutting-edge topics. They form the backbone for technologies ranging from ultraviolet, visible, infrared, non-linear optics, solid-state lasers, optical waveguides, and optical thin films, to nanophotonics.

The journey from the ancient lenses of Crete to today's advanced optical materials was shaped by numerous techniques and methods. Geometric optics, one of the foundational models, regarded light as rays that travel straight and bend when interacting with surfaces. While this model simplified many phenomena, it was soon evident that to account for wave effects like diffraction and interference, a more comprehensive model was needed. Thus, physical optics emerged.

Furthermore, the 19th-century progress in electromagnetic theory unveiled that light waves were essentially electromagnetic radiation. This shifted the paradigm and further expanded our understanding. Yet, certain phenomena required an understanding of light's wave-like and particle-like properties, leading to the inception of quantum optics, which integrates quantum mechanics with optical systems.

Today, quantum optics which involves with optimization of optical materials is important for applications such as laser stabilization and quantum information, as it can improve the performance and functionality of these technologies. Optimization of optical materials can involve designing new materials with desired optical properties or modifying existing materials with external stimuli or processes. Optimization of optical materials can also involve developing new fabrication methods or characterization techniques that can produce high-quality optical devices or systems. Optimization of optical materials is an active area of research that involves interdisciplinary collaboration among physics, chemistry, engineering, biology, and medicine.

The extensive applications and complexities surrounding optical materials necessitate a robust theoretical approach. Theory plays a pivotal role in the discovery and optimization of optical materials for various reasons:

- **Predictive Capabilities:** Theoretical approaches enable scientists to predict how materials might behave under certain conditions, thereby aiding in the design and tailoring of materials for specific applications.
- **Efficiency:** Through theory, we can simulate scenarios, test hypotheses, and optimize material properties without extensive physical testing, saving both time and resources.
- **Advanced Applications:** Theoretical insights drive innovation. By understanding materials at a fundamental level, we can engineer them for advanced applications, be it in nanophotonics or optoelectronics, to name a few.
- **Foundation for Future Innovations:** A solid theoretical grounding ensures that as the field evolves, newer models and theories can be built upon established ones. This continuum of knowledge fosters rapid advancements and technological innovations.

Among theoretical approaches first-principles calculations, especially those based on density functional theory (DFT), are invaluable in comprehending the atomistic characteristics of materials. They provide insights into the linear optical response of materials, which is essential for many optical applications. The advancement in computational methods is continually pushing the boundaries and providing even more precise and comprehensive insights into the optical behaviors of various materials.

The aim of this work is to enhance the existing knowledge of certain optical materials and to develop a framework and methods that could facilitate the optimization and discovery of a new class of optical materials. To achieve this goal, this work focuses on theoretical methods that can advance our understanding of the optical properties and behaviors of these materials. This can enable the creation of new types of optical materials or the improvement of the performance and functionality of existing optical devices and instruments by providing further in-depth knowledge of their intrinsic properties.

Populärvetenskaplig sammanfattning på svenska

Historiskt sett kan de tidigaste kända linserna, tillverkade av polerad kristall, särskilt kvarts, spåra sina rötter tillbaka till 2000 f.Kr. på Kreta. Grekerna och romarna förbättrade dessa produkter genom att fylla glassfärer med vatten, vilket skapade grundläggande linser. Dessa gamla innovationer betonar betydelsen av optiska material i världens utveckling.

Över åren har definitionen och omfattningen av optiska material utvidgats. Denna tillväxt tillskrivs i stor utsträckning IT-tekniker, vilket i sin tur har främjat snabb tillväxt inom optoelektroniska tillämpningar. Optiska material, som de förstås idag, spänner över ett brett spektrum, och omfattar traditionella principer såväl som banbrytande ämnen. De utgör grunden för teknik som sträcker sig från ultraviolett, synligt, infrarött, icke-linjär optik, till fasta tillståndslasrar, optiska vågledare, optiska tunna filmer till nanofotonik.

Resan från de antika linserna på Kreta till dagens avancerade optiska material formades genom många tekniker och metoder. Geometrisk optik, en av de grundläggande modellerna, betraktade ljus som strålar som reser rakt och böjer sig när de interagerar med ytor. Även om denna modell förenklade många fenomen blev det snart uppenbart att för att ta hänsyn till vågeffekter som diffraktion och interferens behövdes en mer omfattande modell. Så uppstod fysisk optik.

Dessutom avslöjade 1800-talets framsteg inom elektromagnetisk teori att ljusvågor i grunden var elektromagnetisk strålning. Detta ändrade paradigmet och utökade ytterligare vår förståelse. Ändå krävde vissa fenomen en förståelse för ljusets vågliknande och partikelliknande egenskaper, vilket ledde till uppkomsten av kvantoptik, som integrerar kvantmekanik med optiska system.

Idag är kvantoptik som involverar optimering av optiska material viktigt för tillämpningar som laserstabilisering och kvantinformation, eftersom det kan förbättra prestanda och funktionalitet för dessa teknologier. Optimering av optiska material kan innebära att designa nya material med önskade optiska egenskaper eller att ändra befintliga material med externa stimuli eller processer. Optimering av optiska material kan också innebära utveckling av nya framställningsmetoder eller karaktäriseringstekniker som kan producera högkvalitativa optiska enheter eller system. Optimering av optiska material är ett aktivt forskningsområde som involverar tvärvetenskapligt samarbete mellan fysik, kemi, teknik, biologi och medicin.

De omfattande tillämpningarna och komplexiteten kring optiska material kräver

ett robust teoretiskt tillvägagångssätt. Teorin spelar en central roll i upptäckten och optimeringen av optiska material av flera skäl:

De tidigast kända linserna var tillverkade av polerad kristall, särskilt kvarts. Rötterna går att spåra tillbaka till 2000 f.kr. på Kreta. Grekerna och romarna förbättrade verktygen genom att fylla glassfärer med vatten, vilket skapade grundläggande linser. Dessa gamla innovationer betonar betydelsen av optiska material i världens utveckling.

- **Prediktivitet:** Teoretiska metoder gör det möjligt för forskare att förutsäga hur material kan bete sig under vissa förhållanden, vilket hjälper till att designa och anpassa material för specifika tillämpningar.
- **Effektivitet:** Genom teori kan vi simulera scenarier, testa hypoteser och optimera materialens egenskaper utan omfattande fysisk testning, vilket sparar både tid och resurser.
- **Avancerade tillämpningar:** Teoretiska insikter driver innovation. Genom att förstå material på en grundläggande nivå kan vi konstruera dem för avancerade tillämpningar, vare sig det är inom nanofotonik eller optoelektronik, för att nämna några.
- **Grunden för framtida innovationer:** En solid teoretisk grund gör att när fältet utvecklas kan nya modeller och teorier byggas på etablerade. Denna kunskapskontinuitet främjar snabba framsteg och teknologiska innovationer.

Bland teoretiska metoder är first-principles-beräkningar, särskilt de baserade på densitetsfunktionsteori (DFT), ovärderliga för att förstå materialens atomistiska egenskaper. De ger insikt i materialens linjära optiska respons, vilket är väsentligt för många optiska tillämpningar. Framstegen inom beräkningsmetoder fortsätter att flytta gränserna och ge ännu mer precisa och omfattande insikter i de optiska beteendena hos olika material.

Syftet med detta arbete är att förbättra den befintliga kunskapen om vissa optiska material och att utveckla ett ramverk och metoder som kan underlätta optimeringen och upptäckten av en ny klass av optiska material. För att uppnå detta mål fokuserar föreliggande arbete på teoretiska metoder som kan förbättra vår förståelse för de optiska egenskaperna och beteendena hos sådana material och kan möjliggöra skapandet av nya.

1 Introduction

1.1 Optical materials

Optical materials are a type of material used in optics that have distinct characteristics and applications due to their unique crystalline structures [1]. They find extensive application in the construction of various optical components such as lenses, prisms, beam splitters [2], and filters [3], and serve as integral elements in laser systems [4]. One of their distinctive property is birefringence, where the crystal exhibits double refraction, causing light rays to split into two distinct paths. Additionally, they possess high refractive indices, meaning that they can significantly bend light, thereby influencing the optical path and the system's focus. Furthermore, optical materials display nonlinear optical behavior, a feature that allows light waves to interact in complex and beneficial ways. For example, they can convert the frequency of light, combine light beams, or generate controlled light pulses. Such unique capabilities make optical materials indispensable for the functioning and optimization of a myriad of optical devices and systems.

Doping crystals with Rare Earth (RE) ions is a common practice to modify and enhance certain properties. Doping occurs when one type of atom or ion is replaced by a different atom or ion in the crystal lattice. The schematic picture of this process is shown in Figure 1. The new atom or ion, known as a substitutional impurity, may have a different size, charge, or electron configuration than the atom it replaces, thereby altering the crystal's properties. These changes can substantially impact the optical and physical characteristics of the crystal, modifying properties such as refractive index, and structural integrity [5, 6]. Doping can also affect the luminescence properties of optical materials. Luminescence is the emission of light by a material (Figure 2) in response to excitation by an external energy source, such as light or heat. When a substitutional defect occurs, it can create localized energy states within the crystal lattice, which can modify the luminescence properties of the material [7, 8]. For example, the introduction of a substitutional defect can change the color or intensity of the emitted light, or shift the emission spectrum to a different wavelength [9]. This effect can be exploited for applications such as solid-state lighting and color displays. In addition, substitutional defects can alter the mechanical and thermal properties of optical materials. For example, the introduction of a substitutional defect can increase or decrease the material's hardness or thermal conductivity,

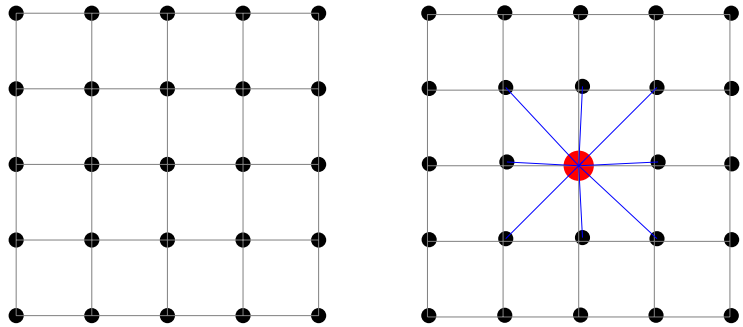

Figure 1: Schematic view of the substitutional defect. Note how the impurity atom displaces the neighboring atoms.

which can affect its durability and heat dissipation properties. This effect can be important for applications such as laser optics and thermal management. Despite some risks, intentionally introduced impurities can enhance certain attributes of optical materials and potentially offer new functionalities for diverse applications [10].

The RE ions, for instance, fall under the category of intentional dopants. Their unique electron configurations lead to sharp, well-defined energy levels and make them suitable as phosphors and scintillators for lighting, imaging, and sensing applications [11, 12, 13, 14]. Moreover, these materials are advantageous for quantum computing, quantum cryptography, and mapping quantum information, largely due to the long coherence lifetimes enabled by the unique properties of RE ions [15]. The unique properties of rare earth ions, attributable to their partially filled 4f shell and shielding effects, enable them to be used in materials with long coherence lifetimes. Coherence lifetime, an essential factor in quantum information science, is however limited by the excited-state lifetime [15]. To optimize the functionality of rare-earth materials in quantum information applications, technologies such as laser sources and detectors with narrow line widths and high stability are vital. Furthermore, RE-doped materials are utilized for frequency and phase stabilization of laser sources in quantum information [16]. Lastly, Trivalent rare earth ions, in particular, exhibit fascinating optical properties and are suitable for various applications, including the development of luminescent materials and other specialized optical components due to their interaction with light and potential in bio-detection [17].

The optical characteristics of these doped crystals are subject to variations and noise stemming from numerous factors, which might potentially influence their performance. For instance, the concentration of RE ions within the crystal may vary its optical properties [18, 19]. Inconsistencies in these properties may arise

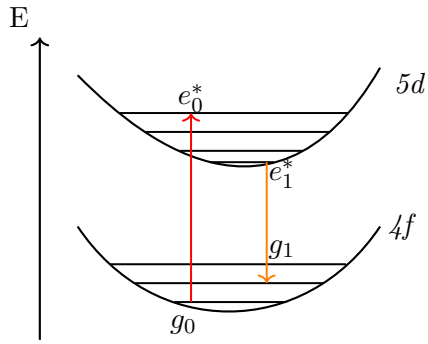

Figure 2: Schematic description of excitation and emission in a RE-doped phosphor.

due to imperfections in the crystal lattice, such as impurities, vacancies, or dislocations, resulting in localized refractive index changes. Moreover, fluctuations in temperature can induce alterations in the optical material's refractive index [20], thermal expansion [21], and thermo-optic coefficients [22]. Such thermal changes could lead to variations in the optical path length [23] and cause wavefront distortions. These factors collectively underscore the need for meticulous control and management in the manufacturing and handling of these doped crystals to ensure their optimal performance. Additionally, mechanical stress can induce changes in the refractive index through the photoelastic effect [24], giving rise to birefringence, polarization alterations, and other stress-related optical phenomena that can impair the performance of the optical system. For example, it can influence the energy levels of the ions in the crystal, and thereby affect the absorption and emission characteristics [25].

Given these complexities, it becomes imperative to understand how doping and mechanical stress modify the intrinsic properties of RE-doped crystals. This understanding is crucial for optimizing their performance and maximizing their utility across various applications.

1.2 Objectives of this work

This study aims to formulate theoretical models that predict and describe the qualities of emerging optical materials, enhancing their role in optoelectronic devices. These models primarily harness theoretical methodologies to deepen comprehension of these materials' optical traits. Such insights could potentially foster the inception of innovative optical materials or augment the efficacy of existing devices, emphasizing intrinsic attributes over empirical evidence.

Our research predominantly focuses on Y_2SiO_5, a widely recognized optical material often doped with RE ions for various purposes. Additionally, YVO_4, which is also a popular laser medium optical material is studied mainly due to its popularity and existing experimental data. We mainly address two attributes in these materials: refractive index and RE-activated transitions. For the former, we intend to monitor and forecast how the material responds to mechanical or thermodynamical stress. Such insights can refine device optimization. Meanwhile, for the latter, our aim is to develop a model that becomes standard for the identification of RE-doped materials, particularly in phosphor applications.

2 Fundamentals of density functional theory

The Density Functional Theory (DFT) is widely used as the main tool in the study of materials so much so that today there is a field of study known as computational material science, and the key tool for this field is DFT. All the quantum calculations in this thesis are carried out in the Vienna Ab initio Simulation Package (VASP) [26] and CRYSTAL [27] packages in which VASP utilizes plane-wave approach while the CRYSTAL is based on the expansion of Gaussian type basis set to reproduce the necessary wave functions. Consequently, this chapter is aimed to provide essential background and understanding of such approaches.

2.1 Density Functional Theory

Since the advent of the DFT method in the early 60s, many applications and spin-offs have been created, and it has consistently proven to be a reliable addition to the toolbox of physicists, chemists, and especially material scientists. Here, a brief introduction about this theory is added to build a foundation of the further methods that actually help us to conduct the necessary calculations for this thesis.

The motion and interaction of electrons in their respective ground state in a solid can be described by the many-body Schrödinger equation.

$$H\Psi_i(r_1, r_2, ..., r_N) = E_i\Psi_i(r_1, r_2, ..., r_N) \tag{1}$$

where Ψ_i is the wave function with energy E_i, and r_i is the coordinate of electron i. The non-relativistic many-body Hamiltonian can be decomposed into three terms as follows

$$H = T + V_{ee} + V_{ei} \tag{2}$$

where T is the kinetic energy

$$T = -\frac{\hbar^2}{2m}\sum_{i=1}^{N}\nabla^2 \tag{3}$$

and V_{ee} is the electron-electron repulsive interactions

$$V_{ee} = \frac{1}{2}\sum_{i\neq j}\frac{e^2}{|r_i - r_j|} \tag{4}$$

and V_{ei} is the electron-ion attractive interactions (Z_I is the ionic charge and R_I is the coordinate of ions)

$$V_{ei} = \sum_i V_{ion}(r_i) = -\sum_{iI} \frac{Z_I e^2}{|r_i - R_I|} = \sum_{i=1}^{N} \nu(r_i) \tag{5}$$

Note that in the provided Hamiltonian only the last term contains information about interaction with the nucleus. This is mainly due to the mass difference between electrons and nuclei, even the lightest nuclei weigh more or less 1800 times more than an electron, and the motion of the nucleus is considered to be stationary relative to electrons. As a result, the Hamiltonian can be simplified to only consider the terms related to electrons and the static charge between electrons and the nucleus. This simplification is known as Born-Oppenheimer approximation [28].

If we refer back to Equation 1, the purpose of solving many-body Schrödinger equation is to obtain the eigenfunctions ψ_i and their corresponding eigenvalues E_i. However, solving it exactly except for the Hydrogen atoms is a near impossible task as the complexity of such a task scales up exponentially, and the fact that for the problems with more than one electron a many-body approach is required. Therefore, it is necessary to employ approximation methods to simplify the task. The most widely used approach is the independent-electron approximation which essentially assumes that electrons move independently in an effective potential created by all other electrons. Consequently, the many-body problem is reduced to a single-particle problem. Although there are a few methods to tackle single-particle problems, the main two approaches are:

- Wave function-based methods: The coroner-stone of this approach is Hartree-Fock approximation
- Density-based methods: DFT.

Even though the main focus of this thesis is on the usage of the DFT approach, the wave function approach is important to grasp the physical picture behind the machinery of all quantum mechanical approaches. Thus, I will briefly introduce the Hartree-Fock (HF) approach, which would help to better understand the DFT method.

2.2 Hartree-Fock Approximation

According to Hartree product [29] rule, the wavefunction for a collection of electrons, if they are individual and non-interacting electrons 1,2,...,n in the

state i,j, ...,k, can be written as:

$$\Psi(r_1, r_2, ..., r_n) = \psi_i(r_1)\psi_i(r_2)...\psi_k(r_n) \tag{6}$$

As a result of this assumption, the probability of finding an electron at r_1 in space is independent of the position of the electron at position r_2, while in reality due to coulomb repulsion, electrons avoid each other. So, the correlation between pair electrons is ignored. Furthermore, in this picture, all non-interacting single electrons are considered to be identical, which defies the antisymmetric principle for the electrons. Hence, HF approximation [30] was born to address the issues that were raised in the Hartree approach. The fundamental idea of the HF is to describe the wavefunctions through a set of single particle orbitals ψ_n that form a single determinant of the form,

$$\Psi(r_1, r_2, ..., r_n) = \frac{1}{\sqrt{n!}} \begin{vmatrix} \psi_i(r_1) & \psi_j(r_1) & \cdots & \psi_k(r_1) \\ \psi_i(r_2) & \psi_j(r_2) & \cdots & \psi_k(r_2) \\ \vdots & \vdots & \ddots & \vdots \\ \psi_i(r_n) & \psi_j(r_n) & \cdots & \psi_k(r_n) \end{vmatrix} \tag{7}$$

The above determinant is known as the Slater determinant, if we change the order of rows then a sign change appears. Hence, the Slater determinant satisfies the requirement of the exchange antisymmetry principle; and the expectation value of the Hamiltonian based on the wavefunction we have just created is given as,

$$\begin{aligned} \langle \Psi | H | \Psi \rangle = & \sum_{i,\sigma} \int dr \psi_i^{\sigma *}(r) [\frac{1}{2}\nabla^2 + V_{ext}(r)] \psi_i^{\sigma}(r) + E_{II} \\ & + \frac{1}{2} \sum_{i,j,\sigma_i,\sigma_j} \int dr dr' \psi_i^{\sigma_i *}(r) \psi_j^{\sigma_j^*}(r') \frac{1}{|r - r'|} \psi_i^{\sigma_i}(r) \psi_j^{\sigma_j}(r') \\ & - \frac{1}{2} \sum_{i,j,\sigma} \int dr dr' \psi_i^{\sigma^*}(r) \psi_j^{\sigma^*}(r') \frac{1}{|r - r'|} \psi_j^{\sigma}(r) \psi_i^{\sigma}(r'). \end{aligned} \tag{8}$$

Moreover, the variational principle dictates that the optimum orbitals are the ones that minimize the energy. So to find the optimal eigenvalues of Equation 1, one has to run Equation 8 iteratively to obtain the desired eigenvalues. In Equation 8, the first line includes the single-body terms such as kinetic energy and the interaction energy due to electrons and the generated field by nuclei. The third and fourth terms are the direct exchange interactions among the electrons. These interactions include the terms where i=j which means an electron interacts with itself. This anomaly is known as a self-interaction error and it is canceled by the last term. Nevertheless, since the Slater determinant is not

a perfect approximation for a wavefunction there is still a discrepancy between the real ground state and the ground state obtained through HF formalism. This difference between exact energy, ε_0, and HF energy is known as correlation energy and it is defined as:

$$E_c = \varepsilon_0 - E_{HF} \tag{9}$$

Lastly, the HF explains that one can obtain the total wavefunction of a system by considering the single-particle wavefunction for each electron present in the system. However, in reality, there are 3N variables for a system with N electrons which makes it impossible to solve a system such as a solid with millions of electrons. Therefore, an efficient alternative method is required to bypass the complexity of an exact system. This alternative was later introduced as DFT, which uses electron density to solve a system instead of the wave function. The principles of the DFT method are explained in the coming sections of this chapter.

2.3 Hohenberg-Kohn Theorems and Kohn-Sham equations

The core concept behind DFT is two theorems that state when a quantum system is located at the lowest possible energy state of a respective Hamiltonian, one can retrieve all the information about the quantum system by operating on the electron density.

$$n(r) = N \int \prod_{i=2}^{N} dr_i |\Psi(r, r_2, ..., r_N)|^2 \tag{10}$$

These theorems are called the Hohenberg-Kohn (HK) theorems [31], and they result in all observable properties of a ground state system being determined by the three degrees of freedom in the real-valued electron density rather than the 3N degrees of freedom in the complex-valued wave function.

HK Theorem I: The ground state electron density for a system of interacting electrons is uniquely determined by the external potential.
HK Theorem II: Based on theorem I, there exists a universal functional of the density that minimizes the total energy corresponding to the full solutions of the Schrödinger equation.

$$E[n] = F[n] + \int d^3 r n(r) \nu(r) \tag{11}$$

$$\langle \psi_i | \psi_j \rangle = \delta_{ij} \tag{12}$$

$$\sum_{i=1}^{N} |\psi_i(r)|^2 = n(r) \tag{13}$$

Then the universal functional F[n(r)] is split into three terms:

$$\begin{aligned} F[n] = T_s[n] + E_H[n] + E_{xc}[n] = -\frac{\hbar^2}{2m} \sum_{i=1}^{N} \langle \psi_i | \nabla^2 | \psi_i \rangle \\ + \frac{1}{2} \int d^3r d^3r' \frac{n(r).n(r')}{|r - r'|} + E_{xc}[n] \end{aligned} \tag{14}$$

Although the HK theorems are extremely powerful, they do not offer a way of computing the ground-state density of the system in practice. Therefore, on still requires the calculation of the many-body wave function to construct the correct ground state density. About one year after the HK paper, Kohn and Sham devised a simple method to conduct DFT calculations that retain the exact nature of DFT [32]. In this paper, solving the energy of the ground state remains exact, but it still leaves a big challenge behind that all the quantum mechanical acting forces are pushed into one term known as the 'exchange-correlation' kernel or potential.

2.4 Kohn-Sham Framework

The approach that Kohn-Sham (KS) developed in their landmark paper led to the implementation of DFT. The ansatz of KS was formulated by considering a non-interacting system of electrons (Figure 3) in an effective potential, v_{KS}. The question now is whether such a v_{KS} exists that can uniquely reproduce the exact interacting ground state energy and density. KS showed this to be the case, and the mapping between the non-interacting and interacting systems defines the KS system of electrons. Since in this approach the electrons are non-interacting, the many-body wave function takes the form of a product state:

$$\Psi(r_i) = \prod_{i=1}^{N} \phi_i(r_i)$$

The wave functions ϕ_i are often referred to as "single particle orbitals". Since the Pauli exclusion principle only allows one fermion per single particle eigenstate of a Hamiltonian, there would be N single-particle orbitals in the KS system. Such a system can be defined as:

$$\left(-\frac{1}{2}\nabla^2 + v_{KS}(r) \right) \phi_i(r) = \epsilon_i \phi_i(r), \tag{15}$$

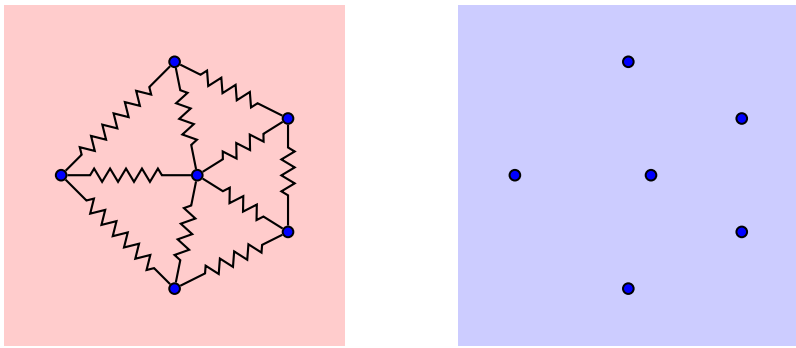

Real Interacting System Non-Interacting KS System

Figure 3: Schematic view of the Kohn-sham system

where v_{KS} is the effective KS potential in which the electrons move, and it is defined as

$$v_{KS} = v_{ext} + v_H + v_{xc} = -\sum_I \frac{Z_I}{r - R_I} + \int \frac{n(r')dr'}{r - r'} + \frac{\partial E_{xc}[n(r)]}{\partial[n(r)]}. \tag{16}$$

The KS equations are solved self-consistently (SC), since for the explicit i^{th} single particle orbital, the KS potential depends on all the other orbitals. As a first step of the SC, the initial density is guessed as a perturbation of atomic densities. Then by solving KS equations and obtaining the wave function, $\phi_i(r)$, the true electron density for the system can be obtained through

$$n^{KS}(r) = \sum_{occupied} |\phi_i(r)|^2, \tag{17}$$

if the resulting density is larger than the predefined criterion in comparison with the initial guess, then the process gets repeated otherwise the system is considered to be converged.

2.5 Exchange-correlation functional

In Equation, 16, the Exchange-Correlation (XC) term stands for all unknown quantum mechanical features of the system. Although the KS equation in principle is an exact solution for a system, it actually can not deliver an exact solution unless the XC term is known. Therefore, XC potential is approximated.

The simplest approximation for the XC energy is the Local Density Approximation (LDA) [33], which stems from uniform electron gas. Based on this, the XC

energy of LDA only depends on the local density of electron gas in a neutralizing positive background, which means LDA XC energy is equal to the XC energy per particle of the homogeneous electron gas. The corresponding relation is as follows

$$E_{xc}^{LDA}[n(r)] = \int d^3r n(r)\epsilon_{xc}(n(r)) \tag{18}$$

where $\epsilon_{xc}^{LDA}(n(r))$ is the XC energy per particle of a uniform electron gas of density $n(r)$. From Equation 18 it can be clearly seen that E_{xc} only depends upon the value of the electronic density at each point in space. Although this simple approximation proves to be sufficiently accurate for applications such as bond length, lattice parameters, phonon spectra, etc, it grossly underestimates the band gap, especially in solids leading to wrong calculation of other optical and electronic properties.

An improved approximation to the XC functional, known as the Generalized Gradient Approximation (GGA) [34], is to include information on the gradient of electron density. Within this approximation, the non-homogeneity of the true electron density is taken into account. The following relation depicts the GGA approximation to the XC energy

$$E_{xc}^{GGA} = \int d^3r n(r)\epsilon_{xc}^{GGA}(n(r)|\nabla n(r)) \tag{19}$$

where $\epsilon_{xc}^{GGA}(n(r)|\nabla n(r))$ is the exchange-correlation energy per electron with density $n(r)$ and gradient $\nabla n(r)$. GGA deals with inhomogeneous electron gas better and shows systematic improvement over LDA especially in the calculation of the cohesive and binding energies. Nevertheless, the underestimation of band gap especially in solids remains an issue, which consequently leads to miscalculation of properties such as absorption, dielectric properties and etc. This underestimation issue is mainly due to an intrinsic problem in LDA and GGA that is known as Self-Interaction Error (SIE). The SIE stems from the inability of approximate density functionals to exactly cancel self-coulomb and self-exchange-correlation for all one electron densities [35, 36]. To reduce the shortcomings of the semi-empirical approaches hybrid functional were developed. Hybrid functional is a type of DFT that combines the accuracy of a many-body method such as HF with the computational efficiency of DFT. The idea behind hybrid functionals is to incorporate a fraction of the exact HF exchange into the DFT exchange-correlation functional to improve the description of the electronic properties of the system. Among hybrid functional, the screened hybrid functional developed by Heyd, Scuseria, and Ernzerhof (HSE) [37, 38], has proved to be effective, especially for solids. The HSE functional has been widely used to study the electronic properties of a wide range of materials,

including semiconductors, insulators, and metals [39]. It has been used to study the electronic structure of various materials, including the band structure, the density of states, and the optical properties, and it has been found to provide improved results over traditional DFT functionals for many systems.

$$E_{xc}^{hybrid} = \alpha E_x^{HF} + (1-\alpha)E_x^{GGA} + E_c^{GGA} \tag{20}$$

Equation 21 shows the relation and mixing parameters of HSE functional. Although the mixing parameter is arbitrary and variable with respect to the system under study the most common combination is HSE06 in which α is set to 0.25. This means the share of exchange HF energy in final XC energy is 25%.

$$E_{xc}^{HSE} = \alpha E_x^{HF,SR}(\omega) + (1-\alpha)E_x^{PBE,SR}(\omega) + E_x^{PBE,LR}(\omega) + E_c^{PBE} \tag{21}$$

In the above equation, Perdew-Burke-Ernzerhof (PBE) [34] is essentially a GGA approximation that has a different set of parameterizations than generic GGA. The exchange part is divided into Short-range (SR) and Long-range (LR) components. ω is the screening parameter that indicates the range separation. This means it identifies the distance for which the short-range interactions become negligible. In other words, when ω goes to ∞, all the interactions that make up the exchange energy are treated as long-range whereas when ω goes to 0 all the interactions are considered to be short-range. In any case, HSE is a substantial improvement over GGA and LDA in band gap calculation and consequently in the optical and electronic properties of a system. Nevertheless, the mixing parameter is not generic so it needs to be adjusted for the specific system to obtain the correct band gap.

2.6 Pseudopotentials

When individual atoms come together to form a crystalline material, the highest electronic states undergo a considerable transformation. These electrons, referred to as valence electrons, partake in the process of chemical bonding. However, the core electrons, which are inherently low in energy, largely remain unaffected irrespective of their chemical surroundings. Consequently, their influence on the properties of the material is significantly less prominent.

When it comes to representing free electrons, which are weakly bound valence electrons, plane waves serve as the natural choice for a basis set. If we aim to describe the nuances of chemical bonding, an intuitive approach would be to 'freeze' the core states. Thereafter, we can solve the KS equation for the valence states within a plane wave basis set. This concept lies at the heart of the Pseudopotential (PP) approximation. Why do we freeze the tightly bound

core states? The reason is simple: solving the atomic-orbital-like core states would necessitate an impractically large number of plane waves in the basis. In this context, freezing refers to the act of fixing these core states to streamline the computational process while ensuring accuracy.

This approach is justifiable as the core states and the hard potential of the atomic cores remain largely consistent across different calculations. Therefore, the strong potential can be replaced with a more manageable PP that corresponds to the pseudo-wavefunctions, denoted as Ψ^{PS}. The basic principles of PPs are explained by Philips-Kleinman [40] in which they consider ψ_c and ψ_v to be the exact core and valence states respectively. ψ_v then solves the Schrödinger equation with eigenvalues E_v,

$$H\psi_v = E_v\psi_v \tag{22}$$

where the pseudo wavefunctions are smooth functions expressed as expansions of plane waves.

$$\psi_k(r) = \sum_G c_k, Ge^{i(k+G).r}, \tag{23}$$

and the G are the reciprocal lattice vectors.

The pseudo wavefunctions are not orthogonal to the core states so the exact valence states can be related to the pseudo wavefunctions with the part linearly dependent on the core states subtracted,

$$\psi_v = \psi_v^{PS} - \sum_c \langle\psi_c|\psi_v^{PS}\rangle\, \psi_c. \tag{24}$$

substituting the above equation into a plane wave gives:

$$H\psi_v^{PS} - \sum_c \langle\psi_c|\psi_v^{PS}\rangle\, H\psi_c = E_v(\psi_v^{PS} - \sum_c \langle\psi_c|\psi_v^{PS}\rangle\, \psi_c). \tag{25}$$

As $H\psi_c = E_c\psi_c$ for the core states, the Equation 25 can be rewritten as,

$$H\psi_v^{PS} = E_v\psi_v^{PS} + \sum_c \langle\psi_c|\psi_v^{PS}\rangle\, (E_c - E_v)\psi_c$$

$$(H + \sum_c (E_v - E_c)\, |\psi_c\rangle\, \langle\psi_c|)\psi_v^{PS} = E_v\psi_v^{PS} \tag{26}$$

This way the problem of solving a Schrödinger equation in a hard potential $H = -\frac{1}{2}\nabla^2 + V_{eff}$ for the exact valence states ψ_v can be transformed into the easier problem of solving the Schrödinger equation in a softer potential,

$$V^{PS} = V_{eff} + \sum_c (E_v - E_c)\, |\psi_c\rangle\, \langle\psi_c| \tag{27}$$

for the pseudo-wavefunctions ψ_v^{PS} but with the true energy eigenvalues, E_v. This soft potential is called the PP and it is calculated once and for all, along with the core states, for an isolated atom.

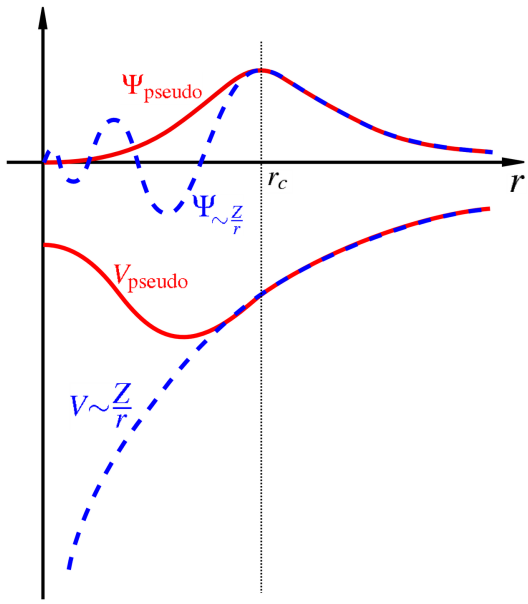

Figure 4: Schematic illustration of pseudopotential

The schematic illustration of PP is depicted in Figure 4. Here, we can observe that within the core region, the potential adopts a soft nature. As we move outside the core region, the PP gradually merges with the effective potential due to the fading presence of core wavefunctions. This leads to an interesting phenomenon - beyond a certain atomic radius r_c, the pseudo wavefunctions coincide with the exact all-electron wavefunctions.

The primary aim of PPs is to significantly minimize the computational requirements, hence an optimal PP should be as gentle, or "soft," as possible. This translates to needing as few plane waves as feasible for the expansion of the pseudo wavefunction [41]. Additionally, it's imperative for a PP to possess the characteristic of being transferable, meaning it retains its accuracy irrespective of whether it's applied to individual atom computations or crystal formations. Moreover, the creation of a PP is founded on specific atomic configurations, but its applicability extends to diverse scenarios without losing precision. The charge density of pseudo-wavefunctions is also crucial as it should approximate the true valence density as closely as possible since it's an integral physical property. This is pivotal because the charge density directly influences the

physical and chemical properties of the system under study [42]. Therefore, a well-constructed PP is characterized by its softness, transferability, and ability to replicate the true valence density as closely as possible.

PPs come in a few varieties, such as Ultrasoft (US) [43] and Norm-Conserving (NC) [44] PPs. The Ultrasoft PP approach uses larger values of the core radius, which consequently reduces the cutoff energy. This method was introduced to perform calculations with the lowest feasible cutoff energy for the plane-wave basis set. The technique achieves this by allowing pseudo wavefunctions to be as soft as possible within the atom's core region, resulting in a significant decrease in the cutoff energy [45]. On the other hand, Norm-Conserving PPs, in addition to ensuring that pseudo-wavefunctions and potentials correspond to the real valence wavefunction and the original potential beyond the core radius r_c, also mandates that the norm of the pseudo-wavefunctions and the original wavefunctions must be equal within the core radius [45]. The Projector Augmented WAVE (PAW) method, however, differs from the traditional PP methods. Instead of being a traditional PP method, it serves as an all-electron method that works between the exact all-electron wavefunction. PAW was essentially constructed (Figure 5) as a hybrid of the Linear Linear Augmented-Plane-Wave (LAPW) and the US potential methodologies. It is based on the transformation between the exact all electron wavefunctions, Ψ_n, and the smooth Pseudo wavefunctions, $\tilde{\Psi}_n$,

$$|\Psi_n\rangle = \Im\,|\tilde{\Psi}_n\rangle \tag{28}$$

This leads to an equivalent KS equation for the pseudo wavefunctions,

$$\Im^{\dagger} H \Im\,|\tilde{\Psi}_n\rangle = E_n \Im^{\dagger}\Im\,|\tilde{\Psi}_n\rangle \tag{29}$$

when solved, the pseudo wavefunctions are transformed back to the true wavefunctions which are then used to evaluate the total energy. The $\Im$ is denoted as the transformation operator, and it is expressed in terms of the solutions of the Schrödinger equation for an isolated atom, $|\phi_i\rangle$, and the soft pseudo version of them, $|\tilde{\phi}_i\rangle$.

$$\Im = 1 + \sum_i (|\phi_i\rangle - |\tilde{\phi}_i\rangle)\,\langle\tilde{p}_i|\,. \tag{30}$$

The $|\tilde{p}_i\rangle$ are the projector operators dual to the states $|\tilde{\phi}_i\rangle$, fulfilling $\langle\tilde{p}_i\rangle\,\tilde{\phi}_i = \delta_{ij}$, if i and j belong to the same augmentation sphere.

The PAW method is noteworthy for its efficiency and accuracy. With its requirement for fewer plane waves, PAW leads to a reduced energy cutoff when opposed to NC-PP methods. This quality renders PAW less resource-intensive, situating it closer to the computational characteristics of US-PP. One of the

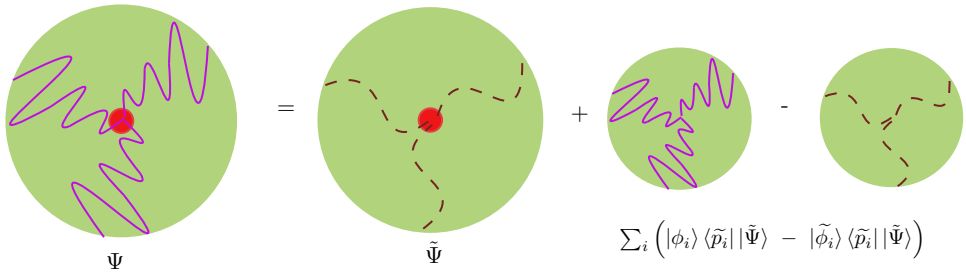

Figure 5: The schematic illustration of constructing PAW all-electron wavefunction.

major advantages of PAW is its ability to offer superior descriptions of materials with considerable magnetic moments, particular transition metals, and alkali as well as alkali-earth metals. This performance supersedes that of US-PP. However, it is important to note that for a broad range of other materials, the results produced by PAW and US-PP show similarities. Further benefits of the PAW method encompass its ability to provide the all-electron density and potential, surpassing the mere provision of the valence part. It also incorporates non-collinearity for magnetic moments and possesses the potential to navigate beyond the frozen core approximation.

3 Beyond density functional theory

As outlined in the introductory section, RE-doped optical materials have a broad range of applications, including their use as phosphors. A prominent example of this is the use of RE-doped YSO & YVO_4. The luminescence properties of these materials play a significant role in their utility, largely influencing their application potential in various fields. The optical and luminescent properties of these materials are largely dictated by the state of excitation they achieve. Consequently, this section is devoted to an exploration of the methods used to accomplish such states of excitation.

In the first part of this section, a detailed review of the applicable excitation methods is provided. This is followed by an introduction to the constrained DFT approach that has been utilized in the research undertaken for this thesis. The discussion thus provides a comprehensive overview of the theoretical and practical aspects that underpin the use and study of RE-doped optical materials.

3.1 Many-body perturbation theory

Many-body perturbation theory is a method to describe the interactions between multiple particles in a system. It involves a systematic expansion of the energy of the system in terms of the strength of the interactions between the particles, allowing for the calculation of properties such as the energy levels and wave functions of the system. These methods are based on GW (G is for one-body Green's function, and W for the dynamically screened Coulomb interaction) approximation, which applies a quasi-particle correction to the ground state eigenvalues obtained through DFT or HF methods [46]. To clarify, Green's function, G, is a matrix that depends on two spatial, two spins, and two-time coordinates:

$$i = (r_i, \xi_i, t_i) \tag{31}$$

The matrix element $G(12)$ is defined in such a way that $i\hbar G(12)$ gives the probability amplitude for the propagation of a particle or hole that is created at space and time coordinate (r_2, ξ_2, t_2), where it is picked up at the point (r_1, ξ_1, t_1). This way a system of N-electrons ground state $|\Psi_0^N(t_2)\rangle$ is brought to a final state $|\Psi_f^N(t_1)\rangle$ by the successive action of operators on the initial state,

$$|\Psi_f^N(t_1)\rangle = \hat{\psi}(r_1)\hat{U}(t_1, t_2)\hat{\psi}^+(r_2)\,|\Psi_0^N(t_2)\rangle \tag{32}$$

As the above equation explains, first an electron gets added to the system with the creation operator, $\psi^{+}(r')$, then the evolution operator propagates the N+1 particle stat in time,

$$\hat{U}(t_1, t_2) = exp(-\frac{i}{\hbar}\hat{H}(t_1 - t_2)). \tag{33}$$

To complete the cycle, the annihilation operator, $\hat{\psi}(r)$, removes the added electron from the system. At this stage, the probability amplitude of an electron at (2) if it is added at (1) can be obtained by the overlap of the initial state with the final state. Therefore, the G function of an electron becomes,

$$\begin{aligned} G^{e}(12) &= -\frac{i}{\hbar}\langle\Psi_0^N(t_1)|\hat{\psi}(r_1)\hat{U}(t_1,t_2)\hat{\psi}^{+}(r_2)|\Psi_0^N(t_2)\rangle\,\Theta(t_1-t_2) \\ &= -\frac{i}{\hbar}\langle\Psi_{0,H}^N|\hat{\psi}_H(r_1,t_1)\hat{\psi}_H^{+}(r_2,t_2)|\Psi_{0,H}^N\rangle\,\Theta(t_1-t_2) \end{aligned} \tag{34}$$

where the Heaviside step function,

$$\Theta(t_1 - t_2) = \begin{cases} 1 & if \quad t_1 > t_2, \\ 0 & if \quad t_1 < t_2. \end{cases} \tag{35}$$

The Equation 34 is also applicable on hole propagation from state (2) to state (1) that leads to,

$$G^{h}(12) = -\frac{i}{\hbar}\langle\Psi_0^N|\hat{\psi}^{+}(r_1,t_1)\hat{\psi}(r_2,t_2)|\Psi_0^N\rangle\,\Theta(t_1-t_2), \tag{36}$$

so the combination of Green's function for electron and hole propagation gives the time-development Green's function:

$$G(12) = G^{e}(12) - G^{h}(21) = -\frac{i}{\hbar}\langle\Psi_0^N|\hat{T}[\hat{\psi}(1)\hat{\psi}^{+}(2)]|\Psi_0^N\rangle\,, \tag{37}$$

where $\hat{T}$ is the time-development operator that arranges a series of field operators in order of descending time arguments. To reach the final form of the equation 37, the time-development function is considered for a stationary system, where $\tau = t_1 - t_2$, and a projection operator onto the complete set of state vectors $\Psi_i^{N\pm1}$ of the $(N \pm 1)$ particles system is inserted into the equation. Furthermore, Fourier transformation is employed to switch to the frequency-based representation of Green's functions. This leaves us with the Lehmann representation of Green's function:

$$G(r_1, r_2 : \omega) = \sum_i \frac{\Psi_i(r_1)\bar{\Psi}_i(r_2)}{\hbar\omega - \epsilon_i + i\eta sgn(z_i - \mu)} \tag{38}$$

The μ is the chemical potential and $z_m = \epsilon_m + i\gamma_m$, where ϵ_i is the single-particle excitation energies and γ_m is the lifetimes of the interacting many-body system as, $\gamma_m = 2\pi/\tau_m$. This shows that Green's function can be used to directly estimate excitation energies for a single-particle system. To build upon this and derive Green's function for a many-body system of interacting electrons under the influence of an external potential one can employ Hedin equations. The full derivation of Hedin equations and the steps that lead to GW approximation are documented in [47, 48]. The resulting equations for GW approximation are listed here:

$$G(12) = G_H(12) + \int d(34) G_H(13) \hat{\Sigma}(34) G(42) \tag{39}$$

$$\hat{\Sigma}(12) = iG(12^+)W(12^+) \tag{40}$$

$$W(12) = \nu(12) + \int d(34) \nu(13) P(34) W(42) \tag{41}$$

$$P(12) = -iG(12)G(21^+) \tag{42}$$

The $\hat{\Sigma}$ is the self-energy, the screened-interaction W, the Green's function of the non-interaction mean-field system G_H, the P is the polarization function, and the G is the full interacting many-body system.

The GW method is widely used to study the electronic structure of strongly correlated materials such as transition metal oxides, high-temperature superconductors, and heavy fermion materials (Lanthanides) [49]. The GW approximation combined with the Bethe-Salpeter equation (BSE) (GW+BSE) is a state-of-the-art method for studying the electronic structure of solids with defects [46]. The GW+BSE method is particularly useful for studying systems with point defects, such as impurities or vacancies, as it can provide detailed information about the electronic states localized at the defect site and their effect on the optical properties of the material [49]. However, it's important to note that GW is an approximate method and in some cases, it is known to provide results that deviate from experiments, especially for the low-energy excitations of these materials. Here low-energy excitations mean an association of the valence and conduction bands of material, and they can have a significant impact on the material's physical properties. This is the type of excitation we deal with in this thesis, as the transition between the valence states of the impurity to the conduction states does not require high energy to occur. To be precise, the required energy for such transitions to occur is in the order of 370 -

371 nm [50]. Aside from that GW+BSE techniques are significantly limited by the size of the material under study, namely the computational cost for larger cells makes it not applicable for the study of defects with large supercells [51].

The most recent addition of many-body perturbation theory that in some cases is considered as an improvement over GW+BSE is (Dynamical Mean Field Theory (DMFT)) GW+DMFT approximation [52], especially for the description of the low-energy excitations of strongly correlated materials [53]. It can provide a more accurate description of the electronic structure of the material, including the quasiparticle energies and lifetimes. In addition, it is specifically designed to take into account the electronic correlation effects, which are particularly important in strongly correlated materials such as transition metal oxides and heavy fermion materials [52]. Nevertheless, it is severely limited due to computational demand and convergence problems [54]. The GW+DMFT is based on several approximations, and it requires a careful treatment of the electronic correlation effects. The quality of the results obtained with the GW+DMFT method depends on the quality of the initial input (e.g. the DFT band structure, the Coulomb interaction parameter) and the choice of the impurity solver. Aside from these, it can be difficult to converge, especially for systems with multiple correlated orbitals, such as Lanthanides where both f-type and d-type orbitals exist, or for systems with strong electron-electron interactions.

3.2 Multiconfigurational methods

Multiconfigurational methods are used to study systems with multiple electronic configurations, such as molecules with several equivalent but differently occupied orbitals or with electron correlation effects. Examples of multiconfigurational methods include Configuration Interaction (CI) [55] and Complete Active Space Self-Consistent Field (CASSCF) techniques [56].

Configuration Interaction

The HF method determines the best determinant wavefunction for a given basis set, but it lacks a correlation effect. To overcome this weakness, additional Slater determinants can be added to correct the outcome energy. The additional determinants should be in the form of singly, doubly, triple, ..., N-tuply excited states since an N-variables system can be exactly expanded in terms of all unique determinants formed from a complete set of one variable wavefunction ψ_i [57].

So the exact wavefunction, $|\Phi\rangle$, for any state of the system can be written as,

$$|\Phi\rangle = c_0 \underbrace{\Psi_0}_{\text{HF}} + \sum_{r,a} c_a^r \underbrace{\Psi_a^r}_{\text{Singles}} + \sum_{\substack{a<b \\ r<s}} c_{a,b}^{r,s} \underbrace{\Psi_{a,b}^{r,s}}_{\text{Doubles}} + ... \tag{43}$$

In the above equation, a singly excited determinant has one electron promoted from orbital ψ_a in the HF ground state to an unoccupied orbital ψ_r which generates a determinant,

$$|\Phi_a^r\rangle = |\psi_1, \psi_2, ...\psi_r, \psi_b..., \psi_{n-1}, \psi_n\rangle\,, \tag{44}$$

and the same logic is applied for doubly excited determinants with two electrons excited from orbitals ψ_a and ψ_b in the HF ground state to an unoccupied orbital ψ_r and $\psi - s$ which generates a determinant

$$|\Phi_{ab}^{rs}\rangle = |\psi_1, \psi_2, ...\psi_r, \psi_s, \psi_c..., \psi_{n-1}, \psi_n\rangle\,. \tag{45}$$

In Equation 43 when all possible excited Slater determinants are considered, it becomes Full-CI. Full-CI is computationally intensive and scales as N^4 or N^5 with the number of active electrons and orbitals, making it impractical for systems with many electrons. In addition, it is sensitive to the quality of the basis set used and requires large basis sets to accurately describe the electron correlation. This can make the calculations computationally expensive and can lead to large errors if a smaller basis set is used. Moreover, it is not well-suited for open-shell systems, where electrons occupy different orbitals with different spins. Last but not least, it has to be mentioned that is limited by the choice of the active space, which defines the number of electrons and orbitals included in the calculation. An incorrect choice of the active space can lead to significant errors in the results.

Complete Active Space-SCF (CASSCF)

CASSCF is normally used for studying the electronic structure and reactivity of molecules, including energy levels, bond strengths, spectroscopic properties, and electronic transitions. In CASSCF, the active space is optimized self-consistently. This allows for the consideration of electron correlation within the active space. The accuracy of the CASSCF calculation can be further improved by adding post-SCF methods, such as CI or Second-order perturbation theory (MP2) [56]. This method gives very accurate results and it is especially suitable for excitation studies such as electronic transitions and excited state dynamics, including photochemical reactions and spectroscopic properties. However, just like its other counterpart it has limited application on solids

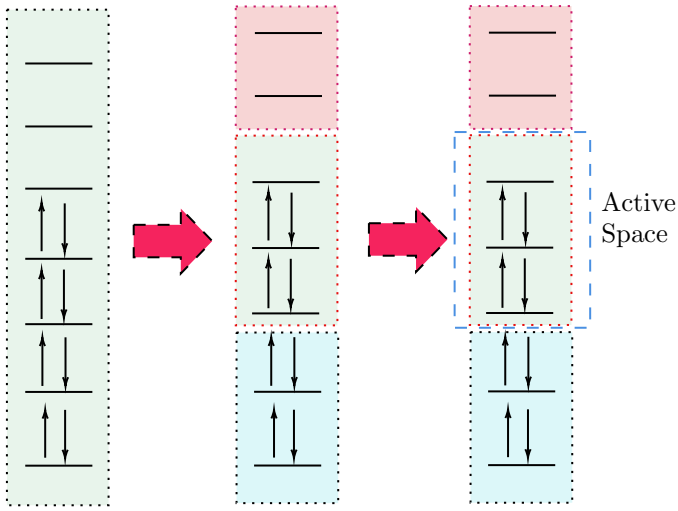

Figure 6: The schematic view of the CASSCF approach. From left to right, the figure shows the selection of active space, where the first diagram shows the ground state, Ψ_{HF}, and the last diagram depicts the orbitals that are selected to perform excitation.

and systems with large numbers of electrons. The main reason behind this is computational cost and active space sensitivity.

3.3 Time-dependent density functional theory

Time-dependent density functional theory (TDDFT) is an exact reformulation of time-dependent quantum mechanics in which instead of solving the time-dependent Schrodinger equation by considering the many-body wave function the density is the fundamental parameter. Thus, it is based on DFT but extends DFT to include the time dependence of the electron density [58]. TDDFT can be used to calculate a wide range of properties, such as absorption and emission spectra, and can be applied to a wide range of systems, including molecules, solids, and biomolecules [59]. The central theorem of TDDFT, which is known as Runge-Gross [60] theorem proves that there is a one-to-one correspondence between external potential, $\nu_{ext}(r,t)$, and the electronic density, $n(r,t)$, for many-body systems evolving from a fixed initial state.

$$i\frac{\partial}{\partial t}\Psi(r,t) = \hat{H}(r,t)\Psi(r,t) \tag{46}$$

The time-dependent Schrödinger equation can be written based on KS eigenvalues as:

$$i\frac{\partial}{\partial t}\phi_i(r,t) = \hat{H}_{KS}(r,t)\phi_i(r,t) \tag{47}$$

$$\hat{H}_{KS}(r,t) = -\frac{\nabla^2}{2} + \nu_{KS}[n](r,t) \tag{48}$$

$$n(r,t) = \sum_{i}^{N} |\phi_i(r,t)|^2 \tag{49}$$

$$\nu_{KS}[n](r,t) = \nu_{ext}(r,t) + \nu_{Hartree}[n](r,t) + \nu_{xc}[n](r,t) \tag{50}$$

As was the case in the ground state, here the first term is external potential, the second term is the classical electrostatic interaction between the electrons, and the third term is the exchange-correlation, which includes all nontrivial many-body effects.

In general, TDDFT is considered to be a good alternative approximation for the calculation of electronic excitation energies of a variety of systems, such as molecules, solids, and surfaces that often provide good agreement with experimental results. Moreover, it offers a computationally more efficient way of solving excitation compared to traditional methods for calculating excited states, such as CI or Coupled cluster (CC) methods, and it is size-extensive in which the results for a large system can be obtained through scaling up the result of a smaller system. However, it is less accurate for open-shell systems, such as transition metal complexes, and for systems with strong electron correlation [51]. The fact that in this thesis the system under study is exactly a system with strong electron correlation makes this approach unsuitable.

3.4 Constrained density functional theory

Constrained Density Functional Theory (CDFT) is a method used in electronic structure calculations to study the properties of a material under specific constraints. CDFT allows for the imposition of constraints on the electronic density, orbital or occupancy, magnetization (H), or other properties of the material being studied. In CDFT calculations, the constraints are incorporated into the functional used in the calculation. The method requires a self-consistent solution of the KS equations, and the resulting eigenvalues and eigenvectors can be used to obtain the electronic structure and other properties of the material under the imposed constraints. Essentially, CDFT takes advantage of DFT characteristics that are low computational cost, and the ability to efficiently perform atomic relaxation. These benefits are especially crucial for defect calculations since large supercells or clusters are required to model an isolated defect and

large numbers of calculations are typically required to characterize the atomic and electronic structure of the defect. Therefore, there is a significant incentive for devising DFT-based techniques that can provide a qualitative and even quantitative understanding of properties connected to excited states.

The corresponding original CDFT formalism is described in the following references [61, 62], however, a short description of this methodology is presented here to create a base for our studies.

In Equation 51, the Lagrange multiplier, $V(\int_\Omega n(r)d^3r - N)$, is added to yield the lowest-energy state by constraining the optimization for N electrons in the volume Ω .

$$E(N) = \min_n \max_V [E[n(r)] + V(\int_\Omega n(r)d^3r - N)] \tag{51}$$

For example, one could constrain the local f-charge variation in RE metals as follows:

$$E(N_f) = \min_n \max_{V_f} [E[n(r)] + V_f(\int n_f(r)d^3r - N_f)]. \tag{52}$$

In another example, one can constrain net magnetization

$$E(M) = \min_n \max_H [E[(n)] + H(\int_\Omega m(r)d^3r - M)] \quad [m(r) \equiv n^\alpha(r) - n^\beta(r)] \tag{53}$$

It is also possible to unify all these constraints and write them in one equation as follows,

$$W[n, V; N] \equiv E[n] + V(\sum_\sigma \int w^\sigma(r) n^\sigma(r) d^3r - N) \tag{54}$$

, where $w^\sigma(r)$ is a spin-dependent weight function that defines the property of interest:

$$E(N) = \min_n \max_V \quad W[n, V; N]. \tag{55}$$

The CDFT has demonstrated its potential by generating results that align favorably with those derived from TDDFT and photoluminescence experiments, particularly when a hybrid functional is applied [63, 64]. This technique also exhibits performance similar to the cluster-embedded methodologies at the level of CASSCF+MPT2 accuracy [65]. The significant advantage of the CDFT approach lies in its combination of high accuracy and lower computational cost, making it an attractive tool for post-DFT applications [65]. In contrast, embedded cluster approaches often simulate the lattice environments of the clusters by

embedding Ab-initio model potentials (AIMPs) [66]. For instance, in the computation of Ce-doped [67] and Yb-doped YSO [68], authors used the AIMPs approach and utilized Electron Paramagnetic Resonance (EPR) data to tailor the model to their phenomenological representation for determining the energy levels of the impurity. However, this approach's reliance on empirical data can be restrictive when the objective is to predict the material's specific behavior under study without having any previous experimental data, which is the case in this thesis. Considering the aforementioned benefits, the CDFT approach has been chosen for use in this thesis. The methodology's precision, affordable computational expenditure, and lesser dependency on empirical data present a compelling case for its selection in the exploration of complex material behaviors.

In this study, we applied constraints on the occupancy of electrons, meaning we controlled and maintained a constant number of electrons in specific orbitals throughout our calculations. This process alters the electron density, subsequently affecting the spatial distribution of electrons within the system. By manipulating the electron occupancy of the system, we can generate a novel ground state for the system that effectively serves as the excited state for the reference system. Figure 7 illustrates the sequence through which excitation is accomplished via the constrained occupancy method.

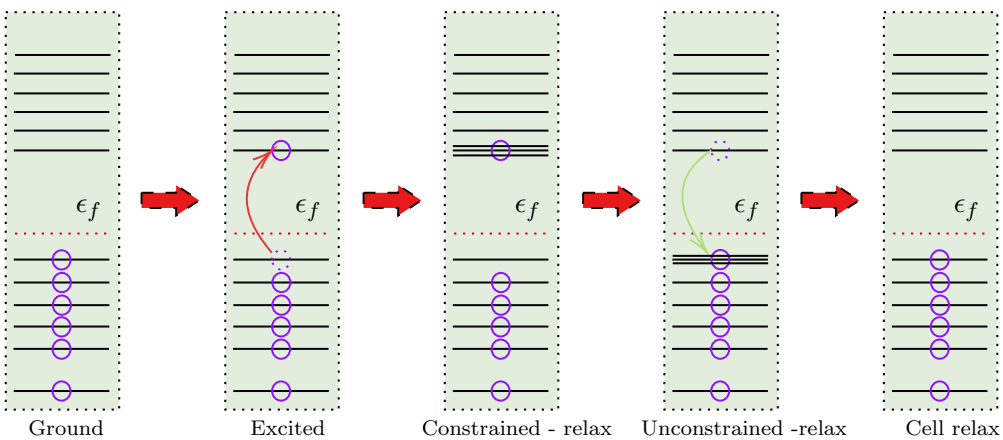

Figure 7: Schematic view of the constrained occupancy approach. ϵ_f denotes the fermi level.

Our methodology stands apart from previous constrained occupancy studies [69, 70, 71], which employed the DFT+U approach. Instead, we opted for the direct application of hybrid DFT to compute the energies of both ground and excited states. This choice was guided by our primary objective: to gain insights into the placement of 4f and, preferably, 5d within the band gap for potential

use in phosphors. The DFT+U approach was deemed unsuitable for this study as it necessitates prior knowledge of 4f to fine-tune the U parameter of the 4f impurity. Since the goal of the study is to formulate a generic approach, the DFT+U violates this. Whereas the proposal is to use the band gap modified HSE coupled with Spin-orbit coupling (SOC) approach. In this approach, as we just tune the HSE parameters with respect to the host band gap there would be no requirement for knowledge of 4f shells which are variant depending on the impurity. So it can be dubbed as one-shot tuning.

4 Results & Discussion

In this chapter, we present a comprehensive summary of the research conducted during this doctoral study. The results are structured in alignment with the sequence of the research papers that are listed at the beginning of this booklet, ensuring a logical and chronological flow of information.

4.1 Optical path length

In an optical cavity (Figure 8) the resonant frequency is a crucial aspect since it controls the laser output [72], aids in precision measurement [73], and helps to measure the absolute frequency of optical transition [74]. The resonance frequency is directly dependent on the physical length of the cavity itself as well as the dielectric properties of the medium namely the refractive index of the material. The relation between these parameters and the resonant frequency of the optical cavity can be written as:

$$m\lambda = 2nL \tag{56}$$

, where m is the mode number, λ is the wavelength, n is the refractive index, and L is the physical length of the cavity. The right-hand side of Equation 56, defines the Optical path length (OPL), and it describes the total distance that light travels through a medium, adjusted for the n of that medium. Variations in the OPL can induce shifts in the resonance frequency of the optical cavity. Such shifts can have multiple consequences: they may detune the laser [75], affect the functioning of the device [76], influence the results of spectroscopic methods [77], and impact the operation of optomechanical systems [78]. Essentially, these shifts in the OPL can generate unintended noise and disturbances, with potential ramifications on the precision and dependability of experimental results. Therefore, understanding the variations in the L and n is critical in mitigating such noise in our experimental outcomes. One such experiment is laser stabilization [4]. Laser frequency can be tuned or stabilized by locking it to an optical resonance of an optical cavity that exhibits extreme length stability [79]. This procedure enables the realization of lasers with high-frequency stability and ultra-narrow linewidth [80]. So, the knowledge of an optical cavity's resonance frequency can be used to fine-tune the laser frequency, thereby ensuring the stability and precision necessary for various applications in optics and photonics.

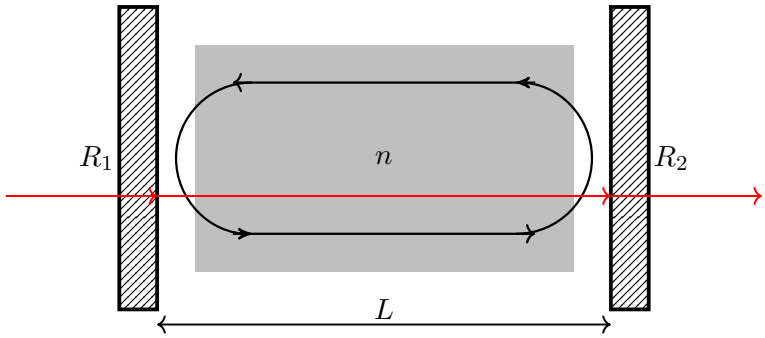

Figure 8: The schematic view of an optical cavity. The light path in the cavity is indicated by circulating arrows whereas the red arrows indicate entering and exiting light path.

As the resonance frequency is directly related to n & L, understanding and monitoring the refractive index's fluctuations can provide critical insight into maintaining laser stability. By continuously monitoring these fluctuations, appropriate adjustments can be made in real-time to the laser system to ensure its frequency remains stable. This could be done by implementing feedback mechanisms that respond to changes in the n or by controlling environmental conditions, such as temperature or applied pressure [25], that affect the n.

Therefore, in Paper II we tried to predict the fluctuation in n and consequently in resonance frequency through establishing photoelastic relation, where photoelasticity is essentially the phenomenon where the n of a material changes in response to stress [81]. To establish a photoelasticity relation in our desired system the YSO, we refer back to the structure of the crystal, which is monoclinic. This type of symmetry in optical terms is biaxial crystals that have two distinct optic axes, which are referred to as D_1 and D_2 [82] as they are depicted in Figure 9. Moreover, due to this symmetry, there are 4 different dielectric functions $\epsilon(\omega)$ that are required to describe the material's interaction with light in the wavelength region where the material is transparent [83]. The principle values of the dielectric functions are unequal and they are ordered as $\epsilon_{11} < \epsilon_{22} < \epsilon_{33}$ [83]. The off-diagonal, ϵ_{12}, is a small value but it is non-zero.

$$\epsilon = \begin{bmatrix} \epsilon_{11} & \epsilon_{12} & 0 \\ \epsilon_{12} & \epsilon_{22} & 0 \\ 0 & 0 & \epsilon_{33} \end{bmatrix} \tag{57}$$

The relation between mechanical load namely stress and dielectric permeability and consequently refractive index is defined in Equation 58 [84].

$$\Delta B_{ij} = p_{ijkl} e_{kl} = \pi_{ijkl} \sigma_{kl}, \tag{58}$$

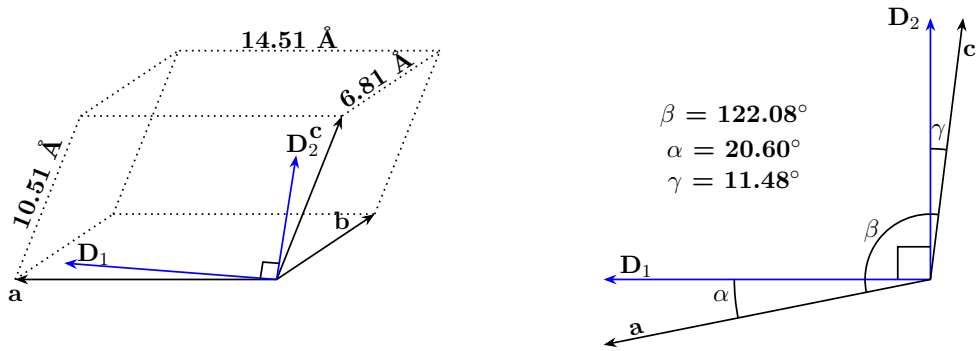

Figure 9: The angles and the relation between optical indicatrix axes and crystallographic axes.

where e_{kl}, σ_{kl} are strain and stress, p_{ijkl} and π_{ijkl} are fourth-rank elasto-optic and piezo-optic tensors, respectively. If we write the matrix form of the above equation for the monoclinic system, it becomes as [84],

$$\Delta B = \begin{pmatrix} \pi_{11} & \pi_{12} & \pi_{13} & 0 & \pi_{15} & 0 \\ \pi_{21} & \pi_{22} & \pi_{23} & 0 & \pi_{25} & 0 \\ \pi_{31} & \pi_{32} & \pi_{33} & 0 & \pi_{35} & 0 \\ 0 & 0 & 0 & \pi_{44} & 0 & \pi_{46} \\ \pi_{51} & \pi_{52} & \pi_{53} & 0 & \pi_{55} & 0 \\ 0 & 0 & 0 & \pi_{64} & 0 & \pi_{66} \end{pmatrix} \begin{pmatrix} \sigma_{11} \\ \sigma_{12} \\ \sigma_{13} \\ 2\sigma_{14} \\ 2\sigma_{15} \\ 2\sigma_{16} \end{pmatrix}, \tag{59}$$

and the left hand side of Equation 58 can be written as follows:

$$\Delta B_{ij} = B_1 - B_0 \tag{60}$$

where B_0 and B_1 are the dielectric impermeability tensor before and after the applied stress [85]. As the principal components of the B matrix is essentially the inverse of dielectric constants, one can reach to refractive indices that are affected by applied stress or temperature.

$$B_1 = [\epsilon^{-1}(\sigma_{kl})]_{ij} = \begin{pmatrix} \epsilon^{-1}(0)_{11} & \epsilon^{-1}(0)_{12} & 0 \\ \epsilon^{-1}(0)_{12} & \epsilon^{-1}(0)_{22} & 0 \\ 0 & 0 & \epsilon^{-1}(0)_{33} \end{pmatrix} + \begin{pmatrix} \Delta B_1 & \Delta B_6 & 0 \\ \Delta B_6 & \Delta B_2 & 0 \\ 0 & 0 & \Delta B_3 \end{pmatrix} \tag{61}$$

And after some manipulation, the stress-effected principal axes of the dielectric

tensor can be obtained as:

$$n_x(\sigma_{kl}) = \sqrt{(1/B_1^x)}$$

$$n_y(\sigma_{kl}) = \sqrt{(1/B_2^y)}$$

$$n_z(\sigma_{kl}) = \sqrt{(1/B_3^z)} \quad (62)$$

This implies that if we possess the photoelastic constants for a particular material we're studying, it would enable us to evaluate variations in the refractive index resulting from the application of a load. Therefore, to investigate the refractive index variations, we have established a Finite element methods (FEM) model, where we can apply both pressure and temperature conveniently. The creation of this model and the calculation of the photoelasticity correlation for both pure and doped structures necessitated first determining the mechanical and thermodynamic properties of both. Key properties such as specific heat and density of the unit cell in varying doping conditions, specifically the doping concentration, were instrumental in configuring the model for photoelastic calculations. Furthermore, given that the material under study exhibits anisotropic characteristics, a comprehensive understanding of the elastic constants is essential. For these reasons, we have investigated the mechanical and thermodynamic properties of both pure YSO and Eu-doped YSO in Paper I.

YSO, with its monoclinic symmetry, is defined by 13 unique elements within its elastic constants matrix as it is shown in Equation 63 [86]. This complexity emerges from the non-orthogonality of one angle in the unit cell, which engenders a nuanced stress-strain relationship [87]. In the tensor notation of Hooke's Law, the fourth-order elastic stiffness tensor, denoted as C, correlates with the Cauchy stress tensor, σ, and the infinitesimal strain tensor, ϵ, expressed by the equation $\sigma = C\epsilon$. Thus, leveraging this principle allows the derivation of the material's elastic constants.

$$C_{ij} = \begin{pmatrix} c_{11} & c_{12} & c_{13} & 0 & c_{15} & 0 \\ \vdots & c_{22} & c_{23} & 0 & c_{25} & 0 \\ \vdots & \ddots & c_{33} & 0 & c_{35} & 0 \\ \vdots & \vdots & \ddots & c_{44} & 0 & c_{46} \\ \vdots & \cdots & \cdots & \ddots & c_{55} & 0 \\ \cdots & \cdots & \cdots & \cdots & \cdots & c_{66} \end{pmatrix} \quad (63)$$

We computed the elastic constants for four specific concentrations of Eu^{3+}, substituting Y^{3+} ions in the host lattice: 6.25%, 12.5%, 18.75%, and 25%. As

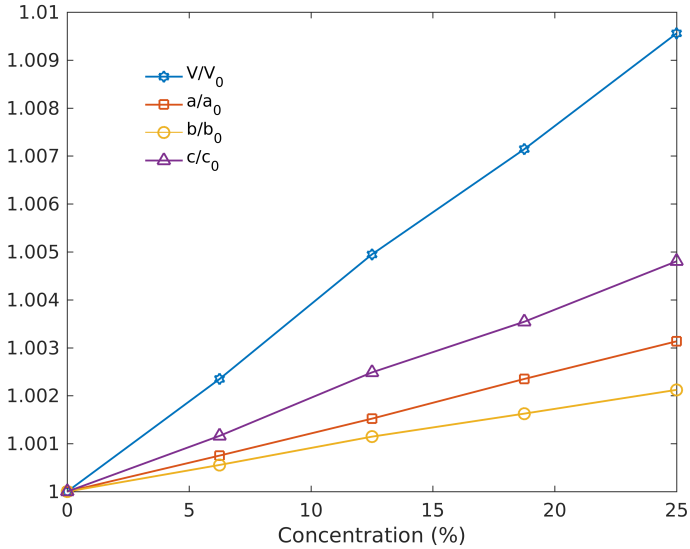

Figure 10: Relative volume, V/V_0, and lattice parameters, a/a_0, b/b_0 and c/c_0, with doping concentration.

depicted in Figure 10, our results unveil a linear correlation between the dopant concentration and both the lattice parameters and the unit cell volume. This observed linearity suggests that a linear polynomial could efficiently predict the lattice parameters and volume of RE-doped YSO systems. It's crucial to understand these shifts in the lattice parameter influenced by dopant concentration, as they directly impact the physical length (L) of an optical cavity. Given the variability in dopant concentration across experiments, possessing a predictive model sharpens our understanding of these influential parameters. Moreover, grasping this linear relationship between dopant concentration and YSO lattice parameters becomes vital when aiming for specific emission characteristics in optical applications. For example, YSO nano phosphors doped with Eu^{3+} emit a notable broad red band upon 397 nm excitation [88].

Furthermore, the linear correlation between dopant concentration and crystal parameters shows that an uptick in Eu^{3+} ion concentration corresponds with a decrease in YSO's overall shear, bulk, and Young's moduli, as depicted in Figure 11. This infers that augmenting dopant concentration reduces the material's mechanical resilience. Grasping this interrelation is imperative for estimating the material's robustness and endurance under mechanical pressure.

The Pugh ratio is included in Figure 12 to further investigate the physical properties of the material. The Pugh ratio gauges the ductility of materials based on

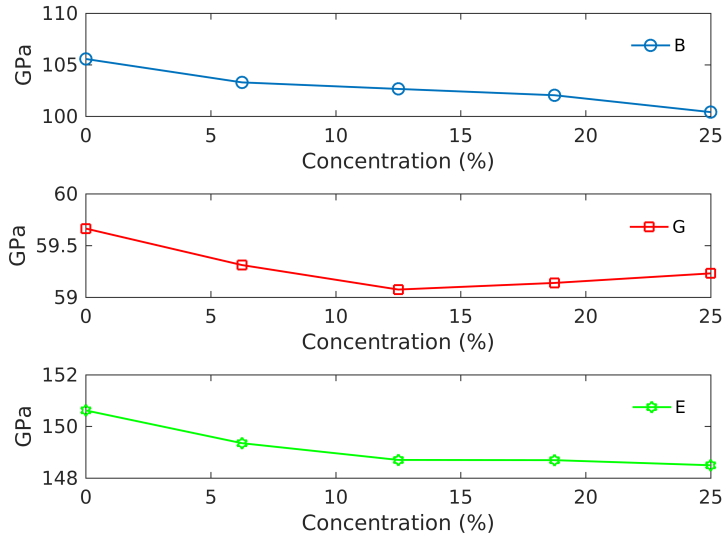

Figure 11: Elastic moduli as a function of Eu^{3+} doping concentrations.

the simple ratio given as B/G. The higher the value of this ratio, the higher the ductility of the material, and vice versa. As Figure 12 demonstrates, the ratio gradually decreases with increasing concentration. The overall drop of the Pugh ratio between pure and 25% doped crystal is 4.2%. Although this drop is small, it shows that there is a decreasing trend in the Pugh ratio which indicates the YSO becomes more brittle with higher impurity concentration.

While we observed that individual elastic constants didn't present a consistent trend, the thermodynamic properties derived from these constants did. Notably, the minimum thermal conductivities (κ_{min}), Grüneisen parameter (γ), and Debye temperature (θ_D), exhibit a decline with concentration, in contrast to density, as illustrated in Table 1. The Debye temperature is pivotal for contrasting the micro-hardness of materials, given its proportional relationship to material hardness. Additionally, a higher Debye temperature signifies stronger bond strength. A small increase in doping concentration appears to weaken this bond's strength, possibly due to intensified interatomic bonding. This phenomenon might be attributed to the larger atomic radius of Eu^{3+} relative to Y^{3+}. Thermal conductivity, depicting heat flow diffusivity via phonon transport, serves as an indicator of a material's heat conduction efficacy. In context, a greater κ_{min} value implies superior conductivity and vice versa. As seen in Table 1, YSO with a κ_{min} value of 0.995 is classified as possessing exceptionally low thermal conductivity. Lastly, as the concentration of Eu^{3+} grows, a drop in

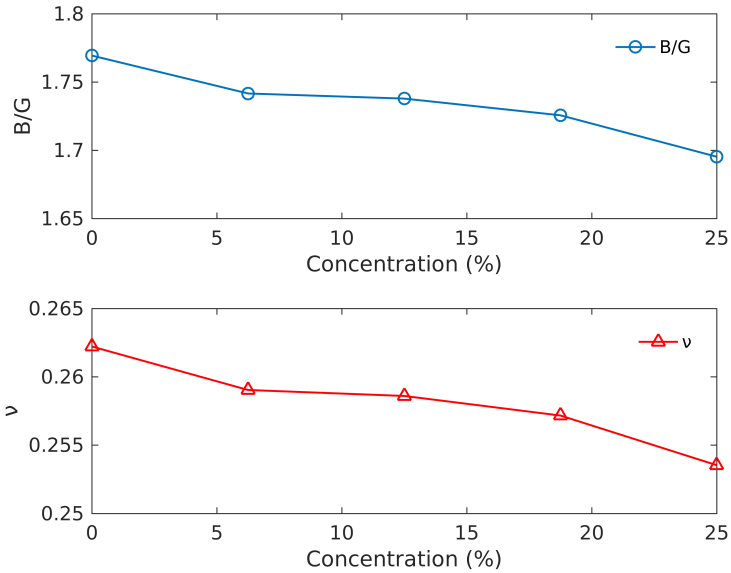

Figure 12: Pugh and Poisson's ratio of the YSO crystal as a function of Eu^{3+} doping concentrations.

the anharmonic phonon scattering within the YSO crystal is observed, leading to reduced thermal expansion due to decreased anharmonic scattering [89].

Table 1: Thermodynamic values predicted for pure YSO and Eu-doped YSO. *: *This study*

Compound	$\rho(g/cm^3)$	$\nu_l(m/s)$	$\nu_t(m/s)$	$\nu_m(m/s)$	$\theta_D(K)$	κ_{min}(W/mK)	γ
$Y_2SiO_5^*$	4.3142	6550.5	3718.8	3926.4	487.88	0.9443	1.560
$Eu^{6.25\%} : Y_2SiO_5^*$	4.4228	6421.5	3662.0	3862.6	483.95	0.9445	1.544
$Eu^{12.5\%} : Y_2SiO_5^*$	4.5298	6328.7	3611.3	3808.6	481.00	0.9462	1.542
$Eu^{18.7\%} : Y_2SiO_5^*$	4.6381	6245.3	3570.8	3764.3	479.16	0.9501	1.535
$Eu^{25\%} : Y_2SiO_5^*$	4.7448	6148.8	3533.2	3720.5	477.20	0.9534	1.517
Y_2SiO_5 [90]	-	-	-	-	580	1.13	-
Y_2SiO_5 [91]	4.680	6196	3580	3975	507	1.01	1.50

Next, our key interest was to assess the variations in specific heat with respect to concentration, denoted as C_ν. We employed the Debye model which estimates the phonon contribution to specific heat in solids, to predict heat capacities at a constant volume. Our findings, as illustrated in Figure 13, demonstrate that alterations in heat capacity due to concentration are essentially insignificant. This interpretation is anchored on the observed superposition of all C_v curves, indicating that no discernible deviation exists between different concentrations.

Furthermore, the predicted curves abide by the Dulong-Petit law at elevated temperatures (where T $\gg \theta_D$). According to this law, the heat capacity at constant volume, C_v, for every atom approximates 3R for temperatures surpassing the Debye temperature (which is computed as 514.35 K for YSO in this study). The gas constant here is represented by R.

However, it's crucial to note that when temperatures dip below the Debye temperature, θ_D, quantum effects become increasingly significant and the C_v tends towards zero. This is attributed to the fact that at such low temperatures, the thermal excitation is mainly contributed by long wavelength acoustic modes, which results in an approximate heat capacity expression $C_v = 324Nk_B(T/\theta_D)^3$ [92]. This shift in behavior underscores the dual influence of both classical and quantum mechanics on heat capacity, as well as the intriguing complexity of the material properties under study.

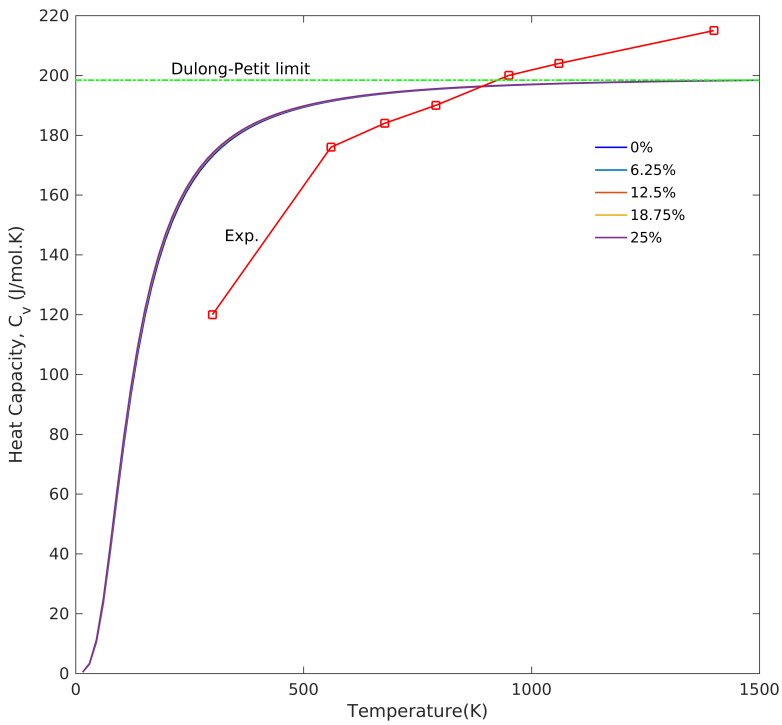

Figure 13: Heat capacity, C_v, based on Debye model for various Eu^{3+} concentrations. The red line with squares indicates experimental data for the molar heat capacity, C_p, of pure YSO obtained by Sun et al. [90].

To evaluate the predicted heat capacity, the experimental values of heat capacity, C_p, obtained by Sun et al. [90] are superimposed on the predicted curve. As can be seen, except at the two extremes (300 K and 1400 K), the predicted model agrees with the experimental data points. If corrections to C_p and C_v were taken into consideration, the predicted curve would be in better agreement with an experiment on the left-hand side. The correction values range between 1 and 8 K at room temperature and reach a maximum at the melting point, where the correction value would be equal to 10% of C_v.

In the wake of examining the mechanical and thermodynamical attributes of both YSO and Eu-doped YSO, our subsequent step encompasses the derivation of piezo-optic constants. A detailed procedure for extracting these photoelastic constants can be found in Paper II, and the results are available in Table 2. The choice of functional for our calculations was based on calculated dielectric

Table 2: piezo-optic constants of Eu:Y_2SiO_5, π_{ij}. Unit=Brewsters, 1B = 10^{-12} Pa^{-1}.

YSO	π_{11}	π_{12}	π_{13}	π_{15}	π_{21}	π_{22}	π_{23}	π_{25}	π_{31}	π_{32}
PBE0-D3	-0.603	0.880	1.184	-1.223	0.164	0.551	0.557	-0.131	0.337	0.725
Eu:YSO	π_{11}	π_{12}	π_{13}	π_{15}	π_{21}	π_{22}	π_{23}	π_{25}	π_{31}	π_{32}
PBE0-D3	-0.634	1.921	1.457	-1.229	0.195	1.580	0.815	-0.131	0.478	1.611
YSO	π_{33}	π_{35}	π_{44}	π_{46}	π_{51}	π_{52}	π_{53}	π_{55}	π_{64}	π_{66}
PBE0-D3	0.313	0.365	-0.353	-0.037	-0.504	-0.073	0.459	-0.594	0.117	-1.476
Eu:YSO	π_{33}	π_{35}	π_{44}	π_{46}	π_{51}	π_{52}	π_{53}	π_{55}	π_{64}	π_{66}
PBE0-D3	0.440	0.489	0.032	-0.268	-0.442	-0.281	0.269	-0.572	0.025	-1.526

constants, where PBE0 functional provided values closest to our experimental observations of dielectric constants. In an ideal scenario, our methodology's accuracy would be confirmed by comparing our calculated photoelastic constants with experimental equivalents. However, for both pure and Eu-doped YSO, such data is currently unavailable. As a workaround, we validated our calculated piezo-optic constants via their application in FEM simulations. In these simulations, we applied loads and post-processed the results using the calculated piezo-optic constants. If the refractive index resulting from these simulations, after the load application, aligns with the available experimental refractive index under similar conditions, we can assert that our piezo-optic constants are correctly determined. To perform a comparative analysis, we utilized the measured values of relative permittivity from the study by Carvalho et al. [93]. These values denote the relative permittivity of pure YSO crystal against varying temperatures. As the YSO crystal is a biaxial dielectric material with known refractive indices at optical frequencies, its permittivity plays a crucial role in this comparison. Following this, we commenced with the application of thermal stress on the YSO crystal. The temperature model employed is a ther-

Table 3: Comparison of measured and calculated refractive indices versus temperature for pure YSO. The measured data is taken from [93].

	measured			**calculated**		
Temp. (K)	n_{D1}	n_b	n_{D2}	n_{D1}	n_b	n_{D2}
6	1.749(1174)	1.787(5427)	1.817(0071)	1.757(7000)	1.762(100094)	1.778(9001)
10	1.749(1174)	1.787(5427)	1.817(0071)	1.757(7001)	1.762(100156)	1.778(9002)
20	1.749(1276)	1.787(5528)	1.817(0162)	1.757(7002)	1.762(100313)	1.778(9004)
30	1.749(1687)	1.787(5952)	1.817(0529)	1.757(7004)	1.762(100469)	1.778(9007)
40	1.749(2575)	1.787(6784)	1.817(1321)	1.757(7005)	1.762(100626)	1.778(9009)
50	1.749(3836)	1.787(7965)	1.817(2445)	1.757(7006)	1.762(100782)	1.778(9011)
70	1.749(7664)	1.788(1770)	1.817(6818)	1.757(7009)	1.762(101095)	1.778(9016)
296	1.760(1088)	1.795(3696)	1.830(0966)	1.757(8983)	1.762(305584)	1.779(2097)
100	1.7(5035)	1.7(8859)	1.8(18360635)	1.7(5770)	1.7(6210)	1.7(7890)
500	1.7(8046)	1.8(0887)	1.8(5505)	1.7(5832)	1.7(6274)	1.7(7986)
1000	1.8(7438)	1.8(6975)	1.9(7115)	1.7(5933)	1.7(6366)	1.7(8127)

momechanical one, where any temperature exceeding 0 K incites a mechanical load on the crystal, thereby inducing stress on the unit cell.

Our calculated results can be substantiated through a direct comparison with empirical data sourced from Carvalho et al. [93]. A side-by-side representation of the corresponding values for our measurements and calculations is presented in Table 3, with data points spanning from 6 to 296 K. Remarkably, for the D_1 orientation, the deviation in our point-to-point comparison is minimal. Additionally, the percentage of error remains unchanged across the entire temperature range as can be seen in Table 4. For the sake of specificity, the maximum errors at D_1, b, and D_2 stand at 0.49, 1.84, and 2.78 respectively. With this, we can claim that our calculated piezo-optic constants are fairly credible.

It's noteworthy that for direction b and D_2, the error appears to escalate with rising temperature. To gain deeper insight into the error magnitude at elevated temperatures, I employed a fitted curve to project the error beyond room temperature. The final three rows in Table 3 & 4, exhibit the values of the measured refractive indices and the projected data. A considerable surge in error is noticeable for the 500 and 1000 K markers. It is important to note that the operational temperature for some RE-activated phosphors is around room temperature or slightly above. For example, the operating temperature for laser stabilization purposes is at cryogenic levels [4, 25], while for some regular phosphor applications, such as LEDs, the operational temperature is closer to room temperature or slightly above [94]. Therefore, we can confidently state that the model's output is consistent with experimental values and suitable for practical applications.

Having established the model and verified its capacity to yield reasonable results, I could now proceed to examine the variations in the refractive indices relative

Table 4: The discrepancy between the measured and the predicted refractive indices.

	Error		
Temp. (K)	Err.D_1 (%)	Err.b (%)	Err.D_2 (%)
6	0.490	1.423	2.097
10	0.490	1.423	2.097
20	0.490	1.423	2.097
30	0.487	1.426	2.099
40	0.482	1.430	2.103
50	0.475	1.437	2.109
70	0.453	1.458	2.133
296	0.125	1.841	2.780
100	0.419	1.481	2.169
500	1.243	2.550	4.052
1000	6.083	5.610	9.543

to the temperature of Eu-doped YSO. The outcomes of these calculations are presented in Figure 14. Consistent with observations made for the pure system, the doped system also exhibits a linear trend in its refractive indices. Therefore, it is reasonable to conclude that the thermo-optic coefficient (dn/dT) for both RE-doped YSO can be approximated by a linear curve, at least within the range of cryogenic to room temperature.

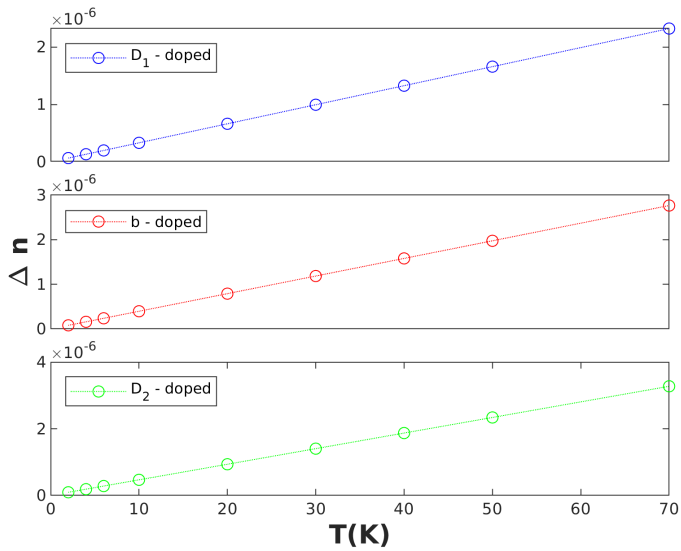

Figure 14: The variation of refractive indices in Eu-doped YSO with respect to temperature.

Using the values depicted in Figure 14 and the relation in Equation 56 as well

as Equation 64 we would be able to observe the resonance frequency shift of the Eu-doped YSO cavity as it is depicted in Figure 15.

$$f = \lambda / c \tag{64}$$

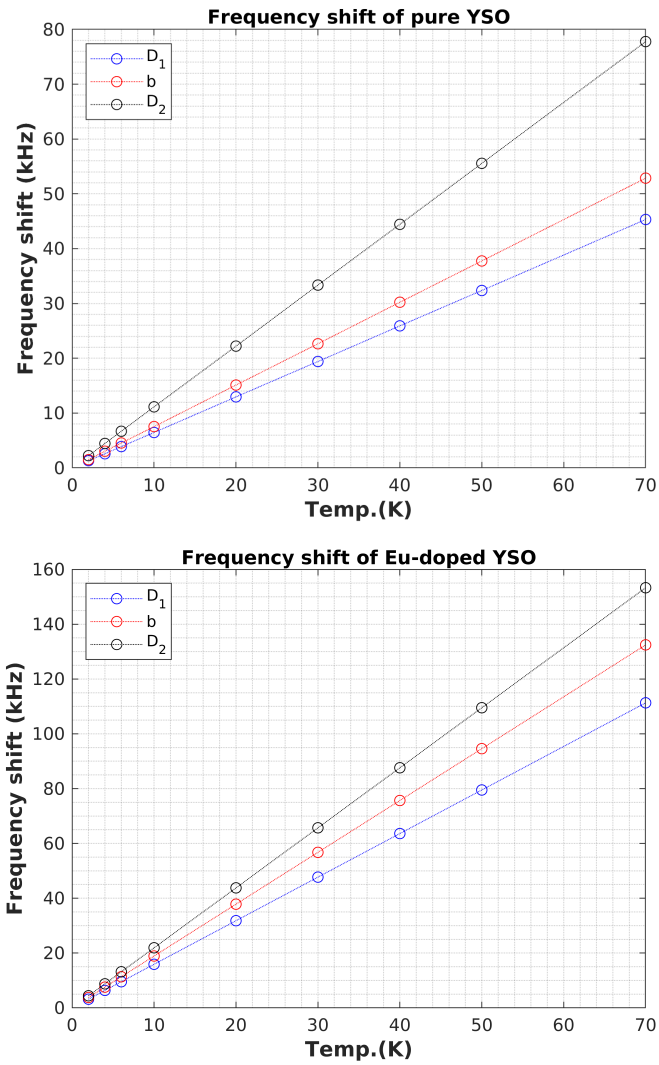

Figure 15: Shift of resonance frequency in pure and Eu-doped YSO.

Next, we are going to investigate the effect of the direct application of a compression and tensile load on the crystal to see how n is changing in different

Table 5: The rate of change of resonance frequency (df/dP) for pure & Eu-doped YSO with respect to applied load.

LoadAxis	Doped	n_{D_1}	n_b	n_{D_2}
D_1	no	-0.0869	0.0761	0.0886
D_1	yes	-0.0960	0.1381	0.1517
D_2	no	0.1375	0.0957	0.1174
D_2	yes	0.2810	0.2424	0.2465
D_1D_2	no	0.1318	0.0952	0.1169
D_1D_2	yes	0.2754	0.2402	0.2448
Hydrost.	no	-0.1616	-0.1071	-0.1179
Hydrost.	yes	-0.2818	-0.2399	-0.2399

orientations. For this, we again are going to apply pressure on the crystal in the FE simulation in which we obtained the stress tensor. This tensor is then further post-processed using the piezo-optic tensor to obtain the variation of the refractive indices with respect to the applied load. Figure 16 shows the variation of n with respect to load in D_1, D_2, D_1D_2 directions as well as the hydrostatic pressure. The linear behavior of the trends could be probably due to the fact that the piezo-optic constants are extracted based on Pockels' effect. The interesting points here are the slope of the hydrostatic pressure and the proximity of the D_2 and D_1D_2. As you can see in all figures the maximum magnitude of change is related to hydrostatic pressure, and the curves corresponding to D_2 and D_1D_2 are almost overlapping which might be explained due to the larger magnitude of n in D_2 direction.

The doped crystal as it is depicted in Figure 17, follows the same trend as the pure system. To understand the difference between the pure and the doped system, we have compared the rate of change of resonance frequencies for the pure and doped system in Table 5. In the table, it is clear that the doping yields a steeper slope, in terms of slope's magnitude, in all orientations. Therefore, one may infer that doping increases the rate of change in refractive indices, and consequently the resonance frequency. Unfortunately, there are no such data to confirm this for YSO, however, Soharab et al. [95] have performed an analysis of refractive index versus Nd concentration in $GdVO_4$, and the results agree with the increasing trend of refractive indices with dopant concentration.

The primary significance of implementing this workflow lies in its practicality. Conducting experiments to determine refractive indices and to measure changes in these indices, which subsequently affect the OPL, can be a tedious and time-consuming process. This complexity can be significantly reduced by adopting simulations such as the one presented here. Furthermore, our demonstration of this workflow's effectiveness for Eu-doped YSO implies a straightforward adaptation of the same process for other Ln-doped YSO systems. This adaptability

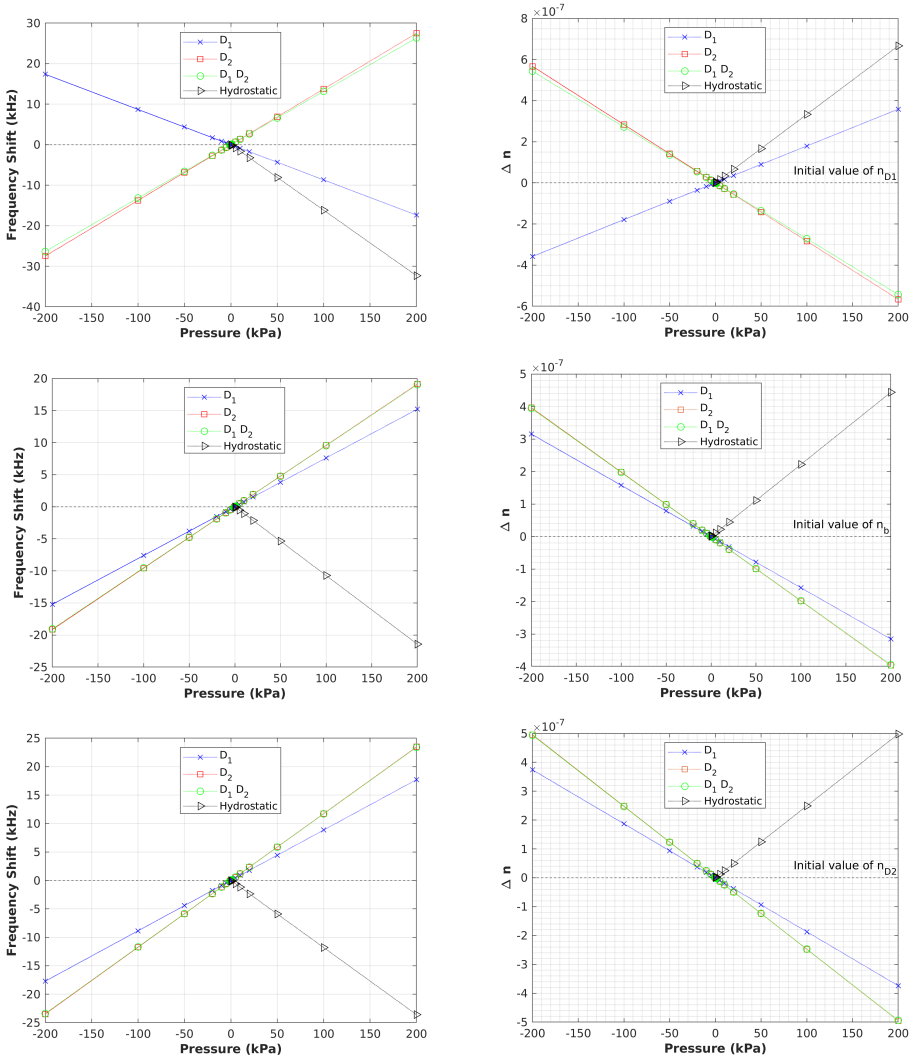

Figure 16: The refractive indices and frequency shift of pure YSO.

significantly simplifies the investigation of a broad range of Ln-doped YSO systems.

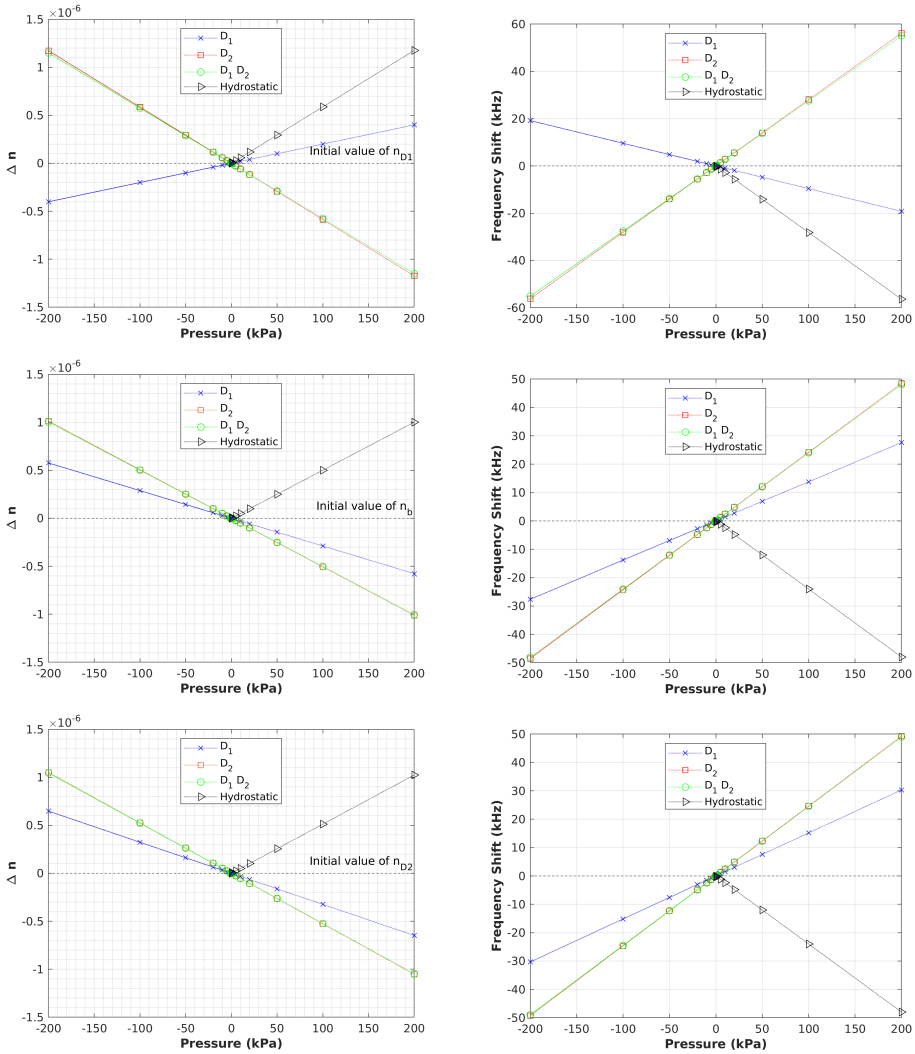

Figure 17: The refractive indices and frequency shift of Eu-doped YSO.

4.2 Phosphor

The luminescent properties of optical materials doped with RE elements are determined by the energy transition between the 4f and 5d orbitals of the RE ions. This transition involves the absorption and emission of light, which is the basis of phosphors. Phosphors are materials that can convert high-frequency light to low-frequency light through electronic transitions [96, 97]. Figure 18 shows one of the mainstream applications of the phosphors which is wLED. A common

example of a phosphor is YSO: Ce, which is widely used as a blue phosphor in various applications, such as radiation detection devices [98]. Moreover, the energy difference between the 4f and 5d orbitals directly impacts the efficiency of light conversion in these materials. So, accurate prediction of these transition energies is essential for the engineering of efficient light sources [99].

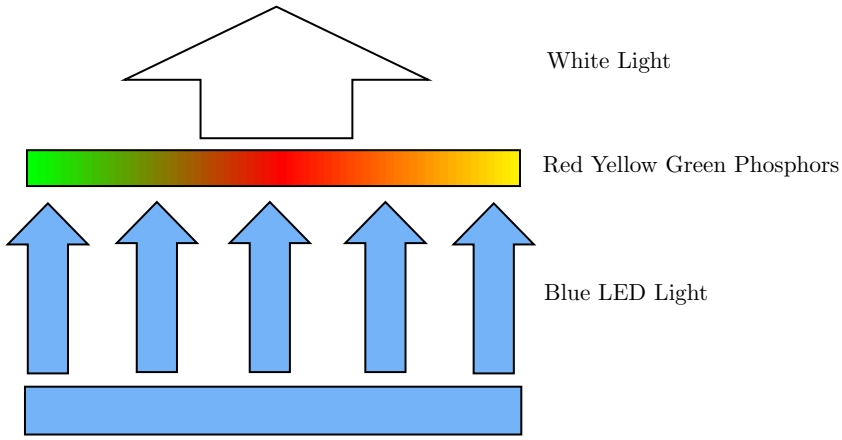

Figure 18: Schematic of a wLED using phosphor.

In the introductory section of this thesis, it was noted that due to the inherent limitations of the DFT approach in dealing with SIE, it is suggested to incorporate a segment of HF calculations. The HF approach is immune to these SIE issues and thus provides a balance, reducing the burden and high computational cost associated with highly precise methods like the *GW* approximation. A prominent player in this context is the screened hybrid functional HSE, which has demonstrated superior performance in our work and others [100]. Moreover, the earlier studies [69, 101] of the CDFT approach have been performed with the DFT+U approach where one has to tune the effective U parameter to adjust the location of 4f states in the band gap whereas we employ CDFT to find the location of 4f electrons in the band gap. Therefore, DFT+U is not applicable and we are proposing to use HSE functional instead.

The conventional HSE parameters are not universally optimal. Specifically, the mixing parameter, which plays a crucial role in the efficiency and accuracy of the HSE functional, is dependent on the effective static dielectric constant, ε_∞, of the material under consideration [102]. This dependency adds an additional layer of complexity to our computations and indicates that the choice of HSE parameters should be tailored to the specific material to achieve reliable and accurate results. Accordingly, the determination of specific HSE parameters

for a given material could yield results that are comparable in quality to those derived from more complex multi-body methods like the *GW* approximation. While there are several studies [103, 104] that showcased improved results following the tuning of HSE parameters, we decided to test this proposition on Ce-doped YVO_4 as the aforementioned studies are mainly on semiconductors and not insulators. The choice of the material was primarily guided by the availability of experimental data, allowing for the validation of our results. We were also particularly interested in investigating a lanthanide-doped laser material. Therefore, in paper III, we utilized an HSE-tuned hybrid functional to explore the effect of Ce doping on the optical properties of YVO_4.

Figure 19 displays the results of refractive indices calculations for Ce-doped YVO_4 using AM05 functionals. An observable anomaly in this figure indicates refractive indices nearing infinity in the infrared region for Ce-doped YVO_4, evident in both xx (n_o (a)) and zz (n_e (b)) directions. Despite the considerable Ce^{3+} concentration, 25%, the refractive index should begin at a lower value. Due to the unavailability of experimental refractive index data for Ce^{3+}-doped YVO_4, values from Yb-doped YVO_4 used as a benchmark. The refractive index for 8% and 15% doped Yb^{3+} for xx- and zz-directions are 2.021, 2.023 and 2.253, 2.250, respectively [105]. However, Figure 20 shows refractive indices for 25% Ce-doped YVO4 as $n_{xx} = 2.296$ and $n_{zz} = 2.409$ at E=0, which is in good agreement with the aforementioned experimental values. Therefore, it can be claimed that the inconsistency is mostly addressed in curves determined by the $HSE06^{15\%}$ functional, as shown in Figure 20.

The tuned-HSE, $HSE06^{15\%}$, curve reveals a blue shift of nearly 1 eV in both refractive index directions in comparison to the AM05 pure curve. While tuned-HSE shows a steady incline towards the end of the visible spectrum followed by a UV peak, the AM05 curve exhibits its peak at the visible spectrum's tail. In doped structures, a significant value spike at $E = 0$ is observed for refractive indices in both directions, as illustrated in Figure 20 (a & b). Notably, the 6.25% doped system has a refractive index value of 1.95 in the xx-direction and 2.73 in the zz-direction at $E = 0$, the lowest and highest among doped systems, respectively. Post this surge, a decreasing trend in the infrared sector is witnessed in both directions for doped systems, with a more evident decline in the zz-direction. The largest discrepancy between configurations is at the infrared zone, precisely around $E = 0$, with deviations of 0.69 in the xx-direction and 0.30 in the zz-direction. Finally, experimental values for the pure structure, plotted between 0.92 and 2.58 eV, were recorded by Shi et al. at room temperature (20°C) [106]. The $HSE06^{15\%}$ functionals align closely with the experimental curve's gradient, with a more precise match in the zz-direction.

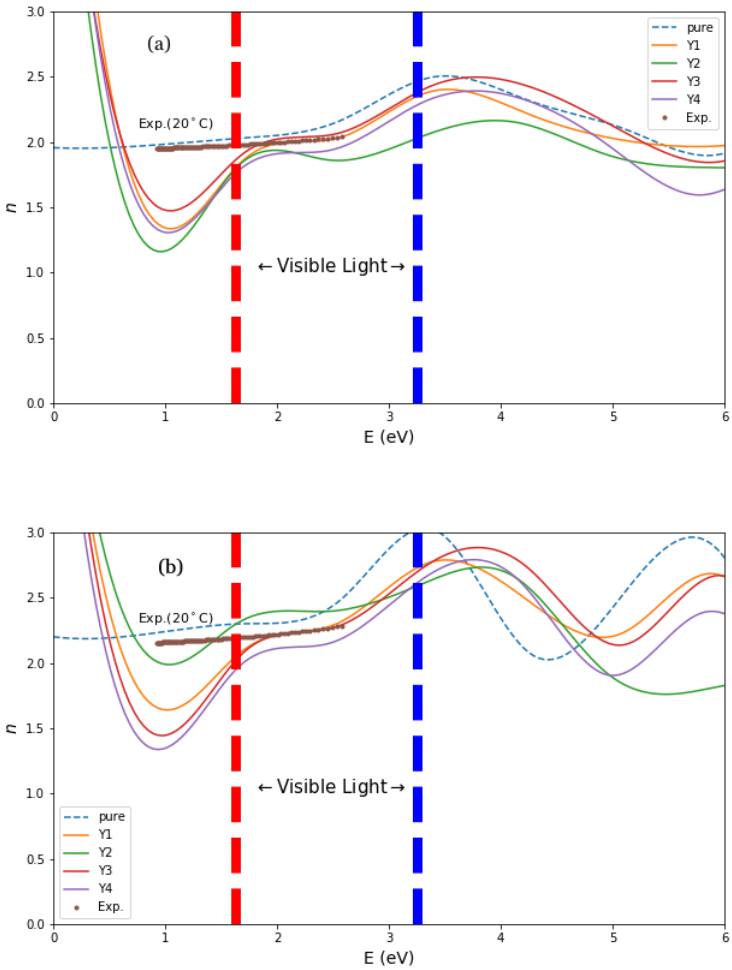

Figure 19: Refractive index of pure YVO_4 & Ce^{3+}-doped YVO_4 with the AM05 functional in xx-direction (a), and in zz-direction (b). The experimental values for refractive indices in both directions are taken from Shi et. al. [106].

The result of paper III proved the applicability of tuned-HSE on RE-doped optical material. Consequently, it was deemed suitable to use the same approach for CDFT calculations in Paper IV. First, however, the HSE parameters must have been tuned to the experimental band gap of the host material, YSO, just as we did in paper III and the results of the band gap are tabulated in Table 6. It reveals that the optimal value for the fraction of HF exact exchange α is 0.40, while the screening value μ is 0.19 and the result is depicted in Figure 21.

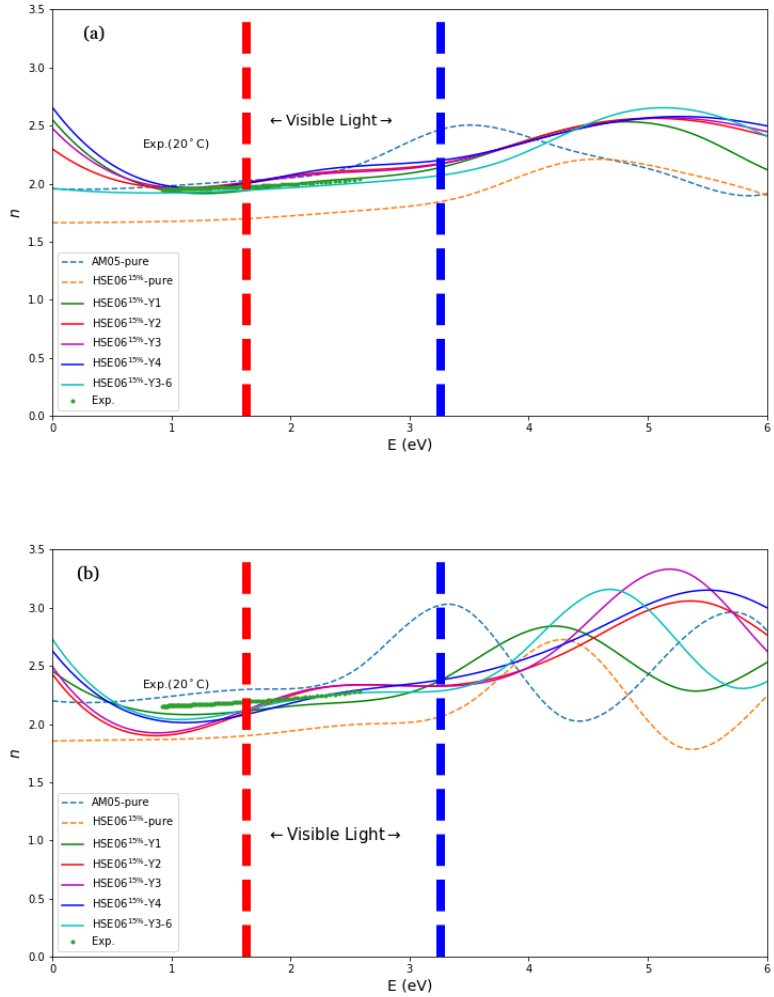

Figure 20: Refractive index of pure YVO_4 & Ce^{3+}-doped YVO_4 with the $HSE^{15\%}$ functional in xx-direction (a), and in zz-direction (b). The experimental values for refractive indices in both directions are taken from Shi et. al. [106].

Based on the CDFT approach, we manually evacuated the 4f levels and filled the lowest-lying 5d-like band to replicate a situation where a photon has removed the electron from valence 4f and transferred it to 5d. Later, the KS eigenvalues and total energies for ground states and excited states are obtained. As eigenvalues of KS can not be an alternative for optical transition levels [109, 110] only the difference between total energies (ΔSCF) of these two states can be considered for energy transition. So, ΔSCF as it is illustrated in Figure 22, absorption=

Table 6: Band gap of C2/c Y_2SiO_5. *This study:* *.

Material	Method	Band gap (eV)
Y_2SiO_5	Exp.	7.4 [107]
Y_2SiO_5	Exp.	7.4 [108]
Y_2SiO_5	PBE	4.82 [68]
Y_2SiO_5	PBE*	4.819
Y_2SiO_5	mBJ	6.14 [68]
Y_2SiO_5	HSE*	7.40

E_{abs} = e_0^* - g_0, is used to obtain the absorption energy. Then the manual constraint is removed and the perturbed lattice due to a change in its electronic configuration is relaxed with fixed lattice parameters. The resultant lattice denotes the $g1$ state in Figure 22, and the emission energy is calculated as emission = e_1^* - g_1. Once both absorption and emission energies are obtained the Stokes shift is obtained simply by subtracting these two from each other. Table 7 presents the calculated absorption and emission energies, as well as the Stokes shift.

Table 7: Calculated total energies, absorption, and emission energies of $Ce:Y_2SiO_5$ based on cDFT approach.

	Site1 (eV)	Site2 (eV)
E_{g_0}	-746.058	-745.744
$E_{e_0^*}$	-741.929	-741.868
E_{g_1}	-746.058	-745.744
$E_{e_1^*}$	-742.121	-742.346
E_{abs}	4.130	3.876
E_{abs}[111]	3.41	3.30
E_{ems}	3.938	3.398
E_{ems}[111]	3.12	2.73
Stokes shift	0.191	0.478

The observed data indicates a higher absorption and emission at both locations when calculated, as opposed to the experimental results. The divergence between these calculated and experimental values is roughly 0.7 eV for both types of energy at Ce1. However, at Ce2, this difference is slightly less, approximately 0.5 eV. The explanation for these disparities is the absence of SOC in the computational models. This can be further corroborated when referencing Figure 23, which illustrates that the SOC effect's magnitude is roughly 1000 cm^{-1} (or 0.12 eV).

The separate absorption and emission processes resulted in two distinct values for the SOC energy (E_{soc}). These were applied individually to account for the observed variances. For Ce1, during absorption and emission, the calculated

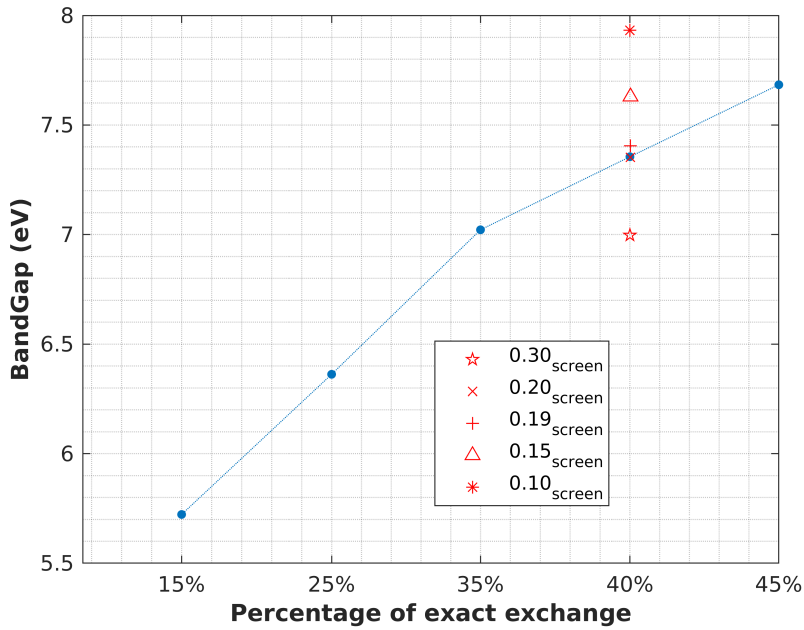

Figure 21: Tuning of HSE parameters based on the experimental band gap. The data points are extracted from gamma point-only calculations. As can be seen in the figure, the experimental band gap gets reproduced at $\alpha = 40\%$ exact exchange and $\omega = 0.19$ screening.

SOC effects are -0.65396 eV and -0.77685 eV, respectively. Similarly, for Ce2, these values are -0.65397 eV and -0.77850 eV, respectively. The SOC-corrected values for absorption and emission energy are presented in Table 8, obtained by adding the corresponding E_{soc} energies to the absorption and emission energies from Table 7.

Table 8: The SOC-corrected values of absorption and emission energies. The updated values are achieved by adding E_{soc} to the corresponding energies in Table 7. *This study:* *, Exp. [111].

	Site1 (eV)	Site2 (eV)
E_{abs}*	3.47	3.22
E_{abs}[111]	3.41	3.30
E_{ems}*	3.16	2.62
E_{ems}[111]	3.12	2.73
Stokes shift	0.314	0.602

The corrected values demonstrate improved agreement between the experimental and calculated results, especially for Ce1. For Ce1, the discrepancy in both absorption and emission is roughly 0.05 eV higher than the experimental value. In contrast, for Ce2, the difference is approximately 0.10 eV lower than the ex-

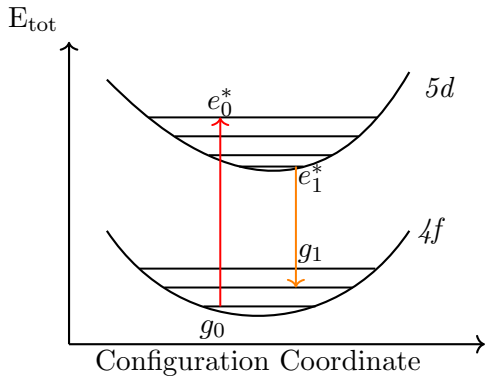

Figure 22: Configuration coordinate diagram. Depiction of absorption and emission energies.

perimental reading. It's important to note that these comparisons are based on a single experiment. However, if we compare the calculated absorption energy with the average of experiments listed in Table 9 for Ce1, where E_{avg}= 3.48 eV, then the discrepancy virtually disappears. This isn't the case for Ce2, where the average absorption energy from experiments at this site is 3.31 eV, while the calculated value is 3.22 eV, indicating a difference of 0.09 eV.

The previous data was limited to the transition energy for the 4f and the lowest-lying 5d level. For the remaining 5d levels, a different approach was used. A neutral HSE calculation provided the ground state location of 4f states when one of the 4f levels was occupied. Following this, a mono-positively charged supercell structure of Ce-doped YSO was relaxed using a modified HSE functional. This supercell structure gave us the electronic structure of excited states at the conduction level, along with the location of low-lying 5d states. It's crucial to note that atomic positions were fixed during this process in accordance with the Frank-Condon principle [112].

The 4f $\rightarrow$ 5d transition energies were obtained by subtracting the 4f eigenvalues of the neutral calculation from the Valence band maximum (VBM) of the corresponding host cell (**a** = 4f - VBM). The 5d eigenvalues of the Ce impurity were determined by examining the mono-positively charged calculation. The degeneracy of the 5d levels was removed due to the Crystal field (CF) effect, as depicted in Figure 26. This allowed us to obtain the 4f$\rightarrow$5d_i transition, where it represents different 5d orbital orientations. However, before we could obtain the transition energies, we subtracted the 5d_i eigenvalues from the corresponding host Conduction band minimum (CBM), (**b** = CBM - 5d_i). Finally, the transition energies between 4f$\rightarrow$5d_i can be obtained by subtracting **a** and **b** from the experimental and/or modified band gap energy of the host in its primitive cell,

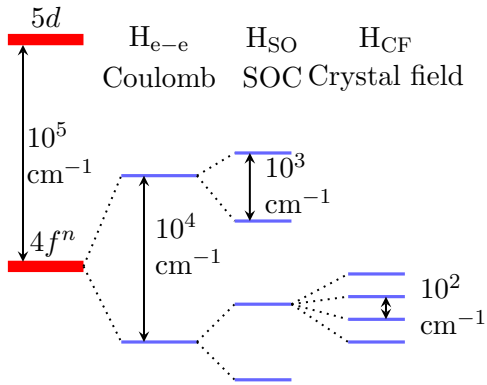

Figure 23: The source and magnitude of the energy level splittings in $4f^n \rightarrow 5d$ configuration.

4f→$5d_i$ = E_g - **a** - **b**. The entire transition process is depicted in Figure 24.

Figure 25 illustrates the projected density of states (Partial DOS (PDOS)) for Ce-doped YSO. The VBM and the CBM primarily consist of O_p and Y_d orbitals, respectively, a pattern similar to pure YSO. Notably, the 4f states are found within the band gap, closer to the VBM than to the CBM at both sites. This location differs from the DFT findings of Zhou et al. for Yb-doped YSO [68]. Zhou et al. located the 4f states 4.78 eV away from the VBM. In contrast, our results align closely with the findings of Ning et al. [113] and experimental measurements by Vedda et al. [114] for Ce: LSO. These findings suggest the VBM-4f gap in Ce: YSO concurs with previous studies on Ln-doped orthosilicates.

To delve further into the 4f ground state's location, it's helpful to compare it with the Dorenbos model [115, 116]. This empirical model is often used to estimate the energy of 4f of trivalent and divalent Ln ions in a given host lattice based on the lowest 4f → 5d level's peak position. Utilizing this model along with experimental data for Ce, and Pr-doped YSO and LSO, Kolk, and Dorenbos et al. estimated the probable location of 4f and the lowest lying 5d levels inside the band gap for all the Ln in YSO [117]. They estimated the 4f - VBM gap to be approximately 3.53 eV. Notably, they did not attribute this value to a specific site, Ce1 or Ce2, as their photocurrent experiment data did not show any doublet structure [117]. Whereas, our results with the inclusion of SOC have shifted the 4f ground states by 0.20 eV at both sites, reducing the 4f-VBM gap at Ce1 to 2.73 eV, and 2.70 eV at Ce2. This adjustment improves the agreement with the experimental work of Vedda et al. [114]. However, it is far from the 3.53 eV that is obtained Kolk et al.

As illustrated in Figure 26, we can observe the mono-positively charged state of

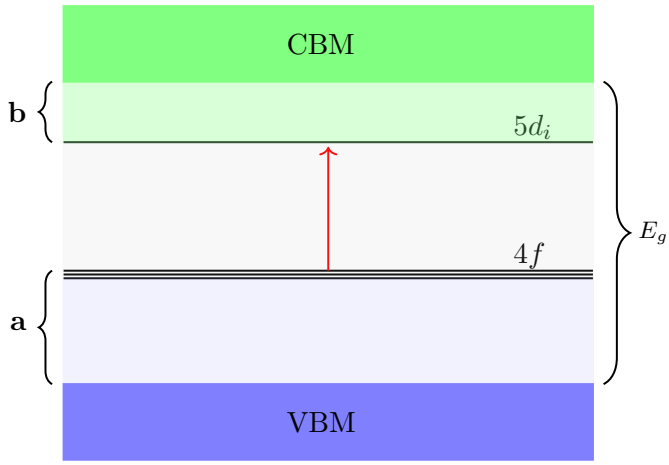

Figure 24: The transition energy: The host valence band maximum of the corresponding cell is subtracted from occupied 4f eigenvalue ($\mathbf{a} = 4f - VBM_{host}$). Then 5d eigenvalues that are obtained from +1-charged supercell calculation are subtracted from the host conduction band minimum of the corresponding cell ($\mathbf{b} = CBM_{host} - 5d$). Lastly, the two values are subtracted from the calculated host band gap, E_g=7.4013 eV. $4f \rightarrow 5d = E_g$ - **a** - **b**.

the Ce-doped YSO. Importantly, during this phase, the atomic configuration is carefully held constant, mirroring the neutral state of the Ce-doped YSO. This is performed to facilitate the excitonic effect, an interaction that occurs between the hole located at the VBM and the electron present in one of Ce's lowest-lying 5d states. In essence, the atomic positions are maintained to comply with the Franck-Condon principle, which states that during electronic transitions, the nuclear configuration remains unchanged due to the significant mass difference between electrons and nuclei. The lowest-lying 5d states in proximity to the CBM are seen to exhibit splitting due to the CF. These CF effects are highlighted in red for clarity. A comparative analysis of the red peaks at Ce1 and Ce2 reveals more pronounced visibility of the peaks, or splittings, at Ce2 for both SOC and non-SOC cases. This observation can be attributed to Ce2 being smaller than Ce1, leading to a stronger CF splitting at Ce2. These findings align with previous studies conducted using DFT+CASPT2 [67, 68].

In the lower portion of Figure 26, the influence of SOC is evident as it leads to the downward shifting of the $5d_i$ levels towards the VBM at both sites. Specifically, the shift of $5d_1$ at Ce1 is 0.38 eV, while it is 0.04 at Ce2. However, the direction of shift for the remaining levels is not consistent across the two sites. This shift, along with the presence of SOC, positions four out of the five lowest peaks within the band gap. This phenomenon is depicted with greater detail in Figure 27 and 28, which also showcases the spacing between these peaks and their shifts due to SOC. The $5d_{2-i}$ levels are identified based on their relative position to

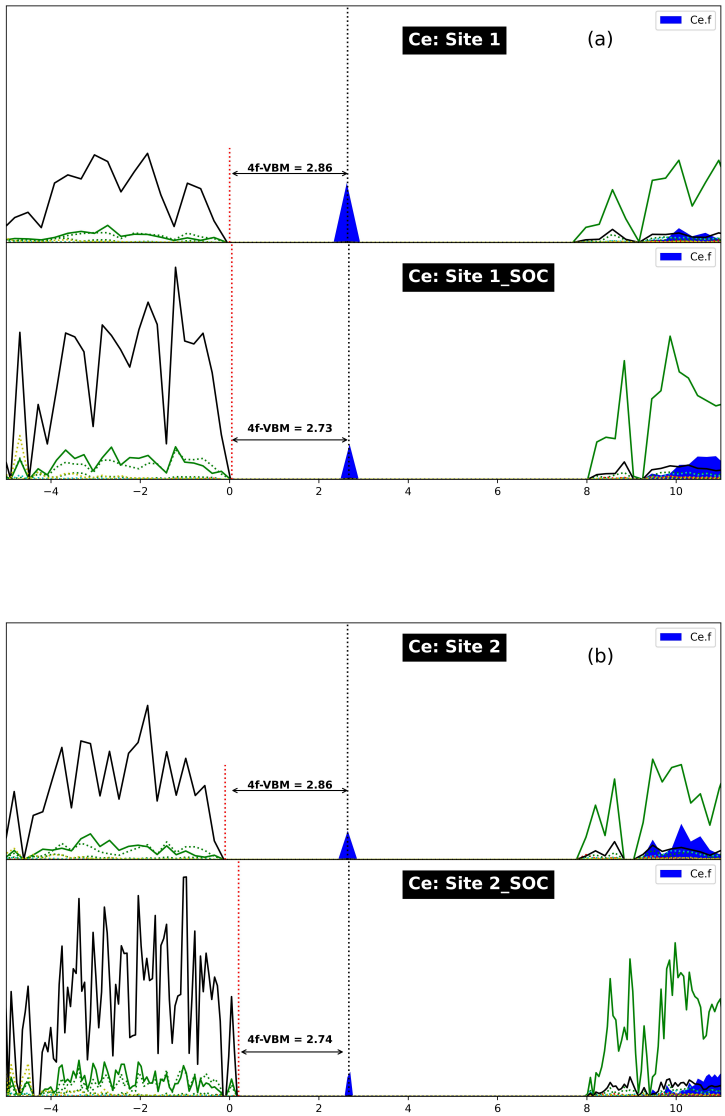

Figure 25: Orbital projected DOS of Ce-doped YSO, at Ce1 and Ce2 in a 1x2x1 supercell. The blue-filled states indicate the 4f states of the Ce^{3+} while they are occupied. The black dotted lines show the position of the Fermi level.

$5d_1$.

Table 9 describes the transition energies from 4f to 5d, observed at two unique

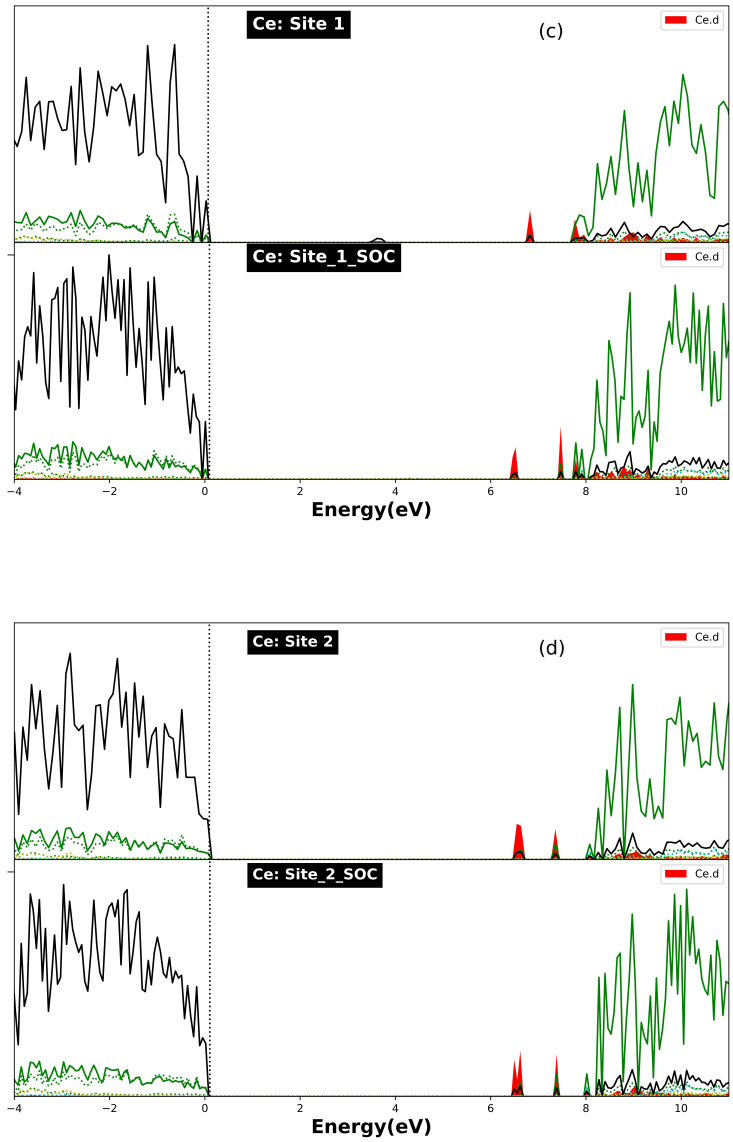

Figure 26: When 4f states are unoccupied, we can observe the 5d states in the band gap that are filled in red. The dotted lines show the position of the Fermi level.

sites in the YSO. The sixth row of the table features the computed values for the non-SOC but HSE functional of the supercell structure. Notably, the first transition value for Ce1 aligns closely with the experimental value. The disparity

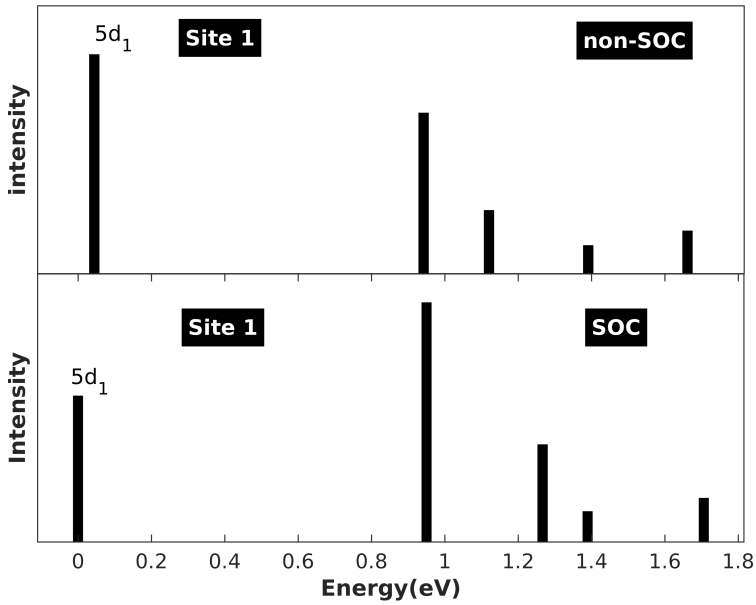

Figure 27: Location of $5d_i$ levels with respect to lowest lying $5d_1$ of the Ce atom at Ce1 with and without SOC.

between the calculated and experimental averages for the lowest-lying 5d level is 0.03 at Ce1 and 0.13 at Ce2. This suggests a more accurate definition of the lowest lying 5d level in relation to both experiment and AIMPs calculations at both impurity sites. However, the discrepancy between the calculated and experimental values rapidly expands for the remaining $5d_i$ levels, particularly for the last two $5d_4$ and $5d_5$ levels. These levels lack distinct sharp peaks, and the intensity is relatively weak, as indicated by our calculated data in Figures 27 and 28. These characteristics make measurements challenging, and likely account for the absence of data for these two levels, thereby precluding any comparisons.

The introduction of SOC has resulted in an almost uniform reduction of the energy of $5d_i$ levels at both sites. The energy shift is approximately 1600 cm^{-1} (0.2 eV) at Ce1, and 1000 cm^{-1} (0.1 eV) at Ce2. These findings are in alignment with those reported by Wen et al. [67] for Ce: YSO, where the shift was around 0.12 and 0.1 eV for Ce1 and Ce2, respectively. Similarly, Ning et al. reported a 1000 cm^{-1} energy shift at both sites of Ce: LSO [113]. Noteworthy, however, is the distinction between the current study and the aforementioned ones: while the previous studies reported an increase in 5d levels due to SOC, we observed

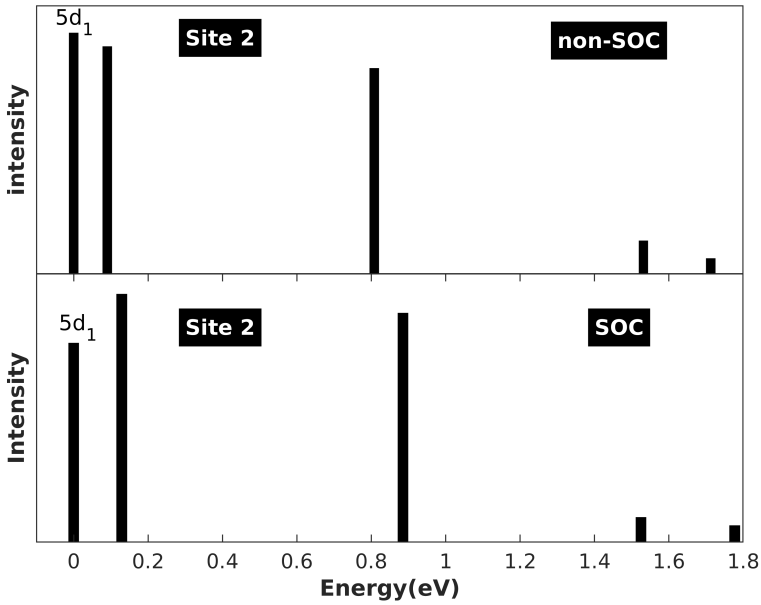

Figure 28: Location of $5d_i$ levels with respect to lowest lying $5d_1$ of the Ce atom at Ce2 with and without SOC.

Table 9: Transition energies, $4f \rightarrow 5d_i$. The procedure for the calculated value in this table is depicted in Figure 24. *This study: *.*

			$4f \rightarrow 5d_i$=1-5(eV)				
Ion	Site	Method	1	2	3	4	5
Ce^{3+}	Ce1	Exp.[111]	3.41	4.03	4.54	-	-
Ce^{3+}	Ce1	Exp.[118]	3.55	4.19	4.68	-	-
Ce^{3+}	Ce1	Exp.[119]	3.48	4.13	4.72	-	-
Ce^{3+}	Ce1	Exp_{avg}	3.48	4.11	4.65	-	-
Ce^{3+}	Ce1	CASPT2[67]	3.41	4.03	4.46	5.75	6.35
Ce^{3+}	Ce1	HSE*	3.511	4.45	4.64	4.92	5.21
Ce^{3+}	Ce1	HSE + SOC*	3.27	4.21	4.53	4.65	4.97
Ce^{3+}	Ce1	CASPT2+SOC[67]	3.53	4.16	4.59	5.89	6.49
Ce^{3+}	Ce2	Exp.[111]	3.30	3.80	-	-	-
Ce^{3+}	Ce2	Exp.[118]	3.32	3.78	4.79	-	-
Ce^{3+}	Ce2	Exp.[119]	3.31	3.79	4.78	-	-
Ce^{3+}	Ce2	Exp_{avg}	3.31	3.79	4.78	-	-
Ce^{3+}	Ce2	CASPT2[67]	3.44	3.64	3.91	6.29	7.09
Ce^{3+}	Ce2	HSE*	3.44	3.50	4.22	4.85	5.21
Ce^{3+}	Ce2	HSE + SOC*	3.30	3.43	4.15	4.79	5.09
Ce^{3+}	Ce2	CASPT2+SOC[67]	3.52	3.76	4.04	6.42	7.21

a decrease in 5d energy levels in our work.

As we observed earlier it is possible to find the 4f location in Ce-doped YSO with an application using a constrained occupancy approach coupled with the HSE+SOC method. As we mentioned earlier, however, the goal of this approach is to provide a generic approach to find the 4f to 5d transition energies of the RE-doped materials in a reasonable computational time in which the designation of the 4f electrons in the band gap is a central feature. So, it is important to check the applicability of this technique on other RE elements and host materials. This could potentially be an alternative to locating the 4f electrons in other host materials with any RE element. To further strengthen the applicability of this approach we have performed similar calculations of 4f→5d energies for Pr^{3+}-doped YSO. The results are shown in Table 10. Further validation for the rest

Table 10: Calculated total energies, absorption, and emission energies of Pr: YSO. The SOC corrected values are obtained via the addition of E_{SOC} to absorption or emission energies.

Pr: YSO	Site1 (eV)	SOC-corr.	Site2 (eV)	SOC-corr.
E_{g_0}	-755.108	-	-754.414	-
$E_{e_0^*}$	-749.553	-1.0	-749.021	-0.907
E_{g_1}	-754.690	-1.05	-750.353	-0.934
$E_{e_1^*}$	-749.978	-	-754.414	-
E_{abs}	5.554	4.553	5.392	4.485
abs. Exp[120]	5.040	5.040	5.040	5.040
E_{ems}	4.712	3.660	4.060	3.126
ems. Exp[120]	4.508	4.508	4.508	4.508
ΔS	0.842	0.893	1.332	1.358
ΔS [120]	0.628	0.628	0.628	0.628

of the RE-doped YSO is limited due to a lack of experimental data. However, we managed to find experimental work on transition energies of the Pr: YSO. The authors did not distinguish between the two sites in their measurements. Therefore, we have used their measurement of the 4f to 5d transition energies to compare with our calculated values for both site1 and site2, as shown in Table 10. At site1, the discrepancies between absorption and emission are: 0.514 and 0.204 eV respectively. If we add the effect of the SOC (listed in the Table under the column name SOC-corr.), the absorption discrepancy decreases to 0.487 eV but the emission discrepancy increases to 0.848 eV. At site2, the discrepancies are 0.352 and 0.448 eV for absorption and emission respectively, while adding SOC effect widens the discrepancies to 0.555 and 1.382 eV. As the comparison between calculated and measured data provides lower error at site1, we have assumed the experimental data to be measured for site1. Based on this assumption, the error for the absorption and emission are 10.19% and 4.52%, respectively.

Although the agreement between calculated and experimental results is not as good as the agreement that we have observed for Ce-doped YSO where the errors were 1.75% and 1.28% for absorption and emission energies, the approach has provided rather qualitative results without the required hassle of the experiment. Furthermore, the comparison is done with only one available experiment and the indistinguishable site symmetry.

5 Summary and Future Work

5.1 Summary

Optical materials are substances that can manipulate light in various ways, and they have many applications in optical instruments and devices, such as lasers, lenses, mirrors, filters, sensors, and displays. However, the properties of optical materials are often complex and difficult to measure or predict experimentally. Therefore, there is a need for theoretical methods that can help understand and optimize the performance of optical materials for different purposes. In this thesis, we have investigated fresh approaches that could improve our existing knowledge of these materials and hopefully aid in the discovery and design of new materials. In particular, we have discussed the optimization of RE-doped YSO for its application as a laser host material and phosphor.

In the initial phase, we attempted to enhance the efficiency of optical setups. Harnessing the multi-scale modeling workflow, we have managed to calculate the thermo-optic coefficients (dn/dT) of pure and Eu-doped YSO. To achieve this the piezo-optic constants were extracted with the application of DFPT, and the calculated constant was validated using the measured value of the dn/dT for the pure YSO. For the selected temperature interval (6 - 296 K) the maximum error between calculated and measured values was at 2.78% in D_2 direction. The main discrepancy between the developed model and the measured data is the type of polynomials that they fit in. While the measured data follow a quadratic equation the calculated data shows a linear behavior. This must be due to the fact that we have extracted the piezo-optic constant based on Pockels' effect which is a linear approach in its origin. So, to decrease the discrepancy between calculated and measured data non-linear effects known as Kerr's effect should be added to the process of piezo-optic extraction. Nevertheless, the workflow produces reasonable results for at least the selected temperature interval. The produced results presented in Table 3 are important as they enable the estimation of thermo-optic coefficients, which is crucial for the optimization and design of the optical cavity.

Using the piezo-optic post-processing method, we successfully observed variations in refractive indices for different applied loads and their respective frequency shifts. Our observations indicate that hydrostatic pressure induces the most significant variation in the refractive index. Furthermore, a linear relationship exists between the applied load and the change in refractive index n.

Doping amplifies the variation magnitude, regardless of its orientation or magnitude of the applied load. Thus, it can be inferred that an increase in impurity concentration amplifies the variation in n and subsequently affects the resonance frequency.

Rare Earth (RE) activated phosphors have gained widespread attention for display applications due to their unique luminescence mechanisms. Selecting the ideal lattice is vital in the fabrication of these phosphors, as it directly influences emission efficiency, stability, and a range of other properties. To enhance the understanding and development of these phosphors, identifying potential host candidates is of paramount importance.

In this work, we've proposed a theoretical approach that leans on the CDFT. This method is distinctive as it minimizes reliance on empirical or experimental data to predict and identify the location of the 4f and 5d energy levels in Lanthanides. The relevance of this process lies in the fact that the energy levels of 4f and 5d significantly affect emission characteristics. In some instances, transitions encompassing these energy levels are the primary reasons for the observed luminescence.

Many conventional methods, like *GW* and CASSCF, are not always applicable to larger molecules or solids. They often depend on empirical data to accurately identify the 4f and 5d levels. In contrast, our approach, drawing its foundations from DFT, offers a simpler yet effective alternative. As it's been tailored based on a singular calibration against host materials' experimental values, this method proves effective in examining a diverse range of RE-doped optical materials to discern the most suitable phosphor candidates.

Due to the simplicity of the current technique with respect to wave function approaches namely AIMPs, this technique can be a good alternative for at least qualitative assessment of phosphors and identification of optical properties in laser materials. Besides, since this technique does not require any prior data as is the case with AIMPs and empirical models, it could be more promising for applications such as high-throughput of phosphors. It should be noted that the applicability of this approach for the rest of the Ln group, and other host materials remains to be seen, although we have tested and validated the approach for Pr-doped YSO.

5.2 Future work

As you have noticed in the thesis there are two separate sections that each deal with an application of RE-doped optical materials. Our findings were enlightening. We identified a discrepancy in the refractive index of around 2.7% between calculated and measured values, but it's crucial to note that this observation was specific to a temperature spectrum ranging from cryogenic levels to room temperature. Further insights revealed a pronounced value concerning the rate of change of the refractive index with respect to pressure. However, a limitation that became evident was our model's linear trend assumption. This might have its roots in our reliance on Pockel's effect for extracting photoelastic constants. As we move forward, it's imperative to incorporate non-linear dynamics, specifically Kerr's effect.

In our latter approach, we've noted that the positioning of the 4f and 5d energy levels within the band gap holds significant importance. As highlighted in our results section, the primary challenge remains the absence of adequate experimental data. Hence, to validate our approach, it's essential to apply our framework to RE-doped materials for which comparative data exists.

6 References

[1] Jialiang Xu and Xian-He Bu. Optical properties and applications of crystalline materials. *Advanced Optical Materials*, 9(23):2102394, 2021.

[2] Zhe Yang, Kan Chen, Chen-ge Wang, Xuan She, Nan Li, and Xiao-wu Shu. A photonic crystal beam splitter used for light path multiplexing: synergy of tir and pbg light guiding. *Optical and Quantum Electronics*, 52:1–8, 2020.

[3] Asim Kumar Roy Choudhury. *Principles of colour and appearance measurement: Object appearance, colour perception and instrumental measurement*. Elsevier, 2014.

[4] Michael J. Thorpe, Lars Rippe, Tara M. Fortier, Matthew S. Kirchner, and Till Rosenband. Frequency stabilization to 6 × 10-16 via spectral-hole burning. *Nature Photonics*, 5(11):688–693, sep 2011.

[5] Kalaivani Srigurunathan, Rugmani Meenambal, Anupam Guleria, Dinesh Kumar, José Maria da Fonte Ferreira, and Sanjeevi Kannan. Unveiling the effects of rare-earth substitutions on the structure, mechanical, optical, and imaging features of zro2 for biomedical applications. *ACS Biomaterials Science & Engineering*, 5(4):1725–1743, 2019. PMID: 33405549.

[6] Yuichi Nakamura, Shingo Korekawa, Hideya Aoki, Shinichiro Mito, and Pang Boey Lim. Effects of al or ga substitution on the optical properties of bi-substituted rare earth iron garnets for magnetic hologram memory. In *International Symposium on Imaging, Sensing, and Optical Memory*, page ITuAF_02. Optica Publishing Group, 2022.

[7] Yulong Wang, Wentao Zhang, Xianfei Chen, Haiying Du, Junfeng Li, and Kehui Qiu. Influence of al3+/p5+ ions substitution on the structure and luminescence properties of sr2sio4:eu2+ phosphors for white light emitting diodes. *Ceramics International*, 43(2):2824–2828, 2017.

[8] Hirotaka Takahashi and Yuta Matsushima. Investigation on luminescent properties of rare earth doped mullite phosphors and the occupation site of the doped rare earths. *Journal of The Electrochemical Society*, 166(9):B3209, may 2019.

[9] Marie Krečmarová, Rodolfo Canet-Albiach, Hamid Pashaei-Adl, Setatira Gorji, Guillermo Muñoz-Matutano, Miloš Nesládek, Juan P. Martínez-Pastor, and Juan F. Sánchez-Royo. Extrinsic effects on the optical

properties of surface color defects generated in hexagonal boron nitride nanosheets. *ACS Applied Materials & Interfaces*, 13(38):46105–46116, 2021. PMID: 34520163.

[10] Yang Zhao, Bing Yan, Xianxiao Liang, Shaoxiang Liu, Xuan Shi, and Hongquan Zhao. Engineering of vacancy defects in ws2 monolayer by rare-earth (er, tm, lu) doping: A first-principles study. *physica status solidi (b)*, n/a(n/a):2300055.

[11] Hongjie Zhang and Hong Zhang. Special issue: Rare earth luminescent materials. *Light: Science & Applications*, 11(1):260, Sep 2022.

[12] P. C. Ricci, C. M. Carbonaro, R. Corpino, C. Cannas, and M. Salis. Optical and structural characterization of terbium-doped y2sio5 phosphor particles. *The Journal of Physical Chemistry C*, 115(33):16630–16636, 2011.

[13] Ge Zhu, Zhipeng Ci, Qian Wang, Yan Wen, Shaochun Han, Yurong Shi, Shuangyu Xin, and Yuhua Wang. A new type of color tunable composite phosphor y 2 sio 5: Ce/y 3 al 5 o 12: Ce for field emission displays. *Journal of Materials Chemistry C*, 1(29):4490–4496, 2013.

[14] Wenli Zhou, Ye Li, Ronghuan Zhang, Jing Wang, Rui Zou, and Hongbin Liang. Ultraviolet to near-infrared downconversion of y2sio5: Ce3+, yb3+ nanobelt-poly-eva films. *Opt. Lett.*, 37(21):4437–4439, Nov 2012.

[15] C.W. Thiel, Thomas Böttger, and R.L. Cone. Rare-earth-doped materials for applications in quantum information storage and signal processing. *Journal of Luminescence*, 131(3):353–361, 2011. Selected papers from DPC'10.

[16] B. Julsgaard, A. Walther, S. Kröll, and L. Rippe. Understanding laser stabilization using spectral hole burning. *Opt. Express*, 15(18):11444–11465, Sep 2007.

[17] Hongjie Zhang and Hong Zhang. Rare earth luminescent materials. *Light: Science & Applications*, 11(1):260, 2022.

[18] Carla Cannas, Marina Mainas, Anna Musinu, Giorgio Piccaluga, Adolfo Speghini, and Marco Bettinelli. Nanocrystalline luminescent eu3+-doped y2sio5 prepared by sol–gel technique. *Optical Materials*, 27(9):1506–1510, 2005. Proceedings of the Third International Conference on Sol–Gel Materials: Research, Technology, Applications.

[19] Liping Xie, Hongwei Song, Yu Wang, Wen Xu, Xue Bai, and Biao Dong. Influence of concentration effect and au coating on photoluminescence properties of yvo4: Eu3+ nanoparticle colloids. *The Journal of Physical Chemistry C*, 114(21):9975–9980, 2010.

[20] NC Carvalho, Jean-Michel Le Floch, J Krupka, and ME Tobar. Multimode technique for the determination of the biaxial y2sio5 permittivity tensor from 300 to 6 k. *Applied Physics Letters*, 106(19):192904, 2015.

[21] Xi Zhang, Jixin Chen, Jie Zhang, Detian Wan, and Yanchun Zhou. High-temperature mechanical and thermal properties of h-bn/30vol%y_2sio_5 composite. *Ceramics International*, 41(9, Part A):10891–10896, 2015.

[22] Luigi Moretti, Mario Iodice, Francesco G. Della Corte, and Ivo Rendina. Temperature dependence of the thermo-optic coefficient of lithium niobate, from 300 to 515 K in the visible and infrared regions. *Journal of Applied Physics*, 98(3), 08 2005. 036101.

[23] Tso Yee Fan and John L. Daneu. Thermal coefficients of the optical path length and refractive index in yag. *Appl. Opt.*, 37(9):1635–1637, Mar 1998.

[24] Wounjhang Park and Jeong-Bong Lee. Mechanically tunable photonic crystal structure. *Applied Physics Letters*, 85(21):4845–4847, 11 2004.

[25] N. Galland, N. Lučić, B. Fang, S. Zhang, R. Le Targat, A. Ferrier, P. Goldner, S. Seidelin, and Y. Le Coq. Mechanical tunability of an ultranarrow spectral feature of a rare-earth-doped crystal via uniaxial stress. *Phys. Rev. Appl.*, 13:044022, Apr 2020.

[26] G. Kresse and J. Furthmüller. Efficiency of ab-initio total energy calculations for metals and semiconductors using a plane-wave basis set. *Computational Materials Science*, 6(1):15 – 50, 1996.

[27] Roberto Dovesi, Alessandro Erba, Roberto Orlando, Claudio M Zicovich-Wilson, Bartolomeo Civalleri, Lorenzo Maschio, Michel Rérat, Silvia Casassa, Jacopo Baima, Simone Salustro, et al. Quantum-mechanical condensed matter simulations with crystal. *Wiley Interdisciplinary Reviews: Computational Molecular Science*, 8(4):e1360, 2018.

[28] M. Born and R. Oppenheimer. Zur quantentheorie der molekeln. *Annalen der Physik*, 389(20):457–484, 1927.

[29] D. R. Hartree. The wave mechanics of an atom with a non-coulomb central field. part ii. some results and discussion. *Mathematical Proceedings of the Cambridge Philosophical Society*, 24(1):111–132, 1928.

[30] Vladimir Fock. Näherungsmethode zur lösung des quantenmechanischen mehrkörperproblems. *Zeitschrift für Physik*, 61:126–148, 1930.

[31] P. Hohenberg and W. Kohn. Inhomogeneous electron gas. *Phys. Rev.*, 136:B864–B871, Nov 1964.

[32] W. Kohn and L. J. Sham. Self-consistent equations including exchange and correlation effects. *Phys. Rev.*, 140:A1133–A1138, Nov 1965.

[33] W. Kohn and L. J. Sham. Self-consistent equations including exchange and correlation effects. *Phys. Rev.*, 140:A1133–A1138, Nov 1965.

[34] John P. Perdew, Kieron Burke, and Matthias Ernzerhof. Generalized gradient approximation made simple. *Phys. Rev. Lett.*, 77:3865–3868, Oct 1996.

[35] J. P. Perdew and Alex Zunger. Self-interaction correction to density-functional approximations for many-electron systems. *Phys. Rev. B*, 23:5048–5079, May 1981.

[36] Junwei Lucas Bao, Laura Gagliardi, and Donald G. Truhlar. Self-interaction error in density functional theory: An appraisal. *The Journal of Physical Chemistry Letters*, 9(9):2353–2358, 2018. PMID: 29624392.

[37] Jochen Heyd, Gustavo E Scuseria, and Matthias Ernzerhof. Hybrid functionals based on a screened coulomb potential. *The Journal of chemical physics*, 118(18):8207–8215, 2003.

[38] J Heyd, GE Scuseria, and M Ernzerhof. Erratum:[j. chem. phys. 118, 8207 (2003). *J. Chem. Phys.*, 124:219906, 2006.

[39] Joachim Paier, Martijn Marsman, K Hummer, Georg Kresse, Iann C Gerber, and János G Ángyán. Screened hybrid density functionals applied to solids. *The Journal of chemical physics*, 124(15):154709, 2006.

[40] James C. Phillips and Leonard Kleinman. New method for calculating wave functions in crystals and molecules. *Phys. Rev.*, 116:287–294, Oct 1959.

[41] Albert P. Bartók and Jonathan R. Yates. Ultrasoft pseudopotentials with kinetic energy density support: Implementing the tran-blaha potential. *Phys. Rev. B*, 99:235103, Jun 2019.

[42] A. Rafi M. Iasir and Karl D. Hammond. Pseudopotential for plane-wave density functional theory studies of metallic uranium. *Computational Materials Science*, 171:109221, 2020.

[43] David Vanderbilt. Soft self-consistent pseudopotentials in a generalized eigenvalue formalism. *Phys. Rev. B*, 41:7892–7895, Apr 1990.

[44] D. R. Hamann, M. Schlüter, and C. Chiang. Norm-conserving pseudopotentials. *Phys. Rev. Lett.*, 43:1494–1497, Nov 1979.

[45] Richard M. Martin. *Pseudopotentials*, page 204–232. Cambridge University Press, 2004.

[46] Giovanni Onida, Lucia Reining, and Angel Rubio. Electronic excitations: density-functional versus many-body green's-function approaches. *Rev. Mod. Phys.*, 74:601–659, Jun 2002.

[47] K. Held, C. Taranto, G. Rohringer, and A. Toschi. Hedin equations, gw, gw+dmft, and all that, 2011.

[48] Ferdi Aryasetiawan and Olle Gunnarsson. The gw method. *Reports on Progress in Physics*, 61(3):237, 1998.

[49] Lucia Reining. The gw approximation: content, successes and limitations. *WIREs Computational Molecular Science*, 8(3):e1344, 2018.

[50] Ying Yan, Jenny Karlsson, Lars Rippe, Andreas Walther, Diana Serrano, David Lindgren, Mats-erik Pistol, Stefan Kröll, Philippe Goldner, Lihe Zheng, and Jun Xu. Measurement of linewidths and permanent electric dipole moment change of the ce $4f$-$5d$ transition in y_2sio_5 for qubit readout scheme in rare-earth ion based quantum computing. *Phys. Rev. B*, 87:184205, May 2013.

[51] Cyrus E. Dreyer, Audrius Alkauskas, John L. Lyons, Anderson Janotti, and Chris G. Van de Walle. First-principles calculations of point defects for quantum technologies. *Annual Review of Materials Research*, 48(1):1–26, 2018.

[52] JM Tomczak, P Liu, A Toschi, G Kresse, and K Held. Merging gw with dmft and non-local correlations beyond. *The European Physical Journal Special Topics*, 226(11):2565–2590, 2017.

[53] Sangkook Choi, Andrey Kutepov, Kristjan Haule, Mark Van Schilfgaarde, and Gabriel Kotliar. First-principles treatment of mott insulators: linearized qsgw+ dmft approach. *Npj Quantum Materials*, 1(1):1–6, 2016.

[54] Tianyu Zhu and Garnet Kin-Lic Chan. Ab initio full cell $gw + \mathrm{DMFT}$ for correlated materials. *Phys. Rev. X*, 11:021006, Apr 2021.

[55] C David Sherrill and Henry F Schaefer III. The configuration interaction method: Advances in highly correlated approaches. In *Advances in quantum chemistry*, volume 34, pages 143–269. Elsevier, 1999.

[56] *Multiconfigurational SCF Theory*, chapter 9, pages 103–130. John Wiley & Sons, Ltd, 2016.

[57] Attila Szabó and Neil S. Ostlund. Modern quantum chemistry : introduction to advanced electronic structure theory. 1982.

[58] M.A.L. Marques and E.K.U. Gross. Time-dependent density functional theory. *Annual Review of Physical Chemistry*, 55(1):427–455, 2004. PMID: 15117259.

[59] M. Lourenço Neto, K.L. Agra, J. Suassuna Filho, and F.E. Jorge. Tddft calculations and photoacoustic spectroscopy experiments used to identify phenolic acid functional biomolecules in brazilian tropical fruits in natura. *Spectrochimica Acta Part A: Molecular and Biomolecular Spectroscopy*, 193:249–257, 2018.

[60] Erich Runge and E. K. U. Gross. Density-functional theory for time-dependent systems. *Phys. Rev. Lett.*, 52:997–1000, Mar 1984.

[61] P. H. Dederichs, S. Blügel, R. Zeller, and H. Akai. Ground states of constrained systems: Application to cerium impurities. *Phys. Rev. Lett.*, 53:2512–2515, Dec 1984.

[62] Benjamin Kaduk, Tim Kowalczyk, and Troy Van Voorhis. Constrained density functional theory. *Chemical Reviews*, 112(1):321–370, 2012. PMID: 22077560.

[63] Yu Jin, Marco Govoni, Gary Wolfowicz, Sean E. Sullivan, F. Joseph Heremans, David D. Awschalom, and Giulia Galli. Photoluminescence spectra of point defects in semiconductors: Validation of first-principles calculations. *Phys. Rev. Mater.*, 5:084603, Aug 2021.

[64] Christian S. Ahart, Kevin M. Rosso, and Jochen Blumberger. Implementation and validation of constrained density functional theory forces in the cp2k package. *Journal of Chemical Theory and Computation*, 18(7):4438–4446, 2022. PMID: 35700315.

[65] Simona Fantacci, Annapaola Migani, and Massimo Olivucci. Caspt2//casscf and tddft//casscf mapping of the excited state isomerization path of a minimal model of the retinal chromophore. *The Journal of Physical Chemistry A*, 108(7):1208–1213, 2004.

[66] Zoila Barandiarán and Luis Seijo. The ab initio model potential representation of the crystalline environment. Theoretical study of the local distortion on NaCl:Cu+. *The Journal of Chemical Physics*, 89(9):5739–5746, 11 1988.

[67] Jun Wen, Chang-Kui Duan, Lixin Ning, Yucheng Huang, Shengbao Zhan, Jie Zhang, and Min Yin. Spectroscopic distinctions between two types of ce3+ ions in x2-y2sio5: A theoretical investigation. *The Journal of Physical Chemistry A*, 118(27):4988–4994, 2014. PMID: 24953347.

[68] Xiaonan Zhou, Honggang Liu, Zhiyu He, Baojun Chen, and Jun Wu. Investigation of the electronic structure and optical, epr, and odmr spectroscopic properties for 171yb3+-doped y2sio5 crystal: A combined theoretical approach. *Inorganic Chemistry*, 59(18):13144–13152, 2020. PMID: 32865403.

[69] A. Canning, A. Chaudhry, R. Boutchko, and N. Grønbech-Jensen. First-principles study of luminescence in ce-doped inorganic scintillators. *Phys. Rev. B*, 83:125115, Mar 2011.

[70] Yongchao Jia, Anna Miglio, Samuel Poncé, Masayoshi Mikami, and Xavier Gonze. First-principles study of the luminescence of eu^{2+}-doped phosphors. *Phys. Rev. B*, 96:125132, Sep 2017.

[71] Yongchao Jia, Anna Miglio, Samuel Poncé, Xavier Gonze, and Masayoshi Mikami. First-principles study of ce^{3+}-doped lanthanum silicate nitride phosphors: Neutral excitation, stokes shift, and luminescent center identification. *Phys. Rev. B*, 93:155111, Apr 2016.

[72] Alan Corney. 355Resonant modes of optical cavities. In *Atomic and Laser Spectroscopy*. Oxford University Press, 10 2006.

[73] DA Long, Benjamin J Reschovsky, Feng Zhou, Yiliang Bao, Thomas W LeBrun, and JJ Gorman. Electro-optic frequency combs for rapid interrogation in cavity optomechanics. *Optics letters*, 46(3):645–648, 2021.

[74] Alok K. Singh, Lal Muanzuala, Atanu K. Mohanty, and Vasant Natarajan. Optical frequency metrology with an rb-stabilized ring-cavity resonator—study of cavity-dispersion errors. *J. Opt. Soc. Am. B*, 29(10):2734–2740, Oct 2012.

[75] Deshui Yu and Frank Vollmer. Active optomechanics. *Communications Physics*, 5(1):61, 2022.

[76] Yaowen Hu, Mengjie Yu, Di Zhu, Neil Sinclair, Amirhassan Shams-Ansari, Linbo Shao, Jeffrey Holzgrafe, Eric Puma, Mian Zhang, and Marko Lončar. On-chip electro-optic frequency shifters and beam splitters. *Nature*, 599(7886):587–593, 2021.

[77] Agata Cygan, Adam J Fleisher, Roman Ciuryło, Keith A Gillis, Joseph T Hodges, and Daniel Lisak. Cavity buildup dispersion spectroscopy. *Communications Physics*, 4(1):14, 2021.

[78] Markus Aspelmeyer, Tobias J. Kippenberg, and Florian Marquardt. Cavity optomechanics. *Rev. Mod. Phys.*, 86:1391–1452, Dec 2014.

[79] Warren Nagourney. 323Laser frequency stabilization and control systems. In *Quantum Electronics for Atomic Physics and Telecommunication*. Oxford University Press, 05 2014.

[80] Qun-Feng Chen, Andrei Troshyn, Ingo Ernsting, Steffen Kayser, Sergey Vasilyev, Alexander Nevsky, and Stephan Schiller. Spectrally narrow, long-term stable optical frequency reference based on a eu^{3+}:y_2sio_5 crystal at cryogenic temperature. *Phys. Rev. Lett.*, 107:223202, Nov 2011.

[81] Krishnamurthi Ramesh. *Developments in Photoelasticity: A renaissance*. IOP Publishing, 2021.

[82] C Li, Ch Wyon, and Richard Moncorge. Spectroscopic properties and fluorescence dynamics of er/sup 3+/and yb/sup 3+/in y/sub 2/sio/sub 5. *IEEE journal of quantum electronics*, 28(4):1209–1221, 1992.

[83] Jr. Jellison, Gerald E., Eliot D. Specht, Lynn A. Boatner, David J. Singh, and Charles L. Melcher. Spectroscopic refractive indices of monoclinic single crystal and ceramic lutetium oxyorthosilicate from 200 to 850 nm. *Journal of Applied Physics*, 112(6), 09 2012. 063524.

[84] Tamma Satya Narasimhamurty. *Photoelastic and electro-optic properties of crystals*. Springer Science & Business Media, 2012.

[85] John Frederick Nye et al. *Physical properties of crystals: their representation by tensors and matrices*. Oxford university press, 1985.

[86] Moises Levy. 1. introduction to fundamentals of elastic constants. In Moises Levy, Henry E. Bass, and Richard Stern, editors, *Modern Acoustical Techniques for the Measurennent of Mechanical Properties*, volume 39 of *Experimental Methods in the Physical Sciences*, pages 1–35. Academic Press, 2001.

[87] Marius Grundmann. The principal axes systems for the elastic properties of monoclinic gallia. *Scientific Reports*, 10(1):19486, 2020.

[88] G. Ramakrishna, H. Nagabhushana, B. Daruka Prasad, Y.S. Vidya, S.C. Sharma, K.S. Anantharaju, S.C. Prashantha, and Nityanand Choudhary. Spectroscopic properties of red emitting eu3+ doped y2sio5 nanophosphors for wled's on the basis of judd–ofelt analysis: Calotropis gigantea latex mediated synthesis. *Journal of Luminescence*, 181:153–163, 2017.

[89] N.W. Ashcroft, N.D. Mermin, and et al. *Solid State Physics*. HRW international editions. Holt, Rinehart and Winston, 1976.

[90] Ziqi Sun, Meishuan Li, and Yanchun Zhou. Thermal properties of single-phase y2sio5. *Journal of the European Ceramic Society*, 29(4):551–557, 2009.

[91] Yixiu Luo, Jiemin Wang, Jingyang Wang, Junning Li, and Zijun Hu. Theoretical predictions on elastic stiffness and intrinsic thermal conductivities of yttrium silicates. *Journal of the American Ceramic Society*, 97(3):945–951, 2014.

[92] Charles Kittel et al. *Introduction to solid state physics*, volume 8. Wiley New York, 1976.

[93] N. C. Carvalho, J-M. Le Floch, J. Krupka, and M. E. Tobar. Multi-mode technique for the determination of the biaxial y_2sio_5 permittivity tensor from 300 to 6 k. *Applied Physics Letters*, 106(19):192904, may 2015.

[94] Irfan Ayoub, Umer Mushtaq, Nisar Hussain, Seemin Rubab, Rakesh Sehgal, Hendrik C. Swart, and Vijay Kumar. 8 - rare-earth-activated phosphors for led applications. In Vikas Dubey, Neha Dubey, Marta Michalska Domańska, M. Jayasimhadri, and Sanjay J. Dhoble, editors, *Rare-Earth-Activated Phosphors*, pages 205–240. Elsevier, 2022.

[95] M Soharab, Indranil Bhaumik, R Bhatt, A Saxena, and AK Karnal. Effect of nd doping on the refractive index and thermo-optic coefficient of gdvo 4 single crystals. *Applied Physics B*, 125:1–14, 2019.

[96] Saniya Khan, Yatish R Parauha, Dharma K Halwar, and Sanjay J Dhoble. Rare earth (re) doped color tunable phosphors for white light emitting diodes. *Journal of Physics: Conference Series*, 1913(1):012017, may 2021.

[97] Isha Gupta, Sitender Singh, Shri Bhagwan, and Devender Singh. Rare earth (re) doped phosphors and their emerging applications: A review. *Ceramics International*, 47(14):19282–19303, 2021.

[98] Nikoletta Laczai, László Kovács, Laura Kocsor, and László Bencs. Influence of lif additive and cerium doping on photoluminescence properties of polycrystalline yso and lyso. *Materials Research Bulletin*, 133:111018, 2021.

[99] M. Stephan, M. Zachau, M. Gröting, O. Karplak, V. Eyert, K.C. Mishra, and P.C. Schmidt. A theoretical investigation of 4f→5d transition of trivalent rare earth ions in fluorides and complex oxides. *Journal of Luminescence*, 114(3):255–266, 2005.

[100] Pedro Borlido, Jonathan Schmidt, Ahmad W Huran, Fabien Tran, Miguel AL Marques, and Silvana Botti. Exchange-correlation functionals for band gaps of solids: benchmark, reparametrization and machine learning. *npj Computational Materials*, 6(1):1–17, 2020.

[101] Benjamin Kaduk, Tim Kowalczyk, and Troy Van Voorhis. Constrained density functional theory. *Chemical Reviews*, 112(1):321–370, 2012. PMID: 22077560.

[102] Miguel A. L. Marques, Julien Vidal, Micael J. T. Oliveira, Lucia Reining, and Silvana Botti. Density-based mixing parameter for hybrid functionals. *Phys. Rev. B*, 83:035119, Jan 2011.

[103] D. O. Demchenko and M. A. Reshchikov. Koopmans' tuning of HSE hybrid density functional for calculations of defects in semiconductors: A case study of carbon acceptor in GaN. *Journal of Applied Physics*, 127(15):155701, 04 2020.

[104] D. Kirk Lewis, Ashwin Ramasubramaniam, and Sahar Sharifzadeh. Tuned and screened range-separated hybrid density functional theory for describing electronic and optical properties of defective gallium nitride. *Phys. Rev. Mater.*, 4:063803, Jun 2020.

[105] M. Soharab, Indranil Bhaumik, R. Bhatt, A. Saxena, A. K. Karnal, and P. K. Gupta. Effect of Yb^{3+} doping on the refractive index and thermo-optic coefficient of yvo4 single crystals. *Appl. Opt.*, 56(6):1682–1688, Feb 2017.

[106] H-S Shi, G Zhang, and H-Y Shen. Measurement of principal refractive indices and the thermal refractive index coefficients of yttrium vanadate. *Journal of Synthetic Crystals*, 30(1):85–88, 2001.

[107] L.E. Muresan, Y. Karabulut, A.I. Cadis, I. Perhaita, A. Canimoglu, J. Garcia Guinea, L. Barbu Tudoran, D. Silipas, M. Ayvacikli, and N. Can.

Tunable luminescence of broadband-excited and narrow line green emitting y2sio5:ce3+, tb3+ phosphor. *Journal of Alloys and Compounds*, 658:356–366, 2016.

[108] Xinguo Zhang, Liya Zhou, Qi Pang, Jianxin Shi, and Menglian Gong. Tunable luminescence and ce3+ → tb3+ → eu3+ energy transfer of broadband-excited and narrow line red emitting y2sio5:ce3+, tb3+, eu3+ phosphor. *The Journal of Physical Chemistry C*, 118(14):7591–7598, 2014.

[109] Ralf Stowasser and Roald Hoffmann. What do the kohn- sham orbitals and eigenvalues mean? *Journal of the american chemical society*, 121(14):3414–3420, 1999.

[110] A. Savin, C.J. Umrigar, and Xavier Gonze. Relationship of kohn–sham eigenvalues to excitation energies. *Chemical Physics Letters*, 288(2):391–395, 1998.

[111] Weerapong Chewpraditkul, Chalerm Wanarak, Tomasz Szczesniak, Marek Moszynski, Vitezslav Jary, Alena Beitlerova, and Martin Nikl. Comparison of absorption, luminescence and scintillation characteristics in lu1.95y0.05sio5:ce,ca and y2sio5:ce scintillators. *Optical Materials*, 35(9):1679–1684, 2013.

[112] J.B. Coon, R.E. DeWames, and C.M. Loyd. The franck-condon principle and the structures of excited electronic states of molecules. *Journal of Molecular Spectroscopy*, 8(1):285–299, 1962.

[113] Lixin Ning, Lihua Lin, Lanlan Li, Changbao Wu, Chang-kui Duan, Yongfan Zhang, and Luis Seijo. Electronic properties and 4f → 5d transitions in ce-doped lu2sio5: a theoretical investigation. *J. Mater. Chem.*, 22:13723–13731, 2012.

[114] A. Vedda, M. Nikl, M. Fasoli, E. Mihokova, J. Pejchal, M. Dusek, G. Ren, C. R. Stanek, K. J. McClellan, and D. D. Byler. Thermally stimulated tunneling in rare-earth-doped oxyorthosilicates. *Phys. Rev. B*, 78:195123, Nov 2008.

[115] Pieter Dorenbos. Ce3+ 5d-centroid shift and vacuum referred 4f-electron binding energies of all lanthanide impurities in 150 different compounds. *Journal of Luminescence*, 135:93–104, 2013.

[116] Pieter Dorenbos. Modeling the chemical shift of lanthanide $4f$ electron binding energies. *Phys. Rev. B*, 85:165107, Apr 2012.

[117] E. van der Kolk, P. Dorenbos, C. W. E. van Eijk, S. A. Basun, G. F. Imbusch, and W. M. Yen. $5d$ electron delocalization of ce^{3+} and pr^{3+} in y_2Sio_5 and lu_2Sio_5. *Phys. Rev. B*, 71:165120, Apr 2005.

[118] V. Jary, A. Krasnikov, M. Nikl, and S. Zazubovich. Origin of slow low-temperature luminescence in undoped and ce-doped y2sio5 and lu2sio5 single crystals. *physica status solidi (b)*, 252(2):274–281, 2015.

[119] V. Babin, V.V. Laguta, M. Nikl, J. Pejchal, A. Yoshikawa, and S. Zazubovich. On the luminescence origin in y2sio5:ce and lu2sio5:ce single crystals. *Optical Materials*, 103:109832, 2020.

[120] A. Novoselov, H. Ogino, A. Yoshikawa, M. Nikl, J. Pejchal, A. Beitlerova, and T. Fukuda. Crystal growth, optical and luminescence properties of pr-doped y2sio5 single crystals. *Optical Materials*, 29(11):1381–1384, 2007.

Scientific publications

Author contributions

Paper I: First-principle investigation of doping effects on mechanical and thermodynamic properties of Y_2SiO_5

I did conceptualization, calculation, analysis, writing, and revision.

Paper II: A theoretical investigation of optical path length variation of Eu:Y_2SiO_5 (Submitted)

I did conceptualization, calculation, analysis, writing, and revision.

Paper III: Influence of impurity configuration on electronic and optical properties of Ce-doped YVO_4: Semi-local & Hybrid functionals

I did conceptualization, calculation, analysis, writing, and revision.

Paper IV: First-principles study of luminescence and electronic properties of Ce-doped Y_2SiO_5

I did conceptualization, calculation, analysis, writing, and revision.

Paper I

Amin Mirzai, Solveig Melin, Aylin Ahadi, P.A.T Olsson

First-principle investigation of doping effects on mechanical and thermodynamic properties of Y_2SiO_5

Mechanics of Materials

DOI: 10.1016/j.mechmat.2020.103739

Mechanics of Materials 154 (2021) 103739

Contents lists available at ScienceDirect

Mechanics of Materials

journal homepage: www.elsevier.com/locate/mecmat

First-principle investigation of doping effects on mechanical and thermodynamic properties of Y_2SiO_5

Amin Mirzai [a,*], Aylin Ahadi [a], Solveig Melin [a], P.A.T. Olsson [a,b]

[a] Department of Mechanical Engineering, Lund University, Box 118, SE-22100 Lund, Sweden
[b] Materials Science and Applied Mathematics, Malmö University, SE-20506 Malmö, Sweden

ARTICLE INFO

Keywords:
Monoclinic
Density functional theory
Rare-earth doping
Elastic moduli
Debye temperature
Heat capacity

ABSTRACT

We investigate the variation of elastic stiffness moduli and the thermodynamic properties of yttrium orthosilicate (Y_2SiO_5, YSO) under various doping concentrations of Eu^{3+} ions. The model is based on a low temperature approximation ($T<<\theta_D$) , and the plane-wave density functional theory (DFT) is used to carry out the calculations. The results show that the Eu^{3+} ions primarily occupy the Y_1 site of the basic molecule for all applied concentrations. The overall shear, bulk, and Young's moduli exhibit a decreasing trend with increasing Eu^{3+} concentration. The overall anisotropy shows a very small increase with increasing concentration. The Debye temperature as well as the Grünesien parameter for each concentration are predicted. Lastly, the predicted heat capacity at constant volume is calculated and compared to experimental values. Our study reveals that there is almost linear relationship between concentration and mechanical properties of YSO. The decrease of the Grünesien parameter with concentration increase might decrease the anharmonic effects in YSO, although this effect is small. In addition, the change in heat capacity with concentration rise is negligible.

1. Introduction

There has been substantial interest in the use of rare-earth (RE) ion-doped crystal materials as high-performance luminescent devices, light-emitting diodes, plasma panels, solid-state lasers, and use in laser frequency stabilization (Ricci et al., 2011; Thorpe et al., 2011). In order to improve the performance and efficiency of current devices and to develop new devices with higher brightness and resolution, researchers have been investigating numerous inorganic materials as a host for RE ions. A few candidates such as aluminum garnet ($Y_{3Al5O12}$), RE-orthovanadates ($REVO_4$) and yttrium silicates (Y_{2SiO_5}) have been examined in more detail due to their promising intrinsic properties. In particular, Y_{2SiO_5} (YSO) crystals have been found to have high chemical and thermal stability that is desirable for cathode luminescent phosphors (Saha et al., 2005). They also have negligible magnetic moment, which has made them appealing for quantum information and laser stabilization applications (Thorpe et al., 2011). YSO doped with RE ions such as Ce^{3+} and Eu^{3+} is used in applications for blue phosphor, Cr-doped YSO is used as a saturable absorber, and Tb-doped YSO is an efficient candidate for UV light-emitting-diodes (Ricci et al., 2011).

Although YSO is doped with RE ions in nearly in all its applications, little is known about the effects of doping on the properties of YSO. A few experimental studies on doping effects have indicated the need for further studies in this regard. For instance, Saha et al. (2005) report that doping not only has direct effects on the structural and the mechanical properties of YSO, but also affects the luminescent centers of Ghosh et al. (2006) noted that interband transitions depend on the phase of the crystal as well as the doping concentration percentage, which affects the emission intensity at the luminescent centers.

A few experimental and theoretical studies have been focused on the intrinsic properties of YSO crystals. For example, Ching et al. (2003) calculated the dielectric constants and band gap of YSO using the ab initio orthogonalized linear combination of atomic orbitals (OLCAO) method. The physical properties of YSO were later investigated experimentally for application as thermal barrier coatings (TBC) (Sun et al., 2009, 2008). To examine the selection of YSO as TBC in more detail, Luo et al. (2014) calculated the elastic stiffness and thermal properties of YSO using plane-wave DFT. Mock et al. (2018) also used the plane-wave DFT method to investigate anisotropy and phonon modes of pure YSO crystals by analyzing the dielectric tensor.

However, at present there is a lack of knowledge in the effects of doping on the mechanical and thermodynamic properties of YSO crystals. This knowledge is important in laser materials such as YSO since the residual heat from laser may affects the refractive index. This in turn causes stress-induced birefringence (or, in the case of YSO, trirefringence). Moreover, mechanical stress, for example from mounting the crystal, may also introduce photoelastic effects in the crystal, which

* Corresponding author.
E-mail address: amin.mirzai@mek.lth.se (A. Mirzai).

https://doi.org/10.1016/j.mechmat.2020.103739
Received 6 July 2020; Received in revised form 17 December 2020; Accepted 29 December 2020
Available online 2 January 2021

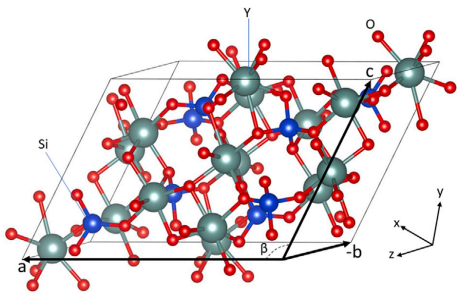

Fig. 1. Schematic of a YSO standard unit cell with 64 atoms and with ($B2/b$, 15) crystal structure. The constituents of basic molecules are Y, Si, and O, that are represented by gray, blue and red spheres, respectively. Lattice parameters are denoted as a, b, and c. (For interpretation of the references to colour in this figure legend, the reader is referred to the web version of this article.)

may slightly alter the polarization of the laser beam (Yoder, 2008). Therefore, it is important to have deeper knowledge about the physical properties of laser materials such as doped YSO so that the performance of practical laser systems can be improved. In this paper, we examine the effect of Eu^{3+} doping on the mechanical and thermodynamic properties of YSO to provide more accurate information for its application in the field of laser stabilization and luminescence. The main reason for the selection of Eu^{3+}, aside from its well-known coherence time (Thorpe et al., 2011) is its high sensitivity to crystal symmetry and the bond length of the lattice sites (Ghosh et al., 2006; Saha et al., 2005). The values of thermodynamic properties such as the Debye temperature, heat capacity, and mechanical properties such as bulk modulus, and Young's modulus as well as their directional components with respect to orientation might be beneficial in minimizing stress-induced trirefringence. We will provide the mechanical and thermodynamic properties of Eu-doped YSO crystal over a doping concentration range from 0% to 25%.

2. Crystal structure of Y_2SiO_5

YSO is a polymorphic crystal, forming two distinct crystal structures, denoted as X1 and X2. The X1 type is known as the low temperature phase since it forms at 1100°C, whereas the X2 type, known as the high temperature phase, forms at 1300°C (Ghosh et al., 2006).

In each phase, two unique C_1 coordination sites for yttrium ions exist, which will be referred to as Y_1 and Y_2, with coordination numbers of seven and nine for X1-YSO, and seven and six in X2-YSO, respectively. Both of these phases form a monoclinic crystal system. Fig. 1 shows a schematic of a YSO standard unit cell with basic constituents Y, Si and O. The unit cell has 64 atoms in total, which corresponds to 8 basic molecules of yttrium silicate, Y_{2SiO_5}. In standardized monoclinic crystals, only the b crystallographic axis is an axis of symmetry (Fig. 2). The relation between the Cartesian coordinate axes (x, y, z) and the crystallographic axes (a, b, c) of a monoclinic crystal is seen in Fig. 2.

There are 18 different groups of structures describing monoclinic systems in tables of crystallography (Mock et al., 2018). The specific group number of YSO is 15. The symmetry of a crystal structure is defined through space groups; X1 holds the space group $P2_1/b$ whereas X2 holds the $B2/b$ space group according to the international notation system (Sun et al., 2009; Luo et al., 2014).

The standard unit cell with the $B2/b$ space group has been chosen by many researchers along with several other alternatives in experimental as well as in theoretical studies. For example, Mock et al. (2018) used the $I2/b$ space group, while many researchers in the quantum information field (Wen et al., 2014) have focused on the standard

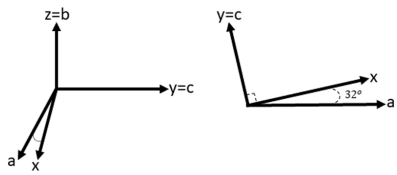

Fig. 2. Relation between the Cartesian coordinate axes (x, y, z) and the crystallographic axes (a, b, c) of a standard monoclinic YSO crystal.

alternative, that is, the $B2/b$ space group. In this study we will use the space group $B2/b$ too, since it has been found to be a good host for luminescent ions, and has numerous applications within photonics and bio-photonics (Ghosh et al., 2006).

In a monoclinic crystal system, the conventional unit cell is defined by primitive vectors a, b, and c of arbitrary length, with one of the vectors perpendicular to the other two. In addition, $B2/b$ is base-centered, and its unique axis b has a 2-fold rotation symmetry; hence, it is denoted $B2/b$.

3. Theory & method

3.1. Elastic properties

Elastic constants are fundamental properties that determine the response of a crystal to an externally applied load. They provide information on the nature of the chemical bonding as well as mechanical and structural stability of the solid. They are not only directly related to the equations of state and the phonon spectra, but also to the thermodynamic properties of solids such as specific heat, thermal conductivity, the Grüneisen parameter, and the Debye temperature. Since in standardized monoclinic crystals the crystallographic axis, b, is an axis of binary symmetry, there are 13 independent elements in the elastic stiffness matrix C_{ij}, given by Eq. (1) (Nye et al., 1985).

There are two main approaches to determine the elements c_{ij}. In the first approach, the stiffness matrix is determined by applying six finite distortions of the lattice, from which the elastic constants can be derived using the stress–strain relation. In the second approach, a distortion matrix is applied to find the strain–energy curve in order to obtain the elastic constants through a second-order expansion of the total energy with respect to the lattice strain components. It should be noted that the strain tensor has specific components for each crystal symmetry. The distortion matrix A for monoclinic systems is described by Söderlind (2002). The matrices A_i, $i = 1, 13$, are given in Appendix.

$$C_{ij} = \begin{pmatrix} c_{11} & c_{12} & c_{13} & 0 & c_{15} & 0 \\ \vdots & c_{22} & c_{23} & 0 & c_{25} & 0 \\ \vdots & \ddots & c_{33} & 0 & c_{35} & 0 \\ \vdots & \vdots & \ddots & c_{44} & 0 & c_{46} \\ \vdots & \cdots & \cdots & \ddots & c_{55} & 0 \\ \cdots & \cdots & \cdots & \cdots & \ddots & c_{66} \end{pmatrix} \tag{1}$$

Next, the elastic constants are checked to assess the stability of the doped crystals. This requires that the strain–energy must be positive for any homogeneous elastic deformation. The set of stability criteria for monoclinic structures are given in Eq. (2) (Nye et al., 1985)

$$\begin{aligned} &c_{11} > 0,\ c_{22} > 0,\ c_{33} > 0,\ c_{44} > 0,\ c_{55} > 0,\ c_{66} > 0, \\ &[c_{11} + c_{22} + c_{33} + 2(c_{12} + c_{13} + c_{23})] > 0, \\ &(c_{33}c_{55} - c_{35}^2) > 0,\ (c_{44}c_{66} - c_{46}^2) > 0, \\ &(c_{22} + c_{33} - 2c_{23}) > 0, \\ &[c_{22}(c_{33}c_{55} - c_{35}^2) + 2c_{23}c_{25}c_{35} - c_{23}^2c_{55} - c_{25}^2c_{33}] > 0, \\ &2[c_{15}c_{25}(c_{33}c_{12} - c_{13}c_{23}) + c_{15}c_{35}(c_{22}c_{13} - c_{12}c_{23}) \end{aligned}$$

$$+c_{25}c_{35}(c_{11}c_{23}-c_{12}c_{13})]-[c_{15}^2(c_{22}c_{33}-c_{23}^2)$$
$$+c_{25}^2(c_{11}c_{33}-c_{13}^2)+c_{35}^2(c_{11}c_{22}-c_{12}^2)+c_{55}d]>0,$$
$$d=c_{11}c_{22}c_{33}-c_{11}c_{23}^2-c_{22}c_{13}^2-c_{33}c_{12}^2+2c_{12}c_{13}c_{23}. \quad (2)$$

The values of the elastic moduli of the crystal can also be defined from the elastic constants c_{ij}, as suggested by Voigt et al. (Voigt et al., 1928), where B_V and G_V denote the bulk and the shear modulus, respectively.

$$B_V=\frac{1}{9}(c_{11}+c_{22}+c_{33}+2(c_{12}+c_{13}+c_{23})) \quad (3)$$

$$G_V=\frac{1}{15}(c_{11}+c_{22}+c_{33}+3(c_{44}+c_{55}+c_{66}))$$
$$-\frac{1}{15}(c_{12}+c_{13}+c_{23}) \quad (4)$$

Analogously, Reuß (1929) derived the bulk modulus B_R and the shear modulus G_R in terms of the elements of the compliance matrix S_{ij} as stated in following relations:

$$B_R=\frac{1}{s_{11}+s_{22}+s_{33}+2(s_{12}+s_{13}+s_{23})} \quad (5)$$

$$G_R=\frac{15}{4(s_{11}+s_{22}+s_{33})-4(s_{12}+s_{13}+s_{23})+3(s_{44}+s_{55}+s_{66})} \quad (6)$$

where the compliance matrix is the inverse of the stiffness matrix:

$$S_{ij}=(C^{-1})_{ij}. \quad (7)$$

Hill (1952) proved that the Voigt and the Reuss approaches are lower and upper bounds, respectively, of any crystalline structure. Therefore, it is common to use the arithmetic mean of the Voigt and the Reuss approximations to define B_H and G_H, known as the Voigt–Reuss–Hill (VRH) approximation or, simply, the Hill approximation.

$$B=B_H=\frac{B_V+B_R}{2}, \quad (8)$$

$$G=G_H=\frac{G_V+G_R}{2}. \quad (9)$$

Finally Young's modulus E and the Poisson's ratio ν are obtained using the following relationships (Hill, 1952)

$$E=\frac{9BG}{3B+G}, \quad (10)$$

$$\nu=\frac{3B-2G}{2(3B+G)}. \quad (11)$$

3.2. Thermodynamic properties

The Debye temperature θ_D is one of the fundamental parameters used to link the physical properties of solids such as specific heat, elastic constants, melting temperature, heat capacity, and bond strength. It is also used to distinguish between high and low temperature regimes. At low temperatures (T << θ_D), only the acoustic vibrations cause transverse vibration excitation. Therefore, calculation of the Debye temperature from elastic constants is equivalent to the values obtained using specific heat measurements (Ravindran et al., 1998). The Debye temperature can be calculated from the elastic constants using the Anderson relation (Anderson, 1963) given as

$$\theta_D=\frac{h}{k_B}[\frac{3n}{4\pi}(\frac{N_A\rho}{M})]^{1/3}v_m \quad (12)$$

where h is Planck's constant, k_B is Boltzmann's constant, n is the number of atoms per formula unit, N_A is Avogadro's number, ρ is the density of the unit cell, and M is the molecular weight. The average sound velocity v_m can be obtained from the longitudinal wave velocity v_l and the transverse wave velocity v_t through the following relationships (Anderson, 1963)

$$v_m=[\frac{1}{3}(\frac{2}{v_t^3}+\frac{1}{v_l^3})]^{-1/3}, \quad (13)$$

$$v_t=\sqrt{\frac{G}{\rho}}, \quad (14)$$

Table 1
Calculated bond length values of X2-YSO configuration.

Bond	Length (Å)	Bond	Length (Å)	Bond	Length (Å)
Y1-O1	2.239	Y2-O1	2.325	Si-O1	1.641
Y1-O2	2.589	Y2-O2	2.358	Si-O2	1.633
Y1-O3	2.334	Y2-O3	2.392	Si-O3	1.661
Y1-O4	2.379	Y2-O4	2.394	Si-O4	1.645
Y1-O5	2.367	Y2-O5	2.296	–	–
Y1-O6	2.337	Y2-O6	2.209	–	–
Y1-O7	2.329	–	–	–	–

$$v_l=\sqrt{\frac{B+\frac{4G}{3}}{\rho}}. \quad (15)$$

At temperatures above θ_D the thermal conductivity approaches a minimum value denoted as the minimum thermal conductivity, κ_{min}. The calculated values of the minimum thermal conductivity are derived from the following relation given by Clarke (2003)

$$\kappa_{min}\rightarrow 0.87K_BN_A^{2/3}\frac{n^{1/3}E^{1/2}}{M^{1/3}\rho^{1/6}}\rightarrow k_Bv_m(\frac{M}{n\rho N_A})^{(-2/3)}. \quad (16)$$

The Grüneisen parameter γ is a dimensionless parameter that links properties such as the expansion coefficient, bulk modulus, and specific heat in solids. The normal thermal expansion of solids due to anharmonicity of interatomic forces is often based on the Grüneisen constant as well. Thus the Grüneisen parameter basically provides a quantitative link between thermal and mechanical properties. It is also used to describe the change in vibration properties with respect to volume variation. Belomestnykh and Tesleva (2004) derived a simplified relation for the Grüneisen parameter using the Poisson ratio ν as follows:

$$\gamma=\frac{3}{2}\frac{1+\nu}{2-3\nu}. \quad (17)$$

Although there are several methods such as phonon calculation with DFT, and machine learning analysis of interatomic potentials to obtain the heat capacity, in low temperature cases one can compute the heat capacity, C_v, using the Debye model as follows (Ashcroft et al., 1976),

$$C_v=3nk_B[4D(\frac{\theta_D}{T})-\frac{3(\theta_D/T)}{exp(\theta_D/T)-1}]. \quad (18)$$

In Eq. (18), T is the temperature and $D(x)$ is the Debye function given as

$$D(x)=\frac{3}{x^3}\int_0^x\frac{t^3}{e^t-1}dt. \quad (19)$$

3.3. Computational details

A standard unit cell of YSO as depicted in Fig. 1 is chosen for the calculations. The initial atomic positions are taken from the Materials Project. The calculations are carried out by employing pseudopotential plane-wave DFT methodology as implemented in the Vienna Ab-initio Software Package (VASP) (Kresse and Furthmüller, 1996). The Eu: $4f^75d^06s^2$, Y: $4s^24p^64d^15s^2$, Si: $3s^23p^2$, and O: $2s^22p^4$ electrons are treated as valence electrons, whereas the core electrons and electron–ion interactions are determined using the projected augmented wave (PAW) method (Blöchl, 1994). The contribution due to exchange and correlation is expressed by the generalized gradient approximation (GGA) theory as described by Perdew–Burke–Ernzerhof (PBE) (Perdew et al., 1996).

The unit cell was optimized by setting the cut-off energy to 500 eV. The conjugate gradient algorithm is used to relax the system. The sampling of the Brillouin zone was done by implementing an automatically generated Γ-centered Monkhorst–Pack grid. In order to minimize the total energy, a 4 × 8 × 6 mesh was adopted for all calculations. A convergence threshold of 1×10^{-8} eV was used to reach self-consistency. The partial occupancy of orbitals was determined using the tetrahedron

Table 2
Volume and lattice parameters for YSO. *:*This study*.

Material	Method	Space group	V (Å^3)	a (Å)	b (Å)	c (Å)	β (o)
$Y_2SiO_5^*$	calc.	$B2/b$	880.52	14.51	6.81	10.51	122.08
Y_2SiO_5 Ching et al. (2003)	calc.	$B2/b$	895.95	14.09	6.80	10.72	119.46
Y_2SiO_5 Luo et al. (2014)	calc.	$B2/b$	812.51	14.25	6.59	10.23	122.30
Y_2SiO_5 SpringerMaterials (2016)	exper.	$B2/b$	852.00	14.41	6.72	10.41	122.20
Y_2SiO_5 O'Bryan et al. (1988)	exper.	$B2/b$	848.65	14.37	6.71	10.40	122.19

Table 3
Bond length values of site Y_1 as a function of Eu^{3+} concentration: 6.25%, 12.5%, 18.75%, 25%.

	Bond Length (Å)			
Bond	6.25(%)	12.5(%)	18.75(%)	25(%)
Eu1-O1	2.263	2.255	2.254	2.377
Eu1-O2	2.672	2.649	2.672	2.383
Eu1-O3	2.336	2.341	2.338	2.435
Eu1-O4	2.434	2.437	2.418	2.418
Eu1-O5	2.434	2.440	2.441	2.338
Eu1-O6	2.386	2.390	2.381	2.668
Eu1-O7	2.369	2.371	2.375	2.255
Aver.	2.414	2.412	2.411	2.411

method with Blöchl corrections. Further convergence criteria were set by restricting the maximum force per atom to below 0.0016 eV/Å and the maximum stress to below 0.034 GPa. Once the relaxed cell is obtained it is used for subsequent elastic constant calculations.

4. Results and discussion

4.1. Crystal structure of YSO

Table 1 shows the bond lengths between constituents of a pure YSO molecule in the X2-YSO configuration. The table shows that Y_1 is surrounded by seven oxygen atoms whereas Y_2 is surrounded by six.

Table 2 compares the volume, V, the lattice parameters, a, b, c and β of a pure YSO unit cell obtained in this study (marked by *), with the theoretical results of Luo et al. (2014) and Ching et al. (2003). The experimental values are also included in the table. As the table shows, the general agreement between the results is good, which confirms the reliability of the present study.

Fig. 3 shows that the volume of the crystal increases with percentage doping due to the difference in atomic radii of Y and Eu, which are 2.27 Å and 2.56 Å, respectively. Fig. 3 shows there is an almost linear relation between concentration percentage and volume. The same holds for the relative change in the lattice parameters.

It is important to note that the doping process occurs through a substitution in the host crystal, that is, Eu^{3+} ions replace Y^{3+} ions. The substitution of Y^{3+} is done randomly, that is, any of 16 existing Y^{3+} in the unit cell can be replaced. The ionic relaxation of the doped structures shown in Table 3 shows that substitution occurs primarily at the site of Y_1, which agrees with the result obtained by Wen et al. (2014). This means that even if Eu^{3+} is substituted into a Y_2 site, optimization of the cell rearranges the relaxed cell so that Eu^{3+} ends up at the Y_1 site. This could be due to the larger polyhedron volume surrounding the Y_1 site compared to the Y_2 site. The Y_1 site also corresponds to the site where a higher emission can be observed as the concentration of Eu^{3+} increases (Ghosh et al., 2006). It should be noted that the concentration is defined by the number of the existing Eu^{3+} ions in a standard unit cell with 16 Y^{3+} ions. As a result, substituting one, two, three, and four Eu^{3+} ions corresponds to 6.25%, 12.5%, 18.75%, and 25% concentration values, respectively.

Since the impurity ions occupy the Y_1 site, it can be inferred that the main luminescent activity is associated with the Y_1 site. Table 3 compares the average bond lengths at different concentrations. The table shows that an increase in concentration is associated with a gentle decrease in average bond length at the Y_1 site.

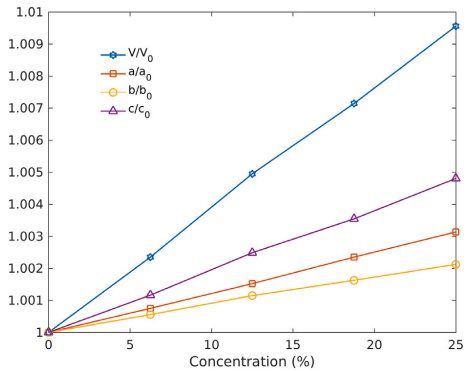

Fig. 3. Relative volume, V/V_0, and lattice parameters, a/a_0, b/b_0 and c/c_0, with doping concentration.

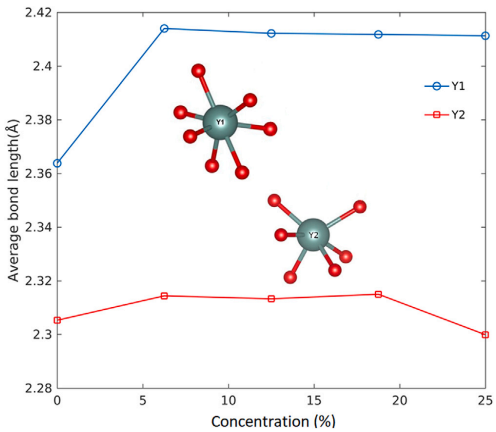

Fig. 4. Bond length variation for doping sites Y_1 and Y_2 as functions of doping concentration..

Fig. 4 shows the average bond lengths surrounding the possible doping positions Y_1 and Y_2 for different doping concentrations. For the Y_1 case, there is initially a considerable increase in the average bond length compared to the pure crystal bond length. As the doping concentration further increases, a slight decrease in the average bond length is observed. At the site of Y_2, after a slight jump to the first data point, the curve reaches a plateau and then descends for the 25% concentration. This decrease could be caused by both the larger atomic radius of Eu compared to Y, and by the higher electronegativity of Eu

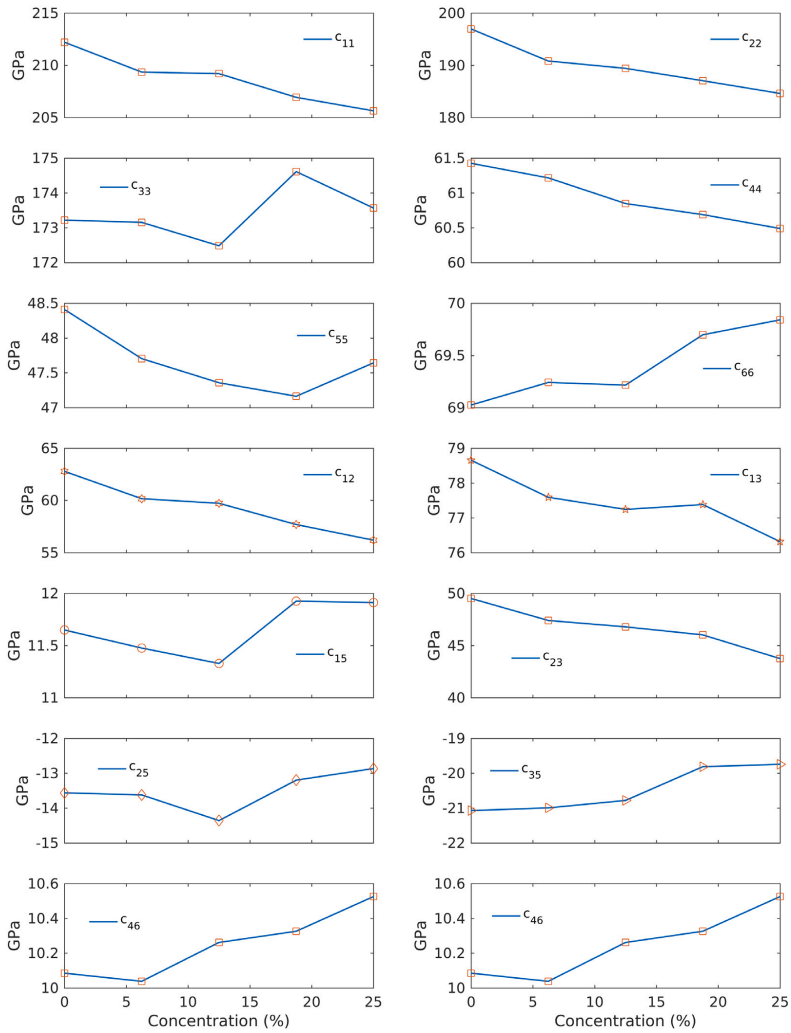

Fig. 5. Components of elastic stiffness matrix for different doping concentrations.

compared to Y which now, due to the higher concentration of Eu, can act more efficiently.

According to Wang et al. (2017), as the bond length of the luminescent center ligand becomes shorter, the emission spectrum shifts towards longer wavelengths, and crystal field splitting becomes stronger due to the change in the local crystal field environment. Thus, considering Fig. 4, the rise in doping concentration should shift the wavelength of the Y_1 site towards red, with the exception of first section of the Y_1 curve where the sudden jump should be interpreted as a shorter wavelength. In other words, a doped YSO always emits shorter wavelengths for the doping site Y_1 compared to the host crystal. Fig. 4 also suggests that at doping site Y_2, doping increases the average bond length and consequently shortens the wavelength. The value of the average bond length between 6.25% and 18.75% remains almost constant, with a small drop at 12.5%. When the doping concentration exceeds 18.75%, the bond length drops dramatically and is less than that of the host crystal. This drop can be related to the higher electronegativity of the Eu^{3+} ion. The reason this phenomenon only occurs at site Y_2 is probably due to the lower number of ligands at this site.

4.2. Elastic properties

The elastic constants were calculated using both the stress–strain and the strain–energy relationships. First, a few diagonal elements of the stiffness matrix C_{ij}, in Eq. (1) were calculated using Eqs. A_1, A_2, A_3 & A_4 given in Appendix. These values were compared to the results calculated using the stress–strain curve. Since the discrepancies

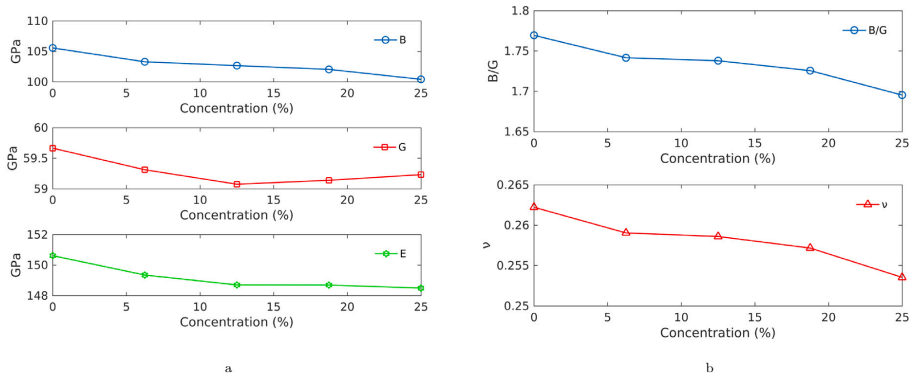

Fig. 6. Elastic moduli and Pugh ratio of the YSO crystal as a function of Eu^{3+} doping concentrations.

Table 4
Elastic constants (GPa). *: *This study*.

Material	Functional	c_{11}	c_{22}	c_{33}	c_{44}	c_{55}	c_{66}	c_{12}	c_{13}	c_{15}	c_{23}	c_{25}	c_{35}	c_{46}
$Y_2SiO_5^*$	PBE	212.21	197	173.21	61.42	48.41	69.25	62.78	78.65	11.64	49.50	−13.56	−21.07	10.08
Y_2SiO_5 Luo et al. (2014)	PBE	226	201	156	44	67	63	88	59	5	27	−0.3	−0.2	10

were small, all other elements of C_{ij} were calculated using the stress–strain relation method, which is an automated scheme within the VASP code and requires less computation time than using the strain–energy relation. Table 4 shows the resulting elastic constants with the values from this study marked with *. The theoretical results of Luo et al. (2014) are also included in Table 4.

The stability of the results was checked using Eq. (2) in Section 3.1. The stability criteria were met for all concentrations, implying that the $B2/b$ structure remains mechanically stable up to at least 25%. Plots of elastic constants as a function of doping concentration are depicted in Fig. 5.

In Eq. (1), c_{11}, c_{22}, and c_{33} represent the stiffness vs. principal strains while c_{44}, c_{55}, and c_{66} correspond to resistance to shear deformations. Overall, the largest changes occur in the diagonal components, whereas the off-diagonal terms show small changes. To clarify, the largest change occurs at c_{22}, where the value drops from 197 GPa to 184 GPa. The smallest change takes place at c_{46}, where the value increases from 10.09 GPa to 10.53 GPa.

The elastic moduli were calculated using the expressions in Section 3.1. A summary of all elastic moduli for the pure crystal is presented in Table 5, together with previous results for comparison and validation. The variations in B, G, E, and ν with doping concentration are presented in Fig. 6. All elastic moduli show a decreasing trend with increasing doping concentration, where the relative decrease is less in B and E compared to G and ν.

The Pugh ratio is included in Fig. 6 to further investigate the physical properties of the material. The Pugh ratio gauges the ductility of materials based on the simple ratio given as B/G. The higher the value of this ratio, the higher the ductility of the material, and vice versa. As Fig. 6 demonstrates, the ratio gradually decreases with increasing concentration. The overall drop of the Pugh ratio between pure and 25% doped crystal is 4.2%. Although this drop is small, it shows that there is a decreasing trend in the Pugh ratio which indicates the YSO becomes more brittle with higher impurity concentration.

4.3. Elastic anisotropy

The knowledge of the anisotropic properties of YSO might help to reduce the effects of induced birefrengence by identifying the elastic moduli in the chosen orientation in applications that are sensitive to thermo-mechanical noise. One such application is laser stabilization (Thorpe et al., 2011), for which YSO is considered a promising host crystal. However, due to its low symmetry and the misalignment of its crystallographic axes with Cartesian coordinate axes, the crystal suffers from high anisotropy.

Table 5
Calculated elastic moduli for the pure YSO. *: *This study*.

Type	B (GPa)	G(GPa)	E(GPa)	ν
$Y_2SiO_5^*$	105.56	59.66	150.61	0.262
Y_2SiO_5 Sun et al. (2008)	108	47	124	0.31
Y_2SiO_5 Luo et al. (2014)	100	60	150	0.25

Therefore we have determined the anisotropy of this crystal with respect to doping concentration. The anisotropy of the moduli are gauged using anisotropy indices defined by Chung and Buessem (1967) where, for polycrystalline materials, the bulk modulus anisotropy factor, A_B, and the shear anisotropy factor, A_G, are defined as

$$A_B = \frac{B_V - B_R}{B_V + B_R}, \tag{20}$$

$$A_G = \frac{G_V - G_R}{G_V + G_R} \tag{21}$$

where V and R refer to the Voigt and Reuss limiting bounds according to Eqs. (8)–(11). The anisotropy factors for both moduli are zero for elastic isotropy when $B_V = B_R$ and $G_V = G_R$, and +1 at the largest possible anisotropy, when the upper bounds of B_R and G_R both approach zero. Fig. 7 shows A_B and A_G as functions of doping concentration. Although the change is minuscule for both A_B and A_G, there is a downward trend in both A_B and A_G that indicates that higher concentrations will lead to lower anisotropy of the material.

Another tool that can assist in measuring the overall anisotropy of crystals is the universal anisotropy index A^U defined by Ranganathan and Ostoja-Starzewski (2008). This index is "universal" since it is applicable to all crystal symmetries and defined as

$$A^U = 5\,\frac{G_V}{G_R} + \frac{B_V}{B_R} - 6. \tag{22}$$

Table 6
Thermodynamic values predicted for pure YSO and Eu-doped YSO. *:*This study*.

Compound	ρ (g/cm^3)	v_l (m/s)	v_i (m/s)	v_m (m/s)	$\theta_D(K)$	κ_{min} (W/mK)	γ
$Y_2SiO_5^*$	4.3142	9583.8	3718.8	4139.4	514.35	0.9955	1.560
$Eu^{6.25\%} : Y_2SiO_5^*$	4.4228	9378.0	3662.0	4074.1	510.45	0.9962	1.544
$Eu^{12.5\%} : Y_2SiO_5^*$	4.5298	9240.2	3611.3	4017.4	507.37	0.9981	1.542
$Eu^{18.75\%} : Y_2SiO_5^*$	4.6381	9111.0	3570.8	3971.4	505.53	1.0023	1.535
$Eu^{25\%} : Y_2SiO_5^*$	4.7448	8951.8	3533.2	3927.3	503.71	1.0063	1.517
Y_2SiO_5 Sun et al. (2009)	–	–	–	–	580	1.13	–
Y_2SiO_5 Luo et al. (2014)	4.680	6196	3580	3975	507	1.01	1.50

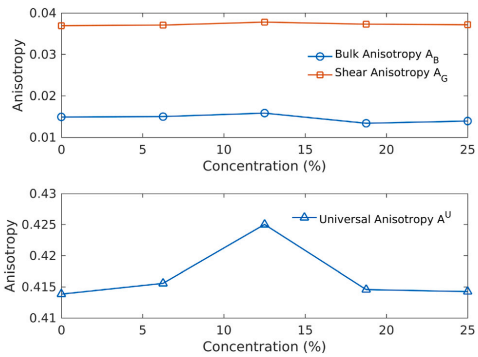

Fig. 7. Elastic anisotropy indices of YSO versus doping concentration.

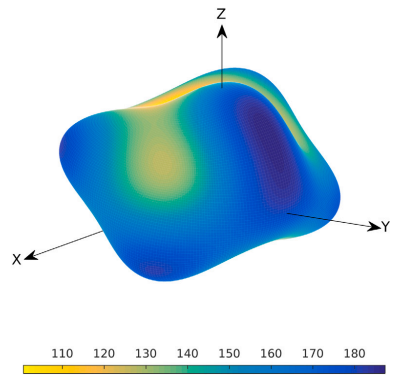

Fig. 8. 3D representation of Young's modulus (GPa) in Cartesian coordinates..

The value of anisotropy using the universal index A^U starts at zero, meaning isotropy, and increases towards $+\infty$ as the anisotropy increases. The universal anisotropy index is also included in Fig. 7. As can be seen, the minimum value of A^U is obtained for pure YSO ($A^U = 0.4138$), and the maximum is obtained for $Eu^{12.25\%} : YSO$. The largest difference in A^U is $\Delta A^U = 0.0112$. The overall trend also agrees with A_B and A_G. The same discrepancy at $Eu^{12.25\%} : YSO$, where there is jump in value of anisotropy, occurs in A^U. So in general, A^U reveals that increasing concentration of impurity increases the overall anisotropy of the crystal.

A convenient way to illustrate the elastic anisotropy is through a three-dimensional surface representation showing the variation of the Young's modulus with crystallographic direction. The direction-dependence of the YSO Young's modulus is determined as follows (Nye et al., 1985):

$$\frac{1}{E} = l_1^4 s_{11} + 2l_1^2 l_2^2 s_{12} + 2l_1^2 l_3^2 s_{13} + 2l_1^3 l_3^2 s_{15} + l_2^4 s_{22} + 2l_2^2 l_3^2 s_{23} + 2l_1 l_2^2 l_3 s_{25} + l_3^4 s_{33} + 2l_1 l_3^3 s_{35} + l_2^2 l_3^2 s_{44} + 2l_1 l_2^2 l_3 s_{46} + l_1^2 l_3^2 s_{55} + l_1^2 l_2^2 s_{66} \quad (23)$$

where l_1, l_2, and l_3 are the direction cosines in relation to the Cartesian (x, y, z) system. Figs. 8–9(c) show the directional dependence of the Young's modulus of pure YSO in Cartesian coordinates (x, y, z), where the z-axis coincides with the crystallographic direction b. As the shape of the 3D representation of Young's modulus for an isotropic material would be a perfect sphere, the degree of deviation from a sphere indicates the degree of anisotropy in the system.

Figs. 9(a)–9(c) show 2D projections of the surface. In the 2D image, the deviation from a circular shape is an indicator of anisotropy. As Fig. 9(c) shows, the yz plane exhibits the highest level of deviation. The anisotropy can be explained by the low symmetry of the crystal, as well as misalignment between the crystallographic axes and the Cartesian coordinates. Nevertheless, the figures show that YSO is highly anisotropic and, consequently, the resulting Young's modulus depends strongly on orientation. The directional dependence of Young's modulus in corresponding orientations as a function of concentration is calculated and plotted in Fig. 10. The values along the Cartesian axes and their variations with doping concentration are denoted as E_i, $i = x, y, z$. As the figure shows, while both E_x and E_z almost remain the same, E_y decreases slightly with an increase in concentration.

4.4. Thermodynamic properties

Table 6 shows the Debye temperatures and velocities for each concentration based on Eqs. (12)–(15). There is a slight decrease in the Debye temperature as the concentration of dopants increases in the host material. All other properties listed in the table follow the same trend, which also follows the same descending trend as the elastic moduli shown in Fig. 6.

The Debye temperature is a suitable parameter to compare the micro-hardness of materials because it increases with the hardness of the material. There is also a correlation between the Debye temperature and bond strength; the higher the Debye temperature, the stronger the bond. The table shows that the increase in doping concentration reduces the bond strength, which may be caused by an increase in interatomic bonding. This may stem from the larger atomic radius of Eu^{3+} in comparison with Y^{3+}.

The minimum thermal conductivities, κ_{min}, and the Grüneisen parameters, γ, were calculated for different concentrations and inserted in Table 6 to further investigate the thermodynamic effects stemming from impurities. The thermal conductivity of a material describes the diffusivity of heat flow on the temperature gradient through phonon transport. In this context, it can be interpreted as an index to measure how well a material conducts heat. Thus, a higher value of κ_{min} can be directly interpreted as a higher conductivity, and vice versa. In Table 6, YSO with $\kappa_{min} = 0.995$ is categorized as having very low thermal conductivity.

The calculated values of γ with respect to different concentrations are listed in Table 6, which suggests a gradual decrease in γ

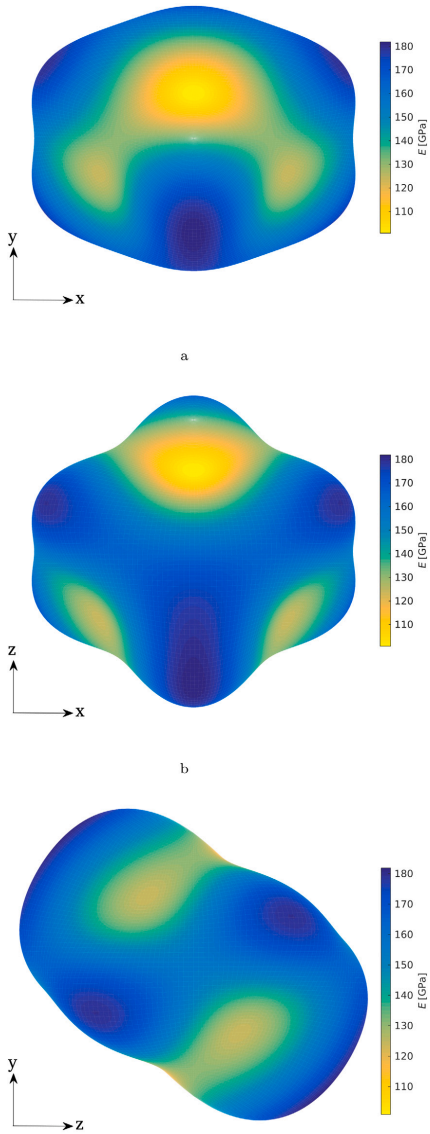

Fig. 9. 2D projections of the Young's modulus (GPa) surface in the xy (a), the xz (b), and the yz (c) planes.

with increasing Eu^{3+} concentration. This means a higher degree of impurity would cause less anharmonic phonon scattering in the YSO crystal (Ashcroft et al., 1976). As anharmonic scattering of phonons is the reason for finite thermal expansion, a lower degree of anharmonic scattering should decrease thermal expansion (Ashcroft et al., 1976).

The predicted heat capacities in a constant volume based on the Debye model as described in Eq. (18) are presented in Fig. 11. The

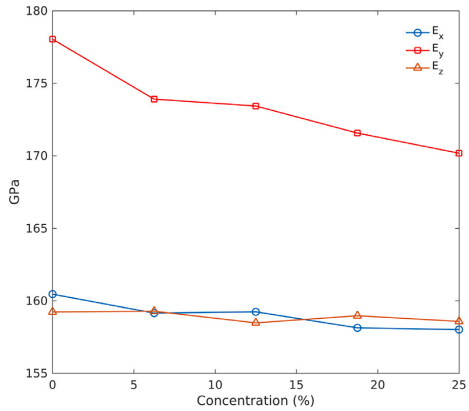

Fig. 10. The components of the Young's modulus E_i, i = x, y, z.

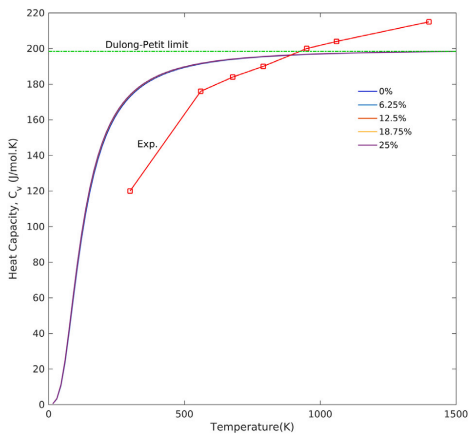

Fig. 11. Heat capacity, C_v, based on Debye model for various Eu^{3+} concentrations. The red line with squares indicates experimental data for the molar heat capacity, C_p, of pure YSO obtained by Sun et al. (2009). (For interpretation of the references to colour in this figure legend, the reader is referred to the web version of this article.)

figure shows that the change in heat capacity due to concentration is negligible. This interpretation is based on the fact that all C_v curves coincide, and no deviation between different concentrations is visible. In addition, the predicted curves approach the Dulong–Petit limit at high temperatures (T >> θ_D). According to this law, the heat capacity at constant volume, C_v, for each atom approaches 3R for temperature values above the Debye temperature (calculated θ_D for YSO is 514.35 K). Here R is the gas constant (Kittel et al., 1976), whereas for temperatures below θ_D, quantum effects gain importance and C_v approaches zero.

To evaluate the predicted heat capacity, the experimental values of heat capacity, C_p, obtained by Sun et al. (2009) are superimposed on the predicted curve. As can be seen, except at the two extremes (300 K and 1400 K), the predicted model agrees with the experimental

data points. If corrections to C_p and C_v were taken into consideration, the predicted curve would be in better agreement with experiment on the left-hand side. The correction values range between 1 and 8 K at room temperature and reach a maximum at melting point, where the correction value would be equal to 10% of C_v (Sun et al., 2009).

5. Conclusions

In this study the DFT plane-waves method is used to investigate the effect of doping on the mechanical and thermodynamic properties of the YSO crystal, which is a popular host for photonic and laser stabilization applications. The results show that the impurity ions prefer to occupy the Y_1 site over the Y_2 site of X2-Y_{2SiO_5}. The resulting emission spectrum of this site would initially be shifted towards shorter wavelengths, and then towards longer wavelengths as the doping concentration gradually increases. The overall trend of the mechanical properties decreases due to doping. Thus the bulk, Young's, and shear moduli of the host drop with increasing doping concentration. The crystal becomes more brittle as a consequence of the decrease in the Pugh ratio. The overall anisotropy of the crystal increases with increasing concentration.

Lastly, the thermodynamic parameters reveal that increasing doping concentration weakens the bond strength, and reduces the anharmonic effects in the crystal, which may in turn decrease the thermal expansion.

Declaration of competing interest

The authors declare that they have no known competing financial interests or personal relationships that could have appeared to influence the work reported in this paper.

Acknowledgments

This work is supported by the Knut and Alice Wallenberg Foundation, Sweden through grant no.: KAW-2016.0081. The simulations were performed using computational resources provided by the Swedish National Infrastructure for Computing (SNIC) at LUNARC, Lund University, and at the National Supercomputer Centre (NSC), Linköping University.

Appendix

The matrix A for monoclinic systems is described by Söderlind (2002). The applied strain is denoted by δ.

$$A_1 = \begin{pmatrix} 1+\delta & 0 & 0 \\ 0 & 1 & 0 \\ 0 & 0 & 1 \end{pmatrix}$$

$$A_2 = \begin{pmatrix} 1 & 0 & 0 \\ 0 & \delta+1 & 0 \\ 0 & 0 & 1 \end{pmatrix}$$

$$A_3 = \begin{pmatrix} 1 & 0 & 0 \\ 0 & 1 & 0 \\ 0 & 0 & 1+\delta \end{pmatrix}$$

$$A_4 = \frac{1}{1-\delta^2}\begin{pmatrix} 1 & 0 & 0 \\ 0 & 1 & \delta \\ 0 & \delta & 1 \end{pmatrix}$$

$$A_5 = \frac{1}{1-\delta^2}\begin{pmatrix} 1 & 0 & \delta \\ 0 & 1 & 0 \\ \delta & 0 & 1 \end{pmatrix}$$

$$A_6 = \frac{1}{1-\delta^2}\begin{pmatrix} 1 & \delta & 0 \\ \delta & 1 & 0 \\ 0 & 0 & 1 \end{pmatrix}$$

$$A_7 = \frac{1}{1-\delta^2}\begin{pmatrix} 1+\delta & 0 & 0 \\ 0 & 1-\delta & 0 \\ 0 & 0 & 1 \end{pmatrix}$$

$$A_8 = \frac{1}{1-\delta^2}\begin{pmatrix} 1+\delta & 0 & 0 \\ 0 & 1 & 0 \\ 0 & 0 & 1-\delta \end{pmatrix}$$

$$A_9 = \frac{1}{1-\delta^2}\begin{pmatrix} 1 & 0 & 0 \\ 0 & 1+\delta & 0 \\ 0 & 0 & 1-\delta \end{pmatrix}$$

$$A_{10} = \frac{1}{1-\delta^2}\begin{pmatrix} 1+\delta & 0 & \delta \\ 0 & 1-\delta & 0 \\ 0 & 0 & 1 \end{pmatrix}$$

$$A_{11} = \frac{1}{1-\delta^2}\begin{pmatrix} 1+\delta & 0 & \delta \\ 0 & 1 & 0 \\ 0 & 0 & 1-\delta \end{pmatrix}$$

$$A_{12} = \begin{pmatrix} 1 & \delta & 0 \\ 0 & 1 & \delta \\ 0 & 0 & 1 \end{pmatrix}$$

$$A_{13} = \frac{1}{1+\delta}\begin{pmatrix} 1+\delta & 0 & \delta \\ 0 & 1 & 0 \\ 0 & 0 & 1 \end{pmatrix}$$

References

Anderson, O.L., 1963. A simplified method for calculating the Debye temperature from elastic constants. J. Phys. Chem. Solids 24 (7), 909–917.
Ashcroft, N., Mermin, N., et al., 1976. Solid State Physics. In: HRW International Editions, Holt, Rinehart and Winston.
Belomestnykh, V.N., Tesleva, E.P., 2004. Interrelation between anharmonicity and lateral strain in Quasi-isotropic polycrystalline solids. Tech. Phys. 49 (8).
Blöchl, P.E., 1994. Projector augmented-wave method. Phys. Rev. B 50 (24), 17953.
Ching, W., Ouyang, L., Xu, Y.-N., 2003. Electronic and optical properties of Y_2SiO_5 and $Y_2Si_2O_7$ with comparisons to α-SiO_2 and Y_2O_3. Phys. Rev. B 67 (24), 245108.
Chung, D., Buessem, W., 1967. The elastic anisotropy of crystals. J. Appl. Phys. 38 (5), 2010–2012.
Clarke, D.R., 2003. Materials selection guidelines for low thermal conductivity thermal barrier coatings. Surface Coat. Technol. 163, 67–74.
Ghosh, P., Sadhu, S., Patra, A., 2006. Preparation and photoluminescence properties of Y_2SiO_5: Eu^{3+} nanocrystals. Phys. Chem. Chem. Phys. 8 (28), 3342–3348.
Hill, R., 1952. The elastic behaviour of a crystalline aggregate. Proc. Phys. Soc. Sect. A 65 (5), 349.
Kittel, C., et al., 1976. Introduction to Solid State Physics, Vol. 8. Wiley New York.
Kresse, G., Furthmüller, J., 1996. Efficiency of ab-initio total energy calculations for metals and semiconductors using a plane-wave basis set. Comput. Mater. Sci. 6 (1), 15–50.
Luo, Y., Wang, J., Wang, J., Li, J., Hu, Z., 2014. Theoretical predictions on elastic stiffness and intrinsic thermal conductivities of yttrium silicates. J. Am. Ceram. Soc. 97 (3), 945–951.
Mock, A., Korlacki, R., Knight, S., Schubert, M., 2018. Anisotropy and phonon modes from analysis of the dielectric function tensor and the inverse dielectric function tensor of monoclinic yttrium orthosilicate. Phys. Rev. B 97 (16), 165203.
Nye, J.F., et al., 1985. Physical Properties of Crystals: Their Representation by Tensors and Matrices. Oxford University Press.
O'Bryan, H.M., Gallagher, P.K., Berkstresser, G., 1988. Thermal expansion of Y_2SiO_5 single crystals. J. Am. Ceram. Soc. 71 (1), C–42.
Perdew, J.P., Burke, K., Ernzerhof, M., 1996. Generalized gradient approximation made simple. Phys. Rev. Lett. 77 (18), 3865.
Ranganathan, S.I., Ostoja-Starzewski, M., 2008. Universal elastic anisotropy index. Phys. Rev. Lett. 101 (5), 055504.
Ravindran, P., Fast, L., Korzhavyi, P.A., Johansson, B., Wills, J., Eriksson, O., 1998. Density functional theory for calculation of elastic properties of orthorhombic crystals: Application to $TiSi_2$. J. Appl. Phys. 84 (9), 4891–4904.
Reuß, A., 1929. Berechnung der fließgrenze von mischkristallen auf grund der plastizitätsbedingung für einkristalle. ZAMM-J. Appl. Math. Mech./Z. Angew. Math. Mech. 9 (1), 49–58.
Ricci, P., Carbonaro, C., Corpino, R., Cannas, C., Salis, M., 2011. Optical and structural characterization of terbium-doped Y_2SiO_5 phosphor particles. J. Phys. Chem. C 115 (33), 16630–16636.
Saha, S., Chowdhury, P.S., Patra, A., 2005. Luminescence of Ce^{3+} in Y_2SiO_5 nanocrystals: Role of crystal structure and crystal size. J. Phys. Chem. B 109 (7), 2699–2702.
Söderlind, P., 2002. First-principles elastic and structural properties of uranium metal. Phys. Rev. B 66 (8), 085113.

SpringerMaterials, 2016. In: Villars, P., Cenzual, K. (Eds.), X2-Y_2SiO_5 Crystal Structure: Datasheet from "Pauling file Multinaries Edition—2012". (sd_1210584), Springer, Berlin.

Sun, Z., Li, M., Zhou, Y., 2009. Thermal properties of single-phase Y_2SiO_5. J. Eur. Ceram. Soc. 29 (4), 551–557.

Sun, Z., Wang, J., Li, M., Zhou, Y., 2008. Mechanical properties and damage tolerance of Y_2SiO_5. J. Eur. Ceram. Soc. 28 (15), 2895–2901.

Thorpe, M.J., Rippe, L., Fortier, T.M., Kirchner, M.S., Rosenband, T., 2011. Frequency stabilization to 6 × 10-16 via spectral-hole burning. Nat. Photonics 5 (11), 688.

Voigt, W., et al., 1928. Lehrbuch der kristallphysik, Vol. 962. Teubner Leipzig.

Wang, C., Wang, Z., Li, P., Cheng, J., Li, Z., Tian, M., Sun, Y., Yang, Z., 2017. Relationships between luminescence properties and polyhedron distortion in $Ca_{9-x-y-z}Mg_xSr_yBa_z$ $Ce(PO_4)_7$: Eu^{2+}, Mn^{2+}. J. Mater. Chem. C 5 (41), 10839–10846.

Wen, J., Duan, C.-K., Ning, L., Huang, Y., Zhan, S., Zhang, J., Yin, M., 2014. Spectroscopic distinctions between two types of Ce^{3+} ions in X2-Y_2SiO_5: A theoretical investigation. J. Phys. Chem. A 118 (27), 4988–4994.

Yoder, P.R., 2008. Mounting Optics in Optical Instruments, Vol. 181. Spie Press.

Paper II

Amin Mirzai, Aylin Ahadi

A theoretical investigation of optical path length variation of Eu: Y_2SiO_5

Submitted to Optics Express, September 2023

A theoretical investigation of optical path length variation of Eu:Y_2SiO_5

Amin Mirzai,[1,*] and Aylin Ahadi,[1]

[1]*Lund university, Department of Mechanical Engineering Sciences, Division of Mechanics, Materials, and Component Design, P.O. Box 118, SE-221 00 Lund, Sweden*
[*]*amin.mirzai@lth.lu.se*

Abstract: The laser host materials undergo relatively small changes in their intrinsic properties due to various sources during an experiment. These sources are often related to temperature change or applied stress, which may cause stress-induced birefringence. Consequently, the crystal experiences an optical anisotropy, which may affect the final outcome of the experiments. One way to reduce probable noises is to predict the change in optical properties with respect to load. To predict the changing pattern of the refractive index in a crystal, one needs to know both the elastic and photoelastic constants of the material. In this study, We utilized density functional perturbation theory (DFPT) to extract the photoelastic tensor of Y_2SiO_5 and Eu-doped Y_2SiO_5 crystals. Using the photoelastic and elastic constants calculated, a Finite Element (FE) model was developed, which allowed us to apply load and then post-process the results. This methodology enabled us to observe the variation in refractive index (n), and consequently, the shift in the resonance frequency of the cavity. The results obtained were in agreement with experimental measurements, falling within a 2% discrepancy across a temperature range spanning from cryogenic to room temperature. This correlation suggests the feasibility of using the current workflow as a predictive tool for evaluating variations in refractive indices over a specific interval.

1. Introduction

An optical cavity, like a laser resonator, has certain frequencies at which it resonantly enhances the electromagnetic field. These resonant frequencies are determined by the condition that the optical path length of the cavity (the distance that light travels inside the cavity) be an integer multiple of the wavelength of the light. This is necessary for the light wave to constructively interfere with itself after each round trip in the cavity, and it's what allows a laser, for example, to generate a strong, coherent beam of light. Mathematically, the condition for resonance is given by [1]:

$$m\lambda = 2nL \tag{1}$$

, where m the mode number (number of round trips in the cavity) is an integer, λ is the wavelength, L is the physical length of the cavity and n is the refractive index. Now, if the optical path length changes - either because the physical length of the cavity changes, or because the refractive index of the medium changes (due to a change in temperature) - then the other side of the equation above changes. To maintain equality, the wavelength of the light must also change. But the frequency (f) and wavelength of light are related by the speed of light (c):

$$c = f\lambda \tag{2}$$

So if the wavelength changes while the speed of light remains constant, the frequency must also change. Hence, a change in the optical path length of a cavity results in a shift in the resonant frequencies of the cavity.

In practical terms, this concept implies that by exercising meticulous control over the length of an optical cavity, for instance, by delicately adjusting the position of one of the mirrors in a laser system, we gain the ability to fine-tune the frequency at which the cavity resonates.

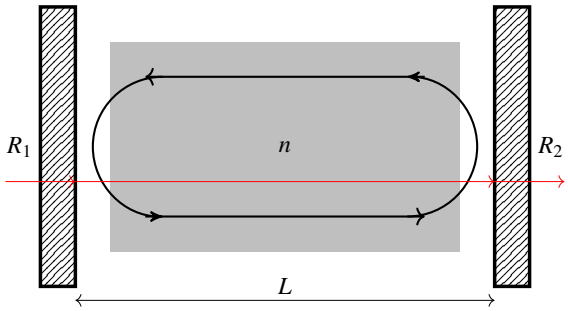

Fig. 1. The schematic view of an optical cavity. The light path in the cavity is indicated by circulating arrows whereas the red arrows indicate entering and exiting light path.

A crucial outcome of this mechanism is the potential to optimize the signal-to-noise ratio. This essentially entails boosting the desired information, or the signal, in the output, while simultaneously minimizing any undesired interference or noise, thereby enhancing the overall quality and accuracy of the laser's performance.

For instance, the resonance frequency of a cavity is used to stabilize a laser's frequency [2]. This is achieved by aligning the laser's frequency to the resonance frequency of the cavity, which means transferring the stability of the cavity to the laser [3]. Hence, the reference cavity acts as an optical resonator that serves as a frequency reference in optical frequency standards [4]. In turn, an ultra-high frequency stability laser is an essential part of an optical atomic clocks [5], and a myriad of optical precision measurements [6, 7].

Given the importance of understanding the factors influencing the physical length of a cavity or the refractive index of a medium, it is essential to examine the phenomena that contribute to these variations. In this work, however, the analysis will primarily concentrate on changes in the refractive index as a result of an external load. The photoelastic effect, which describes changes in the optical properties of a material under mechanical deformation, is employed to examine this alteration. Nevertheless, the applicability of the photoelastic effect is dependent on the availability of the elasto-optic tensor elements. These elements are instrumental in discerning the optical path difference across the crystal.

Furthermore, since the photoelastic properties of a material can be significantly influenced by its electronic structure, and the fact that impurities within a crystal lattice can modify the distribution of stress across the material that can subsequently lead to shifts in the material's photoelastic behavior. We investigate two cases: a pure case and a doped case.

We start by determining the photoelastic constants for both pure Y_2SiO_5 (YSO) and Eu-doped YSO, utilizing the Density Functional Perturbation Theory (DFPT) [8]. Subsequently, leveraging the elastic constants calculated in our previous study [9], we have developed a Finite Element (FE) model. This model allows us to examine the impact of mechanical loads, specifically temperature and stress, on the refractive index of both pure and Eu-doped YSO, which in turn allows us to observe the shift in resonance frequency of the cavity.

1.1. Y_2SiO_5

Yttrium Orthosilicate (YSO), is a dielectric material with biaxial anisotropy, and its refractive index at various frequencies is well-documented [10]. It is a monoclinic biaxial crystal that belongs to the C2/c (C_6^{2h}) space group [11], where RE ions can substitute for the Y^{3+} ions. It is a well-known host material for RE ions, and it's used extensively in optical research. Since the crystal is monoclinic, there are 4 different dielectric functions $\epsilon(\omega)$ that are required to describe the material's interaction with light in the wavelength region where the material is

transparent [12, 13]. The principle values of the dielectric functions are unequal and they are ordered as $\epsilon_{11} < \epsilon_{22} < \epsilon_{33}$ [12]. The off-diagonal, ϵ_{12}, is a small value but it is non-zero.

$$\epsilon = \begin{bmatrix} \epsilon_{11} & \epsilon_{12} & 0 \\ \epsilon_{12} & \epsilon_{22} & 0 \\ 0 & 0 & \epsilon_{33} \end{bmatrix} = \begin{bmatrix} 3.0897 & 0.0135 & 0 \\ 0.0135 & 3.1051 & 0 \\ 0 & 0 & 3.1645 \end{bmatrix} \tag{3}$$

The YSO crystal structure is characterized by three distinct, unequal crystallographic axes, labeled as a, b, and c. These axes have respective lengths of 14.51 Å, 6.81 Å, and 10.51 Å. Notably, axis b is perpendicular to both a and c, while the angle between axes a and c is denoted by β [14]. Apart from the primary crystallographic axes, YSO is further defined by its optical axes: D_1, D_2, and b [14, 15]. The relationship between these optical axes and the crystallographic axes is captured in Figure 2 [14].

In experiments involving YSO crystal, the optical beam is typically directed to propagate along the crystallographic b-axis of the crystal and polarized along the D_1 axis since this setup provides the largest absorption [16]. Moreover, the b-axis aligns with the optic axis of the crystal, thereby making it an axis of symmetry. This property can contribute to more predictable and desirable outcomes in optical experiments.

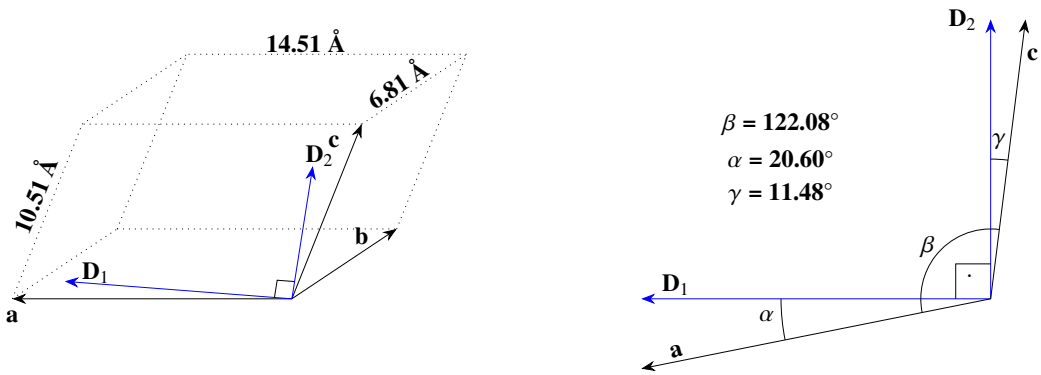

Fig. 2. The angles and the relation between optical indicatrix axes and crystallographic axes.

2. Theory & method

2.1. Theoretical background

The elasto-optic effect illustrates the change in the optical properties of a material under the influence of stress. The indices of refraction due to the birefringence of an unstressed material can be described by Maxwell's equations, but it will lead to impractical long equations. To simplify, an ellipsoid as an analogy is used to express the variation of refractive indices. This ellipsoid is known as indicatrix [17], and it is identified by the following relation:

$$\frac{x_1^2}{n_1^2} + \frac{x_2^2}{n_2^2} + \frac{x_3^2}{n_3^2} = 1 \tag{4}$$

where x_1, x_2, x_3 are the the principal axes, and n_1, n_2, and n_3 are their corresponding refractive indices. The coefficients of this ellipsoid are the components of the relative dielectric impermeability tensor, B_{ij}, at optical frequencies, so the general form of indicatrix can be written

as:

$$B_{ij}x_i x_j = 1 \tag{5}$$

This way the small change of refractive index produced by stress can be traced by a change in the shape, size, and orientation of the indicatrix [11], and the changes in the coefficients of indicatrix, ΔB_{ij}, under applied stress, σ_{kl} or strain e_{kl}, is given as:

$$\Delta B_{ij} = p_{ijkl}e_{kl} = \pi_{ijkl}\sigma_{kl} \tag{6}$$

where p_{ijkl}, and π_{ijkl} are fourth-rank elasto-optic and piezo-optic tensors. The left-hand side of the above equation can be rewritten as: ΔB_{ij} = B_1 - B_0, where B_0 and B_1 are the dielectric impermeability tensor before and after the applied stress [11]. Moreover, as the principal components of B tensor are simply the inverse of the dielectric tensor [11] and the relation between refractive index and dielectric tensor is $\epsilon = n^2$, Equation 6 can be rewritten as,

$$\Delta B_{ii} = [\epsilon^{-1}(\sigma_{kl})]_{ii} - [\epsilon^{-1}(0)]_{ii} = \frac{1}{n_1^2} - \frac{1}{n_0^2} \tag{7}$$

This means the knowledge of applied stress along with piezo-optic coefficients would show us how much the refractive index would change with respect to applied stress.

The B is actually a 3x3 matrix in which it can be reduced with respect to the symmetry of the crystal, and take the form that is similar to the dielectric tensor in Equation 3.

$$B = \begin{bmatrix} B_{11} & B_{12} & 0 \\ B_{21} & B_{22} & 0 \\ 0 & 0 & B_{33} \end{bmatrix} \tag{8}$$

In the same way, the π_{ijkl} which is normally a 6x6 matrix can be reduced to its corresponding monoclinic form [18], which allows us to rewrite the Equation 6 as:

$$\Delta B = \begin{pmatrix} \pi_{11} & \pi_{12} & \pi_{13} & 0 & \pi_{15} & 0 \\ \pi_{21} & \pi_{22} & \pi_{23} & 0 & \pi_{25} & 0 \\ \pi_{31} & \pi_{32} & \pi_{33} & 0 & \pi_{35} & 0 \\ 0 & 0 & 0 & \pi_{44} & 0 & \pi_{46} \\ \pi_{51} & \pi_{52} & \pi_{53} & 0 & \pi_{55} & 0 \\ 0 & 0 & 0 & \pi_{64} & 0 & \pi_{66} \end{pmatrix} \begin{pmatrix} \sigma_1 \\ \sigma_2 \\ \sigma_3 \\ 2\sigma_4 \\ 2\sigma_5 \\ 2\sigma_6 \end{pmatrix} \tag{9}$$

The resultant matrix multiplication becomes:

$$\begin{pmatrix} \Delta B_1 \\ \Delta B_2 \\ \Delta B_3 \\ \Delta B_4 \\ \Delta B_5 \\ \Delta B_6 \end{pmatrix} = \begin{pmatrix} \pi_{11}\sigma_1 + \pi_{12}\sigma_2 + \pi_{13}\sigma_3 + 2\pi_{15}\sigma_5 \\ \pi_{21}\sigma_{11} + \pi_{22}\sigma_{12} + \pi_{23}\sigma_3 + 2\pi_{25}\sigma_5 \\ \pi_{31}\sigma_3 + \pi_{32}\sigma_2 + \pi_{33}\sigma_3 + 2\pi_{35}\sigma_5 \\ 2\pi_{44}\sigma_4 + 2\pi_{46}\sigma_6 \\ \pi_{51}\sigma_1 + \pi_{52}\sigma_2 + \pi_{53}\sigma_3 + 2\pi_{55}\sigma_5 \\ 2\pi_{64}\sigma_4 + 2\pi_{66}\sigma_6 \end{pmatrix} \tag{10}$$

The ΔB matrix on the left-hand side of the above equation can be rewritten to its original matrix form using index change notation as 23 and 32 $\rightarrow$ 4, 31 and 13 $\rightarrow$ 5, 12 and 21 $\rightarrow$ 6 [11]. Finally, the monoclinic symmetry of the ΔB matrix was considered to attain its final form.

$$\begin{pmatrix} \Delta B_1 \\ \Delta B_2 \\ \Delta B_3 \\ \Delta B_4 \\ \Delta B_5 \\ \Delta B_6 \end{pmatrix} \rightarrow \begin{pmatrix} \Delta B_1 & \Delta B_6 & \Delta B_5 \\ \Delta B_6 & \Delta B_2 & \Delta B_4 \\ \Delta B_5 & \Delta B_4 & \Delta B_3 \end{pmatrix} \xrightarrow{sym.} \begin{pmatrix} \Delta B_1 & \Delta B_6 & 0 \\ \Delta B_6 & \Delta B_2 & 0 \\ 0 & 0 & \Delta B_3 \end{pmatrix}$$

we can now obtain the resultant B_1 matrix, which contains the refractive index after applied pressure.

$$[\epsilon^{-1}(\sigma_{kl})]_{ij} = \begin{pmatrix} \epsilon^{-1}(0)_{11} & \epsilon^{-1}(0)_{12} & 0 \\ \epsilon^{-1}(0)_{12} & \epsilon^{-1}(0)_{22} & 0 \\ 0 & 0 & \epsilon^{-1}(0)_{33} \end{pmatrix} + \begin{pmatrix} \Delta B_1 & \Delta B_6 & 0 \\ \Delta B_6 & \Delta B_2 & 0 \\ 0 & 0 & \Delta B_3 \end{pmatrix} \quad (11)$$

$$\begin{pmatrix} \epsilon^{-1}(\sigma_{kl})_{11} & B_6 & 0 \\ B_6 & \epsilon^{-1}(\sigma_{kl})_{22} & 0 \\ 0 & 0 & \epsilon^{-1}(\sigma_{kl})_{33} \end{pmatrix} = \begin{pmatrix} \Delta B_1 + \epsilon^{-1}(0)_{11} & \Delta B_6 + \epsilon^{-1}(0)_{12} & 0 \\ . & \Delta B_2 + \epsilon^{-1}(0)_{22} & 0 \\ . & . & \Delta B_3 + \epsilon^{-1}(0)_{33} \end{pmatrix} \quad (12)$$

And finally, we reach the elements that correspond to the principle axes of dielectric impermeability tensor,

$$\begin{aligned} B_1^x = \Delta B_1 + B_0^x = \pi_{11}\sigma_1 + \pi_{12}\sigma_2 + \\ \pi_{13}\sigma_3 + \pi_{15}2\sigma_5 + \epsilon^{-1}(0)_{11} \\ B_1^y = \Delta B_2 + B_0^y = \pi_{21}\sigma_1 + \pi_{22}2\sigma_6 + \\ \pi_{23}\sigma_3 + \pi_{25}2\sigma_5 + \epsilon^{-1}(0)_{22} \\ B_1^z = \Delta B_3 + B_0^z = \pi_{31}\sigma_3 + \pi_{32}\sigma_2 + \\ \pi_{33}\sigma_3 + \pi_{35}2\sigma_5 + \epsilon^{-1}(0)_{33} \end{aligned} \quad (13)$$

in which the corresponding refractive indices of the principle axes after the applied pressure is:

$$n_x(\sigma_{kl}) = \sqrt{(1/B_1^x)}$$

$$n_y(\sigma_{kl}) = \sqrt{(1/B_2^y)}$$

$$n_z(\sigma_{kl}) = \sqrt{(1/B_3^z)} \quad (14)$$

2.2. Computational method

The *ab-initio* calculations are carried out using the CRYSTAL [19], and VASP [20]. The CRYSTAL code uses linear combinations of Gaussian Type Functions (GTF) as basis sets to construct the fictitious wave functions. The exchange and correlation part of Hamiltonian were treated based on PBE0 [21] method, and PBE [22]. An effective core potential atom-centered GTF basis set of triple-ζ valence quality, augmented by a polarization function (TZVP), is adopted for each element in the system. The truncation criteria for electronic integrals are controlled by five thresholds, which are set to 8, 8, 8, 10, and 20. Last but not least, the sampling of the reciprocal space was conducted using a shrinking factor of 4, and the convergence criterion on total energy was set to 10^{-8} Hartree.

The VASP calculations were conducted with the following setup. The cut-off energy was set to, 520 eV, while the k-point set for the unit cell was selected to be 4×8×6. The convergence threshold was set to 1×10^{-8} eV, and the force criterion for geometry optimization was 0.00001 eV/Å.

The extraction of piezo-optic and elasto-optic elements is conducted by applying a sequence of deformation matrices to the relaxed standard unit cell of YSO. These deformation matrices can be found in the Appendix. Following each deformation, we calculate the dielectric constant of the deformed unit cell. Subsequently, by employing a manipulated version of Equation 6, the piezo-optic and elasto-optic elements are derived.

$$\pi_{ijkl} = \Delta B_{ij}\sigma_{kl}^{-1} \quad (15)$$

For the finite element analysis, a 3D model was created and four pressure loads and a thermal load were analyzed – uniaxial load in two different directions, biaxial load and hydrostatic pressure. This is achieved by utilizing the pre-calculated elastic constants from our previous study [9], as well as thermal coefficient constants courtesy of Sun et al [23] and Marion et al. [24]. The schematic view of the crystal setup in ABAQUS is shown in Figure 3, a rectangular crystal with dimensions length of 5 mm, height of 4 mm, and depth of 1 mm. Due to the symmetry

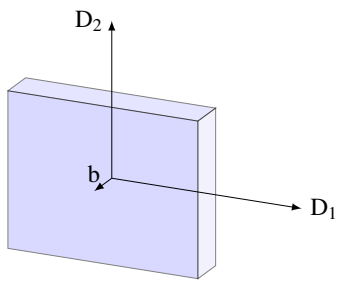

Fig. 3. Schematic view of the crystal geometry employed in FE model

of the crystal, only one-fourth of the geometry was modeled and symmetry conditions were

imposed into the two symmetry axes D_1 and D_2 assumed. The mesh is refined to 0.5 mm in order to describe a reliable stress profile. The element type used in the crystal is an 8-node thermally coupled linear brick element.

Following the application of temperature and stress to the model, we extract the resulting stress matrices for further post-processing. This entails multiplying by the piezo-optic tensor to obtain the affected impermeability matrix. The refractive index influenced by stress is then obtained by performing the manipulations that were detailed in the preceding section.

3. Result & Discussion

The data presented in Table 1 illustrates both the experimentally obtained and the computationally determined values for pure YSO. It also includes the refractive index values for YSO doped with Eu. Upon a preliminary comparison of the experimental and calculated values using the PBE functional, an overestimation was observed. In response to this discrepancy, the hybrid PBE0 approach was employed, resulting in improved congruity between experimental and theoretical results for pure YSO. Our results have the largest discrepancy with results provided by Weber [25]. So, we made a comparison with those results. The discrepancies for n_x, n_y, and n_z are 1.25%, 1.22%, and 1.77%, respectively, which shows the overall agreement between our experimental and theoretical findings suggests a reasonable level of accuracy and reliability.

When comparing the refractive indices of doped and undoped materials, a small but noticeable increase is observed across all principal axes. The largest divergence occurs in the D_1-direction, with a relative increase of 0.0114. In contrast, the smallest change is detected along the b-axis, with a discrepancy of only 0.0071. While it is difficult to draw definitive conclusions from a single data point, this trend suggests that impurities may increase the relative permittivity, leading to an increase in the refractive index. This is consistent with the previous findings [26, 27], who reported that RE-doping can increase the dielectric constant of the host material, although their study did not focus on YSO.

Table 1. Refractive indices for principle axes of pure YSO and Eu-doped YSO: *this work*:*. Note: the exp. values are obtained at 632.8 nm

source	$n_x \approx n_{D_1}$	$n_y \approx n_b$	$n_z \approx n_{D_2}$
YSO-Exp. [25]	1.780	1.784	1.811
Exp. [28]	1.769	1.770	1.789
YSO-PBE*	1.8569	1.8578	1.8822
YSO-PBE0-D3*	1.7577	1.7621	1.7789
Eu:YSO-PE0-D3*	1.7691	1.7692	1.7892

Table 2 demonstrates the elastic constants calculated in our previous work. This table is introduced with dual objectives. Firstly, these values contribute to establishing the Finite Element (FE) model in ABAQUS. Secondly, these values help evaluate the accuracy of the photoelastic constants, which represent changes in the optical properties of a material under mechanical deformation. There is a lack of experimental data for both pure and doped versions of the YSO compound. However, the accuracy of the photoelastic constants can still be probed by comparing the difference between the elastic constants and refractive indices of the pure and doped compounds.

Table 3 displays the piezo-optic constants for both pure and Eu-doped YSO. The choice of functional for our calculations was based on the values of refractive indices presented in Table 1.

Table 2. Elastic constants of YSO, and Eu:YSO, C_{ij} in GPa.

	c_{11}	c_{12}	c_{13}	c_{15}	c_{22}	c_{23}	c_{24}	c_{33}	c_{34}	c_{44}	c_{46}	c_{55}	c_{66}
YSO-Exp. [25]	65.8	-	-	±70.6	185	-	-	83.5	±33.0	46.5	±0.14	187	65.6
YSO-PBE [9]	212.21	62.78	78.65	11.64	197	49.50	-13.56	173.21	-21.07	61.42	10.08	48.41	69.25
YSO-PBE [29]	226	88	59	5	201	27	-0.3	156	-0.2	44	10	67	63
Eu:YSO-PBE [9]	209.35	60.17	77.59	11.47	190.82	47.39	-13.62	173.15	-20.99	61.21	10.03	47.70	69.24

Specifically, we continued with the same type of functional, PBE0 since functional provided values closest to the experimental observations. In an ideal scenario, our methodology's accuracy would be confirmed by comparing our calculated photoelastic constants with experimental equivalents. However, for both pure and Eu-doped YSO, such data is currently unavailable. As a workaround, we validated our calculated piezo-optic and inherent elasto-optic constants via their application in FEM simulations. In these simulations, we applied loads and post-processed the results using the calculated piezo-optic constants. If the refractive index resulting from these simulations, after the load application, aligns with the available experimental refractive index under similar conditions, we can assert that our piezo-optic constants are correctly determined.

Table 3. Piezo-optic constants of Eu:Y_2SiO_5, π_{ij}. Unit=Brewsters, 1B = $10^{-12}\ Pa^{-1}$.

YSO	π_{11}	π_{12}	π_{13}	π_{15}	π_{21}	π_{22}	π_{23}	π_{25}	π_{31}	π_{32}
PBE0-D3	-0.603	0.880	1.184	-1.223	0.164	0.551	0.557	-0.131	0.337	0.725
Eu:YSO	π_{11}	π_{12}	π_{13}	π_{15}	π_{21}	π_{22}	π_{23}	π_{25}	π_{31}	π_{32}
PBE0-D3	-0.634	1.921	1.457	-1.229	0.195	1.580	0.815	-0.131	0.478	1.611
YSO	π_{33}	π_{35}	π_{44}	π_{46}	π_{51}	π_{52}	π_{53}	π_{55}	π_{64}	π_{66}
PBE0-D3	0.313	0.365	-0.353	-0.037	-0.504	-0.073	0.459	-0.594	0.117	-1.476
Eu:YSO	π_{33}	π_{35}	π_{44}	π_{46}	π_{51}	π_{52}	π_{53}	π_{55}	π_{64}	π_{66}
PBE0-D3	0.440	0.489	0.032	-0.268	-0.442	-0.281	0.269	-0.572	0.025	-1.526

Table 4. elasto-optic constants of Y_2SiO_5, p_{ij}.

YSO	p_{11}	p_{12}	p_{13}	p_{15}	p_{21}	p_{22}	p_{23}	p_{25}	p_{31}	p_{32}
PBE0-D3	0.41	0.147	0.158	-0.058	0.118	0.124	0.124	0.002	0.140	0.162
Eu:YSO	p_{11}	p_{12}	p_{13}	p_{15}	p_{21}	p_{22}	p_{23}	p_{25}	p_{31}	p_{32}
PBE0-D3	0.110	0.189	0.195	-0.055	0.149	0.182	0.150	-0.000	0.172	0.197
YSO	p_{33}	p_{35}	p_{44}	p_{46}	p_{51}	p_{52}	p_{53}	p_{55}	p_{64}	p_{66}
PBE0-D3	0.109	0.032	-0.022	-0.006	-0.067	-0.037	0.028	-0.028	-0.011	-0.071
Eu:YSO	p_{33}	p_{35}	p_{44}	p_{46}	p_{51}	p_{52}	p_{53}	p_{55}	p_{64}	p_{66}
PBE0-D3	0.110	0.032	-0.003	-0.010	-0.071	-0.049	0.014	-0.028	-0.024	-0.062

To perform a comparative analysis, we utilized the measured values of relative permittivity from the study by Carvalho et al. [10]. These values denote the real permittivity of pure YSO crystal against varying temperatures with uncertainty of below 0.26% [10]. As the YSO crystal is a biaxial dielectric material with known refractive indices at optical frequencies, its permittivity plays a crucial role in this comparison. Following this, we commenced with the application of thermal stress on the YSO crystal. The temperature model employed is a thermomechanical one,

where any temperature exceeding 0 K incites a mechanical load on the crystal, thereby inducing stress on the unit cell. This stress is then post-processed via the application of piezo-optic constants. This step assists in obtaining the refractive indices influenced by the stress, thereby allowing us to perform an analysis of the material's behavior under thermal conditions.

The plot illustrated in Figure 4, and 5 present the variations in both measured and calculated refractive indices as a function of temperature changes. The measured values are represented by a blue curve, while the calculated values are designated by a red curve. Upon initial observation, a divergence in the patterns of these curves becomes apparent. The blue curve seems to follow a quadratic equation, whereas the red curve appears to possess a linear trait. The main reason behind the linearity of the calculated result may be the extracted photoelastic constants that are actually a result of Pockel's effect [30], which is intrinsically a linear effect. It should be added that Pockels' effect is essentially a term allocated to linear electro-optic effect [11]. Since there is no specific term for linear elasto-optic effect, we have extended the definition of Pockels' effect to linear elasto-optic effect. Therefore, the quadratic trait of the calculated curve can be achieved if the extracted photoelastic constants were obtained with nonlinear traits. To do this, one has to include the non-linear effect known as Kerr effect [11]. Again, the Kerr effect is a term coined for non-linear electro-optic effect but we extend its definition to cover nonlinear elasto-optic effects as well.

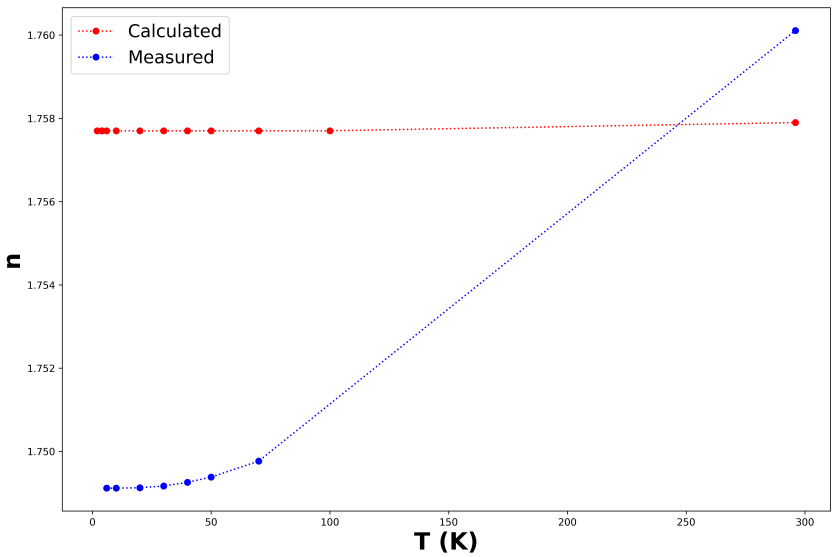

Fig. 4. The comparison between measured and calculated value of the refractive index along D_1 direction.

To observe the orientation-dependent of the n versus temperature, we can refer to Figure 6. Here we have plotted the variation of n in principle axes for both measured and calculated data. In all directions, we observe the quadratic type curve for the measured data and the linear type curve for the calculated data. It is clear that the calculated model follows the right trend with increasing temperature. However, a direct comparison of the curves may not accurately represent the relationship between the data. A closer examination of the relative difference between each data point on the blue curve and its corresponding point on the red curve reveals a very small disparity of only 0.0024. This indicates that, despite their differing patterns, the measured and calculated data are in close agreement. Additionally, it is worth noting that the quadratic behavior

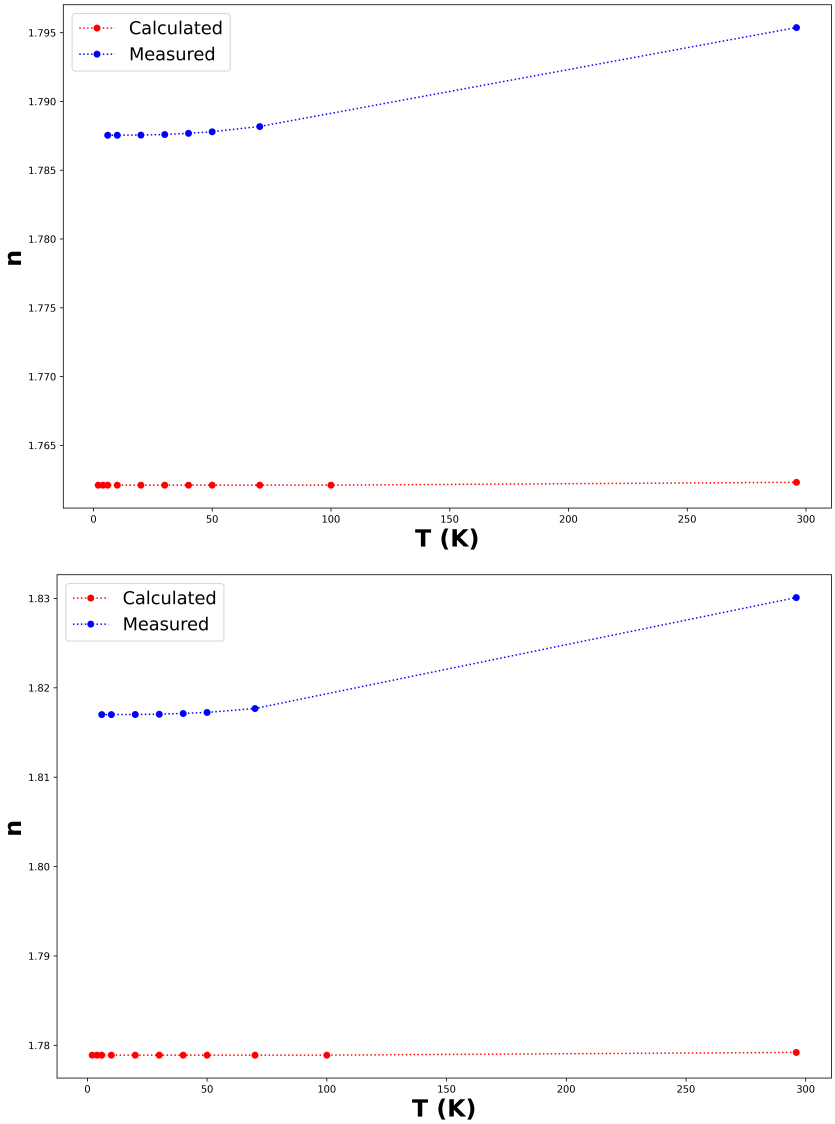

Fig. 5. The comparison between measured and calculated value of the refractive index along b, and D_2 direction.

of thermo-optic coefficients appears to be specific to YSO. Other monoclinic systems, such as Ga2O3, have exhibited linear thermo-optic coefficients [31]. Additionally, considering the fitted polynomials for the measured and calculated curves, we find the corresponding coefficients are as follows: a = 1.3×10^{-7}, b = 2.4×10^{-7}, c = 1.7(4908) for the measured curve and a = 3.1×10^{-9}, b = -2.712×10^{-7}, c = 1.7(5770) for the calculated curve. These findings further reinforce the linearity of the calculated data as the coefficient of x^2 being a, is in order of 10^{-9} while the a for the measured data is in order of 10^{-7}.

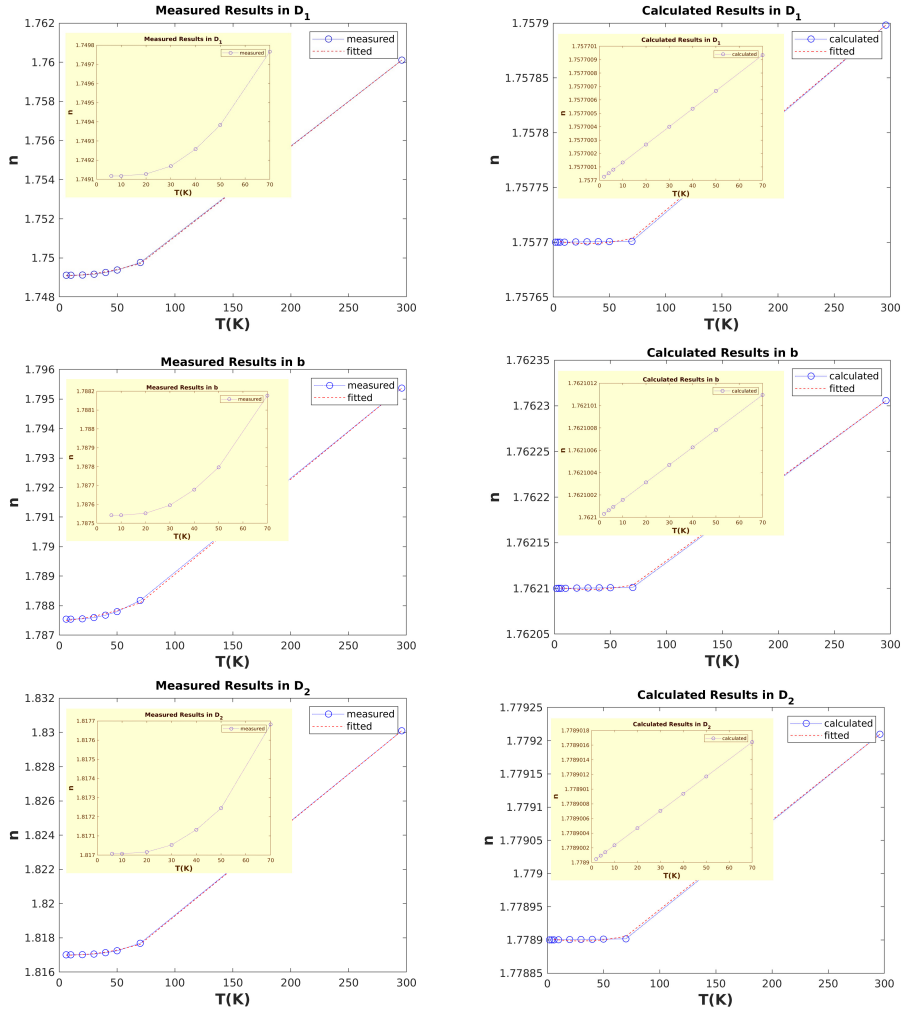

Fig. 6. The measured and calculated values of n in all three optic directions of pure YSO are between 6 to 296 Kelvin.

Our calculated results can be further substantiated through a direct comparison with empirical data sourced from Carvalho et al. [10]. A side-by-side representation of the corresponding values for our measurements and calculations is presented in Table 5, with data points spanning from 6 to 296 K. Remarkably, for the D_1 orientation, the deviation in our point-to-point comparison is minimal. Additionally, the percentage of error remains unchanged across the entire temperature range. For the sake of specificity, the maximum errors at D_1, b, and D_2 stand at 0.49, 1.84, and 2.78 respectively. The parentheses around the value of n after the decimal point are only added to help the reader see how n changes along the temperature interval. It's important to

Table 5. Comparison of measured and calculated refractive indices versus temperature for pure YSO. The measured data is taken from [10].

	measured			**calculated**			**Error**		
Temp. (K)	n_{D1}	n_b	n_{D2}	n_{D1}	n_b	n_{D2}	Err.D_1 (%)	Err.b (%)	Err.D_2 (%)
6	1.749(1174)	1.787(5427)	1.817(0071)	1.757(7000)	1.762(100094)	1.778(9001)	0.490	1.423	2.097
10	1.749(1174)	1.787(5427)	1.817(0071)	1.757(7001)	1.762(100156)	1.778(9002)	0.490	1.423	2.097
20	1.749(1276)	1.787(5528)	1.817(0162)	1.757(7002)	1.762(100313)	1.778(9004)	0.490	1.423	2.097
30	1.749(1687)	1.787(5952)	1.817(0529)	1.757(7004)	1.762(100469)	1.778(9007)	0.487	1.426	2.099
40	1.749(2575)	1.787(6784)	1.817(1321)	1.757(7005)	1.762(100626)	1.778(9009)	0.482	1.430	2.103
50	1.749(3836)	1.787(7965)	1.817(2445)	1.757(7006)	1.762(100782)	1.778(9011)	0.475	1.437	2.109
70	1.749(7664)	1.788(1770)	1.817(6818)	1.757(7009)	1.762(101095)	1.778(9016)	0.453	1.458	2.133
296	1.760(1088)	1.795(3696)	1.830(0966)	1.757(8983)	1.762(305584)	1.779(2097)	0.125	1.841	2.780
100	1.7(5035)	1.7(8859)	1.8(18360635)	1.7(5770)	1.7(6210)	1.7(7890)	0.419	1.481	2.169
500	1.7(8046)	1.8(0887)	1.8(5505)	1.7(5832)	1.7(6274)	1.7(7986)	1.243	2.550	4.052
1000	1.8(7438)	1.8(6975)	1.9(7115)	1.7(5933)	1.7(6366)	1.7(8127)	6.083	5.610	9.543

highlight that for direction b and D_2, the error seems to amplify faster as temperature increases. To better understand the magnitude of error at higher temperatures, we utilize a curve that has been fitted to predict the error beyond room temperature. The last three rows of Table 5 display the measured values of the refractive indices—calculated using the fitted curves—in comparison with the computed data. A significant rise in error is discernible at the 500 and 1000 K points. It is crucial to recognize that the operating temperature for some rare-earth activated phosphors is typically at or slightly above room temperature. For instance, the temperature required for laser stabilization is at cryogenic levels [2, 4], while for common phosphor applications, like lighting LEDs, the operating temperature tends to be near or just above room temperature [32]. Thus, we can assert that the predictions of the model align with experimental findings and are applicable for practical uses. At least, this is the case for applications up to and smaller than room temperature.

After constructing and verifying the ability of the model to produce reasonable results, we proceeded to investigate the changes in refractive indices with respect to the temperature of Eu-doped YSO. The Eu concentration for the doped system was maintained at 6.25% to remain consistent with our previous study [9], and it should be mentioned that the doping is performed only for site 1 of YSO. The results of these computations are detailed in Table 6. Consistent with the findings for the undoped system, the doped system also exhibits a linear pattern in its refractive indices.

Based on these calculated refractive indices, one can track the shift of resonance frequency for pure YSO and Eu-doped YSO medium. Figure 7 shows the shift of the frequency with respect to temperature. As the figure shows, the trend of the curves in both cases (pure and doped) are linear and have an increasing trend in which the value of the principle axes keeps the same order of magnitude D_2>b>D_1.

Next, our study involves assessing the impact of applying compressive and tensile loads directly

Table 6. Calculated refractive indices for Eu-doped YSO with respect to temperature.

Temp. (K)	n_{D1} = 1.7691	n_b=1.7692	n_{D2}=1.7892
2	n_{D1}+6.6e-8	n_b+7.9e-8	n_{D2}+9.4e-8
4	n_{D1}+1.33e-7	n_b+1.58e-7	n_{D2}+1.87e-7
6	n_{D1}+1.99e-7	n_b+2.37e-7	n_{D2}+2.81e-7
10	n_{D1}+3.32e-7	n_b+3.95e-7	n_{D2}+4.68e-7
20	n_{D1}+6.64e-7	n_b+7.9e-7	n_{D2}+9.35e-7
30	n_{D1}+9.96e-7	n_b+1.185e-6	n_{D2}+1.403e-6
40	n_{D1}+1.328e-6	n_b+1.58e-6	n_{D2}+1.871e-6
50	n_{D1}+1.66e-6	n_b+1.975e-6	n_{D2}+2.339e-6
70	n_{D1}+2.324e-6	n_b+2.766e-6	n_{D2}+3.274e-6
100	n_{D1}+3.211e-6	n_b+3.821e-6	n_{D2}+4.524e-6
296	n_{D1}+4.46e-4	n_b+5.17e-4	n_{D2}+6.16e-4

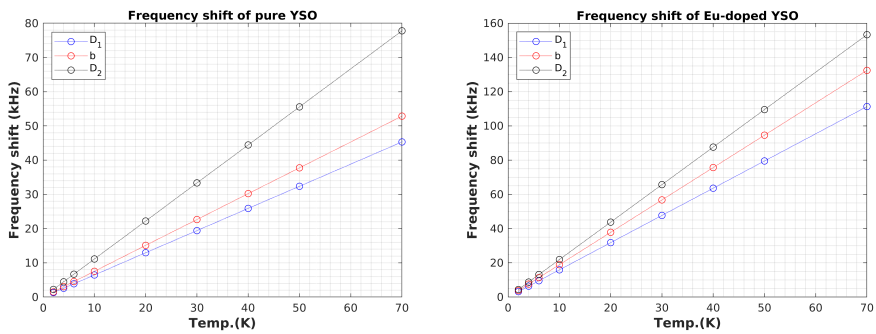

Fig. 7. The variation of resonance frequency with respect to temperature.

to the crystal, specifically focusing on the variation of n in different orientations. We will reapply pressure to the crystal during the FE simulation, which previously provided us with the stress tensor. This tensor will then be subjected to further post-processing via the piezo-optic tensor to derive the fluctuation of refractive indices in relation to the applied load.

Figure 8 illustrates how n changes in relation to the applied load in D_1, D_2, and D_1D_2 directions, as well as hydrostatic pressure. From previous observations, we can anticipate a linear trend, as the piezo-optic constants were derived based on Pockels' effect. The focal points in this instance are the slope of the hydrostatic pressure and the close approximation of the D_2 and D_1D_2. As you can see in all figures the maximum magnitude of change is related to hydrostatic pressure, and the curves corresponding to D_2 and D_1D_2 are almost overlapping which might be explained due to the larger magnitude of n in D_2 direction.

Interestingly, the doped crystal (Figure 9) exhibits similar behavior to the pure system. To discern the differences between the pure and doped systems, we have contrasted the rates of change in resonance frequencies for both systems, as tabulated in Table 7. The table demonstrates

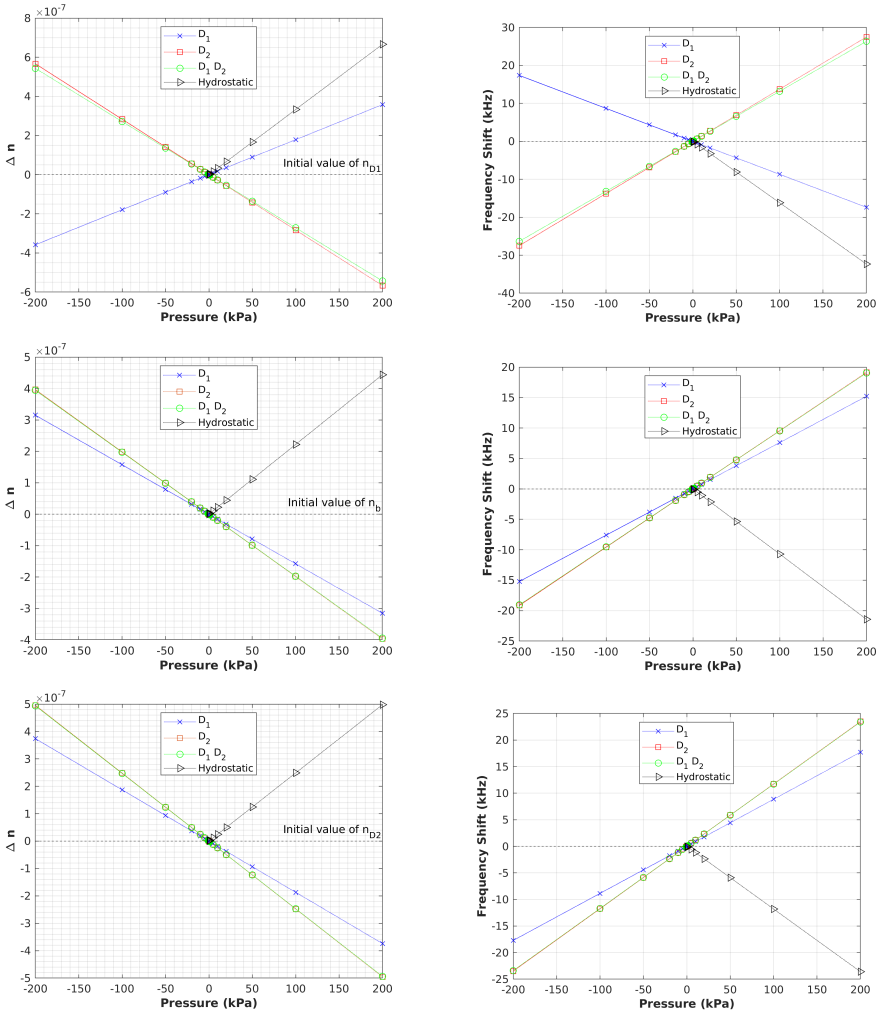

Fig. 8. The change in refractive indices and frequency shift of pure YSO with respect to the applied load.

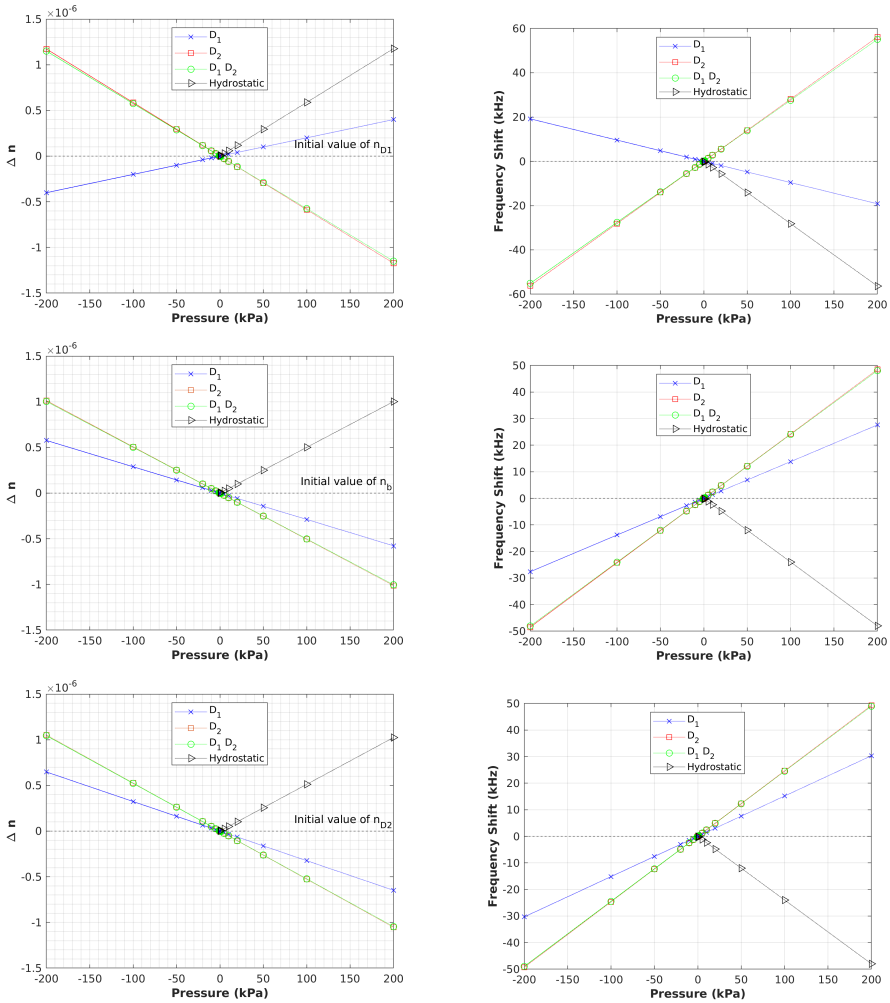

Fig. 9. The change in refractive indices and frequency shift of Eu-doped YSO with respect to applied load.

that doping results in a steeper slope - as far as the magnitude of the slope is concerned - across all orientations. Therefore, one could deduce that doping accelerates the rate of change in refractive indices, and by extension, the resonance frequency. Regrettably, there are no such data available to corroborate this for YSO, although a study conducted by Soharab et al. [33] analyzed the refractive index versus Nd concentration in $GdVO_4$, which seems to support the increasing trend of refractive indices with dopant concentration.

4. conclusion

In this study, a multi-scale modeling workflow was developed and we have managed to calculate the thermo-optic coefficients (dn/dT) of pure and Eu-doped YSO. To achieve this the piezo-optic constants were extracted with the application of DFPT, and the calculated constant was validated

Table 7. The rate of change of resonance frequency (df/dP) for pure & Eu-doped YSO with respect to applied load.

LoadAxis	Doped	n_{D_1}	n_b	n_{D_2}
D_1	no	-0.0869	0.0761	0.0886
D_1	yes	-0.0960	0.1381	0.1517
D_2	no	0.1375	0.0957	0.1174
D_2	yes	0.2810	0.2424	0.2465
D_1D_2	no	0.1318	0.0952	0.1169
D_1D_2	yes	0.2754	0.2402	0.2448
Hydrost.	no	-0.1616	-0.1071	-0.1179
Hydrost.	yes	-0.2818	-0.2399	-0.2399

using the measured value of the dn/dT for the pure YSO. For the selected temperature interval (6 - 296 K) the maximum error between calculated and measured values was at 2.78% in D_2 direction. The main discrepancy between the developed model and the measured data is the type of polynomials that they fit in. While the measured data follow a quadratic equation the calculated data shows a linear behavior. As we mentioned in the result section, this must be due to the fact that we have extracted the piezo-optic constant based on Pockels' effect which is a linear approach in its origin. So, to decrease the discrepancy between calculated and measured data non-linear effects known as Kerr's effect must be added to the process of piezo-optic extraction. Nevertheless, the workflow produces reasonable results for at least the selected temperature interval. The produced results presented in Table 5 are important as they enable the estimation of thermo-optic coefficients, which is crucial for the optimization and design of the optical cavity.

Using the piezo-optic post-processing method, we successfully observed variations in refractive indices for different applied loads and their respective frequency shifts. Our observations indicate that hydrostatic pressure induces the most significant variation in the refractive index. Furthermore, a linear relationship exists between the applied load and the change in refractive index n. Doping amplifies the variation magnitude, regardless of its orientation or magnitude of the applied load. Thus, it can be inferred that an increase in impurity concentration amplifies the variation in n and subsequently affects the resonance frequency.

The accuracy of the results with respect to experimental and the applicability of this approach for other host materials and dopants and the ease of the workflow suggest that the current approach has the potential to be a straightforward alternative for the tedious experimental measurement. This is especially the case for low-symmetry materials such as YSO. Nevertheless, the main purpose of this work was to propose an approach to examine variation of the refractive indices for RE-doped YSO in which we believe we have shown it is possible to do so to a large degree. Except for the high-temperature cases, where the operating temperatures of the experiments exceed the room temperature.

5. Appendix

$$D_1 = \begin{pmatrix} \delta & 0 & 0 \\ 0 & \delta & 0 \\ 0 & 0 & \delta \end{pmatrix} D_2 = \begin{pmatrix} 2\delta & 0 & 0 \\ 0 & -\delta & 0 \\ 0 & 0 & -\delta \end{pmatrix} D_3 = \begin{pmatrix} 0 & \delta & 0 \\ \delta & 0 & 0 \\ 0 & 0 & 0 \end{pmatrix}$$

$$D_4 = \begin{pmatrix} 0 & 0 & 0 \\ 0 & \delta & 0 \\ 0 & 0 & -\delta \end{pmatrix} D_5 = \begin{pmatrix} 0 & 0 & \delta \\ 0 & 0 & 0 \\ \delta & 0 & 0 \end{pmatrix} D_6 = \begin{pmatrix} 0 & 0 & 0 \\ 0 & 0 & \delta \\ 0 & \delta & 0 \end{pmatrix}$$

6. Acknowledgments

The authors are grateful to Matheus Amarante Machado and Jimmy Bisou for their assistance in FEM simulations and the post-processing stage. This work is supported by the Knut & Alice Wallenberg Foundation through grant no.: KAW-2016.0081. The simulations were performed using computational resources provided by the Swedish National Infrastructure for Computing (SNIC) at UPPMAX, Uppsala University, the NSC, Linköping University, and the PDC, Royal Institute of Technology.

Disclosures

The authors declare no conflicts of interest.

References

1. A. Konijnenberg, A. Adam, and P. Urbach, *BSc Optics* (TU Delft Open, 2021).
2. M. J. Thorpe, L. Rippe, T. M. Fortier, M. S. Kirchner, and T. Rosenband, "Frequency stabilization to 6 × 10-16 via spectral-hole burning," Nat. Photonics **5**, 688–693 (2011).
3. J. Millo, D. V. Magalhães, C. Mandache, Y. Le Coq, E. M. L. English, P. G. Westergaard, J. Lodewyck, S. Bize, P. Lemonde, and G. Santarelli, "Ultrastable lasers based on vibration insensitive cavities," Phys. Rev. A **79**, 053829 (2009).
4. N. Galland, N. Lučić, B. Fang, S. Zhang, R. Le Targat, A. Ferrier, P. Goldner, S. Seidelin, and Y. Le Coq, "Mechanical tunability of an ultranarrow spectral feature of a rare-earth-doped crystal via uniaxial stress," Phys. Rev. Appl. **13**, 044022 (2020).
5. A. D. Ludlow, M. M. Boyd, J. Ye, E. Peik, and P. O. Schmidt, "Optical atomic clocks," Rev. Mod. Phys. **87**, 637–701 (2015).
6. J. M. Hogan and M. A. Kasevich, "Atom-interferometric gravitational-wave detection using heterodyne laser links," Phys. Rev. A **94**, 033632 (2016).
7. P. Ghelfi, F. Laghezza, F. Scotti, G. Serafino, A. Capria, S. Pinna, D. Onori, C. Porzi, M. Scaffardi, A. Malacarne *et al.*, "A fully photonics-based coherent radar system," Nature **507**, 341–345 (2014).
8. X. Gonze, "Adiabatic density-functional perturbation theory," Phys. Rev. A **52**, 1096–1114 (1995).
9. A. Mirzai, A. Ahadi, S. Melin, and P. Olsson, "First-principle investigation of doping effects on mechanical and thermodynamic properties of y2sio5," Mech. Mater. **154**, 103739 (2021).
10. N. Carvalho, J.-M. Le Floch, J. Krupka, and M. Tobar, "Multi-mode technique for the determination of the biaxial y2sio5 permittivity tensor from 300 to 6 k," Appl. Phys. Lett. **106** (2015).
11. J. F. Nye *et al.*, *Physical properties of crystals: their representation by tensors and matrices* (Oxford university press, 1985).
12. J. Jellison, Gerald E., E. D. Specht, L. A. Boatner, D. J. Singh, and C. L. Melcher, "Spectroscopic refractive indices of monoclinic single crystal and ceramic lutetium oxyorthosilicate from 200 to 850 nm," J. Appl. Phys. **112** (2012). 063524.
13. G. E. Jellison, M. A. McGuire, L. A. Boatner, J. D. Budai, E. D. Specht, and D. J. Singh, "Spectroscopic dielectric tensor of monoclinic crystals: Cdwo$_4$," Phys. Rev. B **84**, 195439 (2011).
14. G. Erdei, N. Berze, Á. Péter, B. Játékos, and E. Lőrincz, "Refractive index measurement of cerium-doped luxy2-xsio5 single crystal," Opt. Mater. **34**, 781–785 (2012).
15. C. Li, C. Wyon, and R. Moncorge, "Spectroscopic properties and fluorescence dynamics of er/sup 3+/and yb/sup 3+/in y/sub 2/sio/sub 5," IEEE journal quantum electronics **28**, 1209–1221 (1992).
16. A. Ferrier, B. Tumino, and P. Goldner, "Variations in the oscillator strength of the 7f0→5d0 transition in eu3+:y2sio5 single crystals," J. Lumin. **170**, 406–410 (2016). SI: Lanthanide spectroscopy.

17. E. Hecht, *Optik* (De Gruyter, Berlin, Boston, 2018).
18. T. S. Narasimhamurty, *Photoelastic and electro-optic properties of crystals* (Springer Science & Business Media, 2012).
19. R. Dovesi, A. Erba, R. Orlando, C. M. Zicovich-Wilson, B. Civalleri, L. Maschio, M. Rérat, S. Casassa, J. Baima, S. Salustro *et al.*, "Quantum-mechanical condensed matter simulations with crystal," Wiley Interdiscip. Rev. Comput. Mol. Sci. **8**, e1360 (2018).
20. G. Kresse and J. Furthmüller, "Efficiency of ab-initio total energy calculations for metals and semiconductors using a plane-wave basis set," Comput. Mater. Sci. **6**, 15 – 50 (1996).
21. C. Adamo and V. Barone, "Toward reliable density functional methods without adjustable parameters: The pbe0 model," The J. chemical physics **110**, 6158–6170 (1999).
22. J. P. Perdew, K. Burke, and M. Ernzerhof, "Generalized gradient approximation made simple," Phys. Rev. Lett. **77**, 3865–3868 (1996).
23. Z. Sun, M. Li, and Y. Zhou, "Thermal properties of single-phase y2sio5," J. Eur. Ceram. Soc. **29**, 551–557 (2009).
24. J. Marion and R. Beach, "Thermophysical properties of y2sio5 (yos)," (1990).
25. M. J. Weber, *Handbook of optical materials*, vol. 19 (CRC press, 2002).
26. Y. Chen, D. Zhang, Z. Peng, M. Yuan, and X. Ji, "Review of research on the rare-earth doped piezoelectric materials," Front. Mater. **8** (2021).
27. X. Wang, X. Shi, R. Zhang, Y. Shi, Y. Liang, B. Zhang, H. Li, S. Hu, K. Yu, Y. Hu *et al.*, "Effect of co doping on microstructure, dielectric, and energy storage properties of bczt ceramics," J. Mater. Sci. Mater. Electron. **33**, 20399–20412 (2022).
28. E. T. Miyazono, "Nanophotonic resonators for optical quantum memories based on rare-earth-doped materials," Ph.D. thesis, California Institute of Technology (2017).
29. Y. Luo, J. Wang, J. Wang, J. Li, and Z. Hu, "Theoretical predictions on elastic stiffness and intrinsic thermal conductivities of yttrium silicates," J. Am. Ceram. Soc. **97**, 945–951 (2014).
30. A. Erba, M. T. Ruggiero, T. M. Korter, and R. Dovesi, "Piezo-optic tensor of crystals from quantum-mechanical calculations," The J. Chem. Phys. **143**, 144504 (2015).
31. I. Bhaumik, R. Bhatt, S. Ganesamoorthy, A. Saxena, A. K. Karnal, P. K. Gupta, A. K. Sinha, and S. K. Deb, "Temperature-dependent index of refraction of monoclinic ga2o3 single crystal," Appl. Opt. **50**, 6006–6010 (2011).
32. I. Ayoub, U. Mushtaq, N. Hussain, S. Rubab, R. Sehgal, H. C. Swart, and V. Kumar, "8 - rare-earth-activated phosphors for led applications," in *Rare-Earth-Activated Phosphors,* V. Dubey, N. Dubey, M. M. Domańska, M. Jayasimhadri, and S. J. Dhoble, eds. (Elsevier, 2022), pp. 205–240.
33. M. Soharab, I. Bhaumik, R. Bhatt, A. Saxena, and A. Karnal, "Effect of nd doping on the refractive index and thermo-optic coefficient of gdvo 4 single crystals," Appl. Phys. B **125**, 1–14 (2019).

Paper III

Amin Mirzai, Solveig Melin, Aylin Ahadi

Influence of impurity configuration on electronic and optical properties of Ce-doped YVO_4: Semi-local & hybrid functionals

Computational Material Science

DOI: 10.1016/j.commatsci.2022.111741

Computational Materials Science 214 (2022) 111741

Contents lists available at ScienceDirect

Computational Materials Science

journal homepage: www.elsevier.com/locate/commatsci

Full length article

Influence of impurity configuration on electronic and optical properties of Ce-doped YVO_4: Semi-local & hybrid functionals

Amin Mirzai *, Solveig Melin, Aylin Ahadi

Division of Mechanics, Department of Mechanical Engineering Sciences, Lund University, SE-22100 Lund, Sweden

ARTICLE INFO

Keywords:
DFT
Orthovanadates
Tetragonal
Rare Earth
refractive index
absorption coefficient

ABSTRACT

We investigate the impact of impurity configuration on electronic and optical properties of YVO_4 through application of plane-wave DFT. Since this crystal is a common host material for optical devices and it has been widely used as a phosphor and a laser host material, it is important to identify a correlation between impurity location and the intrinsic properties of the material. To further improve the accuracy of the results several semi-local and a hybrid functional are tested. To find the most stable structure among possible configurations of doping, the electronic structures and formation energies of the available configurations are calculated and compared. We report that while the valence is formed by O-*2p* orbitals and conduction is made of V-*3d* orbitals in all configurations, the band width varies with the impurity configuration. Additionally, the formation energy is changing depending on where the dopant is located. Then the absorption coefficient and the refractive index are obtained using a modified HSE functional.

1. Introduction

Yttrium Orthovanadate (YVO_4) belongs to the tetragonal point group $D_{4h}^{19}(I4_1/amd)$ and forms a crystal in a zircon-type structure [1]. It is an excellent birefringence crystal and has a broad transparency spectrum (400–5000 nm). Thus, it is suitable for laser host applications, and the YVO_4 doped with Rare Earth (RE) ions is widely used in optoelectronic devices [2]. For example, Nd^{3+}-doped YVO_4 is commonly used in diode-pumped solid lasers, while Eu^{3+}-doped YVO_4 powder is considered as a prominent red phosphor that has application in plasma display panels, and image detectors [3,4]. In general, the attractiveness of RE ions stems from the *4f* shell in which it has a direct effect on the luminescence of these ions and their corresponding host materials. However, Ce^{3+} ion's luminescence originates from the transition between *4f* and *5d* states. Since the *5d* shell falls outside the *5s* and *5p* shells, it strongly interacts with the host lattice [5]. As a result, the *5d* state gets broadened. This is why the Ce^{3+} spectrum covers a broad wavelength region from the UV to the visible light spectrum [6], and the surrounding crystalline environment has a substantial impact on *5d* energy levels of Ce^{3+}. Hence the application of Ce^{3+}-doped crystals specifically as a laser host, calls for higher accuracy to diminish the gap between theoretical and experimental results.

There have been a few studies that have looked into the properties of both zircon and scheelite structures of YVO_4. For example, the phase transition of YVO_4 under pressure, from zircon type to scheelite type structure is investigated by Raman et al. and Panchal et al. [7,8], while others have studied the photoluminescence properties of Ce^{3+}-doped YVO_4, experimentally [6,9–11]. In addition, Huang et al. has investigated the physical properties of the YVO_4 using Density Functional Theory (DFT) [12].

Yet, the application of YVO_4 as a laser host and a phosphor requires reducing the source of uncertainties as much as possible. As discussed earlier, this gains more significance in Ce^{3+}-doped YVO_4 since the conduction layer of Ce^{3+} is highly sensitive with respect to the surrounding crystalline environment. Consequently, the location of impurities in the crystal can affect the intrinsic properties of the host material. This means that identification of a relation between impurity configuration and concentration may assist the increase of the signal to noise ratio. Hence, we look into the low pressure phase of YVO_4, which is a zircon-type structure, to identify the most stable impurity configuration with the aid of several semi-local and a hybrid functionals. We use the low pressure structure since the applied pressure in experimental conditions, for laser host applications, will not exceed the phase transition threshold, 8.5 GPa [13].

One of the main factors in accuracy of DFT results is the choice of functionals, which gain importance when the main objective is to reduce discrepancies. In DFT, local density approximation (LDA) and semi-local general gradient approximations (GGA) are the most common functionals, although the LDA and the GGA underestimate the band gap due to their vanishing derivative discontinuity [14]. To

* Corresponding author.
E-mail address: amin.mirzai@mek.lth.se (A. Mirzai).

https://doi.org/10.1016/j.commatsci.2022.111741
Received 4 June 2022; Received in revised form 4 August 2022; Accepted 9 August 2022
Available online 30 August 2022

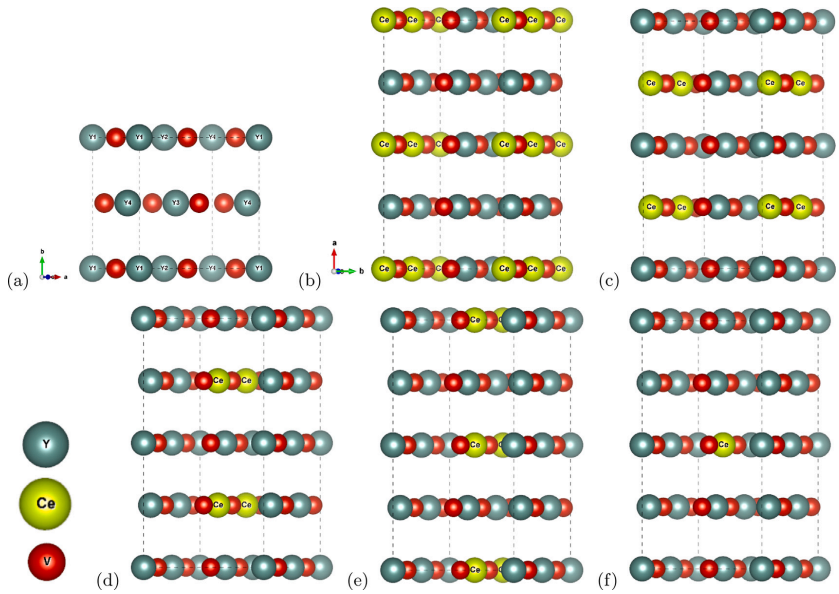

Fig. 1. Zircon-type structure of pure YVO_4 & Ce^{3+}-doped YVO_4 at Y1, Y2, Y3, and Y4 with 25% concentration, and Y3 with 6.25% concentration, respectively. While the pure structure is in a unit cell, the doped structures are in a 2 × 1 × 2 supercell. Note: To simplify, the Oxygen atoms are removed from the figures.

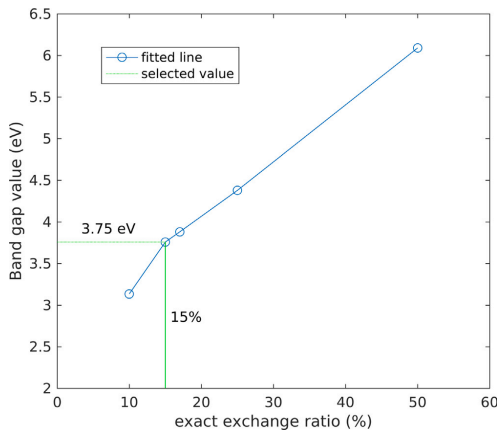

Fig. 2. Band gap values predicted for YVO_4 through variation of the HF contribution. The green dashed lines indicate the point at which the exchange tuning theoretically reproduces the experimental band gap.

explain this term, we must refer to the definition of fundamental band gap (E_G) for a system of N electrons, which is the difference between ionization potential (I) and its electron affinity (A) [15]:

$$E_G = I - A. \tag{1}$$

Although these two terms are accessible in the main definition of DFT, the Khon–Sham (KS) band gap is based on the difference between the eigenvalues of the conduction band minimum (CBM) and the valence band maximum (VBM):

$$E_G^{KS} = \varepsilon_{CBM} - \varepsilon_{VBM}. \tag{2}$$

Therefore, these two band gaps are not equal, and the difference between them is known as derivative discontinuity Δ_{xc} [16,17]:

$$E_G = E_g^{KS} + \Delta_{xc}. \tag{3}$$

The derivative discontinuity of LDA and GGA for solids is zero [14]. Consequently, the band gap obtained by LDA and GGA is underestimated, which may affect the accuracy of optical properties such as refractive index and absorption coefficient. To solve this issue, many-body approximations such as *GW* [18,19] and dynamical mean field theory (DMFT) [20] are employed. However, the computational cost of these techniques still remains the main obstacle in their application in more complex compounds such as YVO_4. Another option is to adopt a one shot *GW* approach, G_0W_0, which is less expensive. However, the perturbative nature of this approach makes it unsuited for total energy and structural optimization, which are valuable for treating systems with defects [21]. One other alternative that is applicable on solids with defects is the *DFT+U* method [22]. This technique is especially attractive since it is computationally more efficient with respect to hybrid functional. This is of course if we ignore the required calculation for finding the optimal U value. However, the problem with this technique is that it is often effective on only one aspect of the material under study and highly dependent on the type of the applied DFT method [23]. To clarify, the optimized U value found for optical properties of a material could not be ideal for other intrinsic properties of the material under study. It means while the optimal U value could lead to attaining the experimental band gap, it often could lead to miscalculation of structural properties such as lattice parameters and elastic constants [23]. Consequently, the application of *DFT+U* as a generic method may not be appropriate. Thus, a screened hybrid functional with plane-wave DFT is used to trade off the accuracy versus

speed, and to include the effect of localized electrons. In addition, we have tuned the portion of exact exchange in HSE06 [24] functional to increase the accuracy.

In this paper, we specifically examine the electronic and optical properties of the crystal in the linear response regime. In addition, the structural and elastic properties of the crystal are also checked to provide the most stable structure for the doped system. To summarize, the objectives of this work are to; (a) evaluate semi-local functionals, PBE, PBEsol, and AM05 with screened hybrid functional HSE06, (b) study the effects of impurity configuration on electronic and optical properties, and (c) observe the effect of impurity concentration on electronic and optical properties.

2. Theory & method

2.1. Computational method

The calculations are carried out by employing pseudopotential plane-wave DFT methodology as it is implemented in Vienna *ab-initio* Software Package (VASP) [25]. The Y: $4s^2 4p^6 4d^1 5s^2$, Si: $3s^2 3p^2$, O: $2s^2 2p^4$, and Ce: $4f^1 5d^1 6s^2$ electrons are treated as valence electrons whereas the core electrons and electron-ion interactions are treated by the projected augmented wave (PAW) method [26].

The optimization of unit cells, Fig. 1(a), in the case of PBE [27], AM05 [28], PBEsol [29] were carried out by setting the cut-off energy to 550 eV and selecting the conjugate gradient as relaxing algorithm. The main reason behind this selection is to test the latter two functionals that are specifically designed for solid materials, and to find the most suitable functional for this compound for follow-up studies. The sampling of the Brillouin zone was done through implementation of an automatically generated Γ-centered Monkhorst–Pack grid [30]. In order to minimize total energy, a $12 \times 12 \times 13$ mesh is adopted for all calculations, and a convergence threshold of 1×10^{-8} eV was used to reach self-consistency. The force criterion for geometry optimization was 0.00001 eV/Å.

Once the standard unit cell of the YVO_4 was converged, the elastic constants of the pure system were calculated using the same cut-off energy and k-points. Moreover, a $2 \times 1 \times 2$ supercell Fig. 1(b–f), was constructed to calculate the formation energy and the optical properties of the system. This is done to control the impurity concentration in the system. Besides, four different doping configurations, Fig. 1(b–f), were considered to observe the effects of impurity configuration. The cut-off energy was kept constant, 550 eV, whereas the k-point set for the supercell was selected to be $3 \times 5 \times 4$. The convergence threshold was set to 1×10^{-6} eV, and the force criterion for geometry optimization was 0.01 eV/Å.

As the general purpose exchange correlation potentials of LDA and GGA methods underestimate the band gap of the material, the hybrid functional is more suitable option to compute properties of a solid. Among those, screened hybrid functional HSE06 [24] happens to be performing the best [14]. Nevertheless, the standard HSE06 parameters are not optimal for general purpose as the so called mixing parameter is dependent on effective static dielectric constant, ϵ_∞, of a material [31]. Hence, finding the specific values for HSE parameters could lead to results comparable to multi-body approaches such as the *GW* approximation. The general form of the HSE06 functional is given as,

$$E_{xc}^{HSE} = aE_x^{HF,SR}(\omega) + (1-a)E_x^{PBE,SR}(\omega) + E_x^{PBE,LR}(\omega) + E_c^{PBE}, \quad (4)$$

where ω is the screening parameter and specifies the separation range, $E_x^{HF,SR}$ is the short-range HF exchange, $E_x^{PBE,LR}$ and $E_x^{PBE,SR}$ are the long-range and the short-range components of the PBE functional, and E_c^{PBE} is the PBE correlation energy. The parameter a is the HF mixing constant derived from perturbation theory [32]. This parameter, a, is the primary tool to obtain our desired accuracy. To fulfill this, the value of a is tuned with respect to experimental band gap (Fig. 2). All the subsequent HSE06 calculations are carried out using the tuned value of the a parameter.

Although hybrid functionals are computationally more efficient than many-body approximations, they are still more expensive to run in comparison with LDA and PBE functionals. To compensate for higher computational cost of the hybrid HSE06 functional $1 \times 3 \times 2$ and $2 \times 2 \times 3$ meshes are selected for supercell and unit cell, respectively. In addition, the cut-off energy is set to 10^{-6} eV from the previous value of 10^{-8} eV.

2.2. Defect formation energy

The formation energy is a suitable scale to gauge the thermodynamic stability of a system since it describes the amount of energy that leaves or enters the chemical reaction. It can be affected not only by the Fermi level due to electron potential but also the crystalline environment that is also related to electron potential. In this work, we have four different doping configurations in the standard zircon type unit cell of YVO_4 as they are depicted in Fig. 1. Therefore, the formation energy of each configuration is calculated using Eq. (5), as it is described in [33]. The four different doping configurations are represented with the total energy of the doped system in each configuration.

$$E_{form} = E_{doped} - E_{pure} + n_Y \mu_Y - n_{Ce}\mu_{Ce} \quad (5)$$

In Eq. (5), the E_{doped} is the total energy of Ce^{3+}-doped supercell, analogously the E_{pure} is the total energy of the pure system. μ_Y and μ_{Ce} are the chemical potential of Y and Ce, respectively. Finally, n_{Ce} and n_Y are the number of substituted Ce and removed Y, respectively. The respective chemical potentials are obtained from bulk structure unit cells with the assumption that the system resides in vacuum condition. In the rich Y condition the chemical potential of the Yttrium is extracted from the bulk energy of the element per atom. Similarly, the Ce chemical potential is extracted from the bulk energy of the element per atom.

2.3. Optical properties

The determination of optical properties helps us to understand the absorption spectra and the energy storage capacity of the system under study. These properties are directly related to a more fundamental property of the system known as the complex dielectric function. From the viewpoint of quantum mechanics, the interaction of a phonon with an electron in the system is described in terms of time-dependent perturbations of the ground electronic state, and the transitions between occupied and unoccupied states are caused by the phonon absorption or emission. The spectra resulting from excitation can be thought of as a joint density of states between the conduction and the valence band. This means the complex dielectric function reflects the relationship between dielectric function and band structure, and in the linear response range, the general form of dielectric function is described as below:

$$\epsilon(\omega) = \epsilon_1(\omega) + i\epsilon_2(\omega), \quad (6)$$

where ϵ_1 and ϵ_2 are the real and imaginary parts of the complex dielectric function, respectively. The imaginary is directly related to the electronic band structure and it can be obtained through the momentum matrix elements as it follows:

$$\epsilon_2(\omega) = \left(\frac{4\pi^2 e^2}{m^2\omega^2}\right) \sum_{i,j} \int_{BZ} \langle i|M|j\rangle^2 \, F_i(1-F_j)\delta(E_F - E_i - \omega) d^3k \quad (7)$$

where m is the free electron mass, ω is the frequency, i and j are the initial and final states respectively, M is the dipole matrix, and F_i is the Fermi distribution function for the ith state. The real part can be obtained through the Kramer–Kronig relation,

$$\epsilon_1(\omega) = 1 + \frac{2}{\pi} \int_0^\infty \frac{\omega'^2 \epsilon_2(\omega')}{\omega'^2 - \omega^2} d\omega'. \quad (8)$$

Table 1
Lattice parameters.

Type	a = b (Å)	c (Å)	Vol. (Å^3)	Dev. (%)
Exp. [34]	7.11	6.28	318.68	0
Exp. [13]	7.12	6.29	319.15	0
Exp. [6]	7.12	6.29	320	0
GGA [12]	7.18	6.31	325.50	1.94
LDA [12]	7.04	6.19	306.78	3.91
PBE	7.18	6.31	326.63	2.30
AM05	7.12	6.24	317.25	0.63
PBEsol	7.10	6.24	315.38	1.22
HSE06	7.22	6.36	332.68	4.19
HSE06$^{15\%}$	7.14	6.28	320.97	0.53

Once ϵ_1 and ϵ_2 are identified, other optical parameters, such as absorption coefficient, and refractive index can be obtained as it has shown below.

$$\alpha(\omega) = \frac{\sqrt{2}\omega}{c}\sqrt{\sqrt{\epsilon_1^2(\omega)+\epsilon_2^2(\omega)}-\epsilon_1(\omega)} \quad (9)$$

$$n(\omega) = \frac{1}{\sqrt{2}}\left(\sqrt{\epsilon_1^2(\omega)+\epsilon_2^2(\omega)}+\epsilon_1(\omega)\right)^{0.5} \quad (10)$$

3. Results

The results of geometric structural optimizations of zircon type YVO_4 unit cell are listed in Table 1. As it can be seen the optimizations are carried out for several XC functionals. It is worth mentioning that the experimental data provided in the first 3 rows of the table is used as the reference to compare the accuracy of the implemented functionals. The final column of the table dubbed as deviation shows how much the calculated results deviated from the provided experimental data. It should be added that deviations are calculated based on volume, and not on individual lattice parameters. The reference value of the volume is the average of the three experimental values, which is equal to 319.27 Å^3. The overall agreement of the results with respect to experimental data is satisfactory. This is especially true for the AM05 and modified version of the HSE06 [24] (HSE06$^{15\%}$), where the deviation percentages are 0.63% and 0.53%, respectively. On the other hand, the highest deviation belongs to the screened hybrid functional HSE06, and the PBE functional which is one of the most widely used functional. The deviation of HSE06 might probably be reduced by increasing k-points as it is reduced to 2 × 4 × 3. However, the deviation related to PBE may not be improved as both k-points and cutoff energy are set to high values. Hence, the error refers to the fundamental shortage of PBE, which is the lack of localization in the PBE wavefunction. The noticeable result in Table 1 belongs to the AM05 that has reproduced the experimental data with high accuracy and close to hybrid functional value while it is computationally comparable to LDA and PBE.

In the quest to find the appropriate functional to determine the optical properties we have also tested the band gap of the YVO_4 using all the aforementioned functionals. The results for band gap calculations are listed in Table 2. Analogous to Table 1, experimental values are included and their average is chosen as the reference point to measure the accuracy of the functionals. Additionally, the theoretical results of the study conducted by Shwetha et al. were also included to reinforce the reference point [35]. The last row of Table 2 belongs to HSE06$^{15\%}$ functional that is tuned with respect to the average of the experimental band gap (E_g = 3.75 eV). Fig. 2 shows the steps that have led to the appropriate portion of HF exact exchange in HSE06 functional. This is the reason the deviation of this functional is set to zero. As for the rest of the functionals, the absolute value of the difference between the average of the experimental band gap and the corresponding functional band gap is calculated and listed in Table 2. As the results indicate, all semi-local functionals underestimate the band gap. Among those, the PBE has the highest deviation. Although

Table 2
Band gap of zircon-type YVO_4 (the reference value would be the average of experimental values ΔE_g = 3.75).

	Band gap (eV)	Dev. (eV)	Dev. (%)
Exp. [37]	3.7	0	0
Exp. [38]	3.8	0	0
PBE	2.85	0.89	24
AM05	2.91	0.83	22.4
PBEsol	2.88	0.86	23.2
HSE06	4.37	0.62	16.53
TB-mBJ [35]	3.67	0.08	2.13
HSE06$^{15\%}$	3.75	0	0

Table 3
Formation energy of defect, in Y-rich environment.

E_{form} (eV)	Site	Dopant	Concentration
−1.156	Y1	Ce	25%
−1.146	Y2	Ce	25%
−1.189	Y3	Ce	25%
−1.138	Y4	Ce	25%
−3.437	Y3	Ce	6.25%

Table 4
Elastic constant of zircon-type YVO_4.

Type	C_{11}	C_{33}	C_{44}	C_{66}	C_{12}	C_{13}
PBE	221.56	286.81	18.16	44.02	45.30	80.31
PBEsol	245.77	315.60	17.94	45.19	51.16	86.05
AM05	234.10	307.82	15.79	44.54	45.25	83.25
HSE06$^{15\%}$	231.27	301.98	15.71	45.19	44.89	81.91
GGA [12]	216.10	284.80	21.90	45.50	44.30	78.80

the PBEsol and the AM05 show improvement over the PBE, they are still far from the average experimental band gap value. On the other hand, the HSE06 overestimates the band gap value just like it did with lattice parameters. Thus, it reinforces the idea that the HSE06 results can be improved with increasing cutoff and k-points. In addition, it must be mentioned that the band gap calculated from Kohn–Sham equations is the single particle band gap, which is an overestimation compared to room temperature experimental band gap [36]. It means the experimental band gap known as optical band gap is normally smaller in value with respect to single-particle band gap that is calculated at 0 K. Therefore, the calculated band gap with the standard HSE06 is not necessarily wrong, but it is not calculated for the right conditions.

The results of the formation energies are listed in Table 3. As it can be seen, the formation energy for Y3 shows the lowest energy that implies the ease with which a dopant can be incorporated within the host lattice. The last row of Table 3 indicates that the concentration of impurity has a significant impact on the final value of the formation energy. The concentration of the Ce^{3+} in the last system is reduced from 25% to 6.25% in the last row. A comparison between those two values of concentration implies that the higher the concentration the lower the stability of the compound.

To further reinforce the validity of our calculations, elastic constants were also calculated and compared in Table 4. The last row of this table exhibits the theoretical calculation of elastic constants, which can be used as a reference point. Overall, the calculated constants in this work are standing slightly higher than the reference with exception of C_{44} and C_{66}. The calculated values of constants in this work are in good agreement with each other, especially the values for AM05 and HSE06$^{15\%}$ as it was the case for lattice parameters in Table 1.

3.1. Electronic properties

As electronic structure is the main property that gets affected by shortcomings of semi-local XC functionals, we ignored the inclusion of

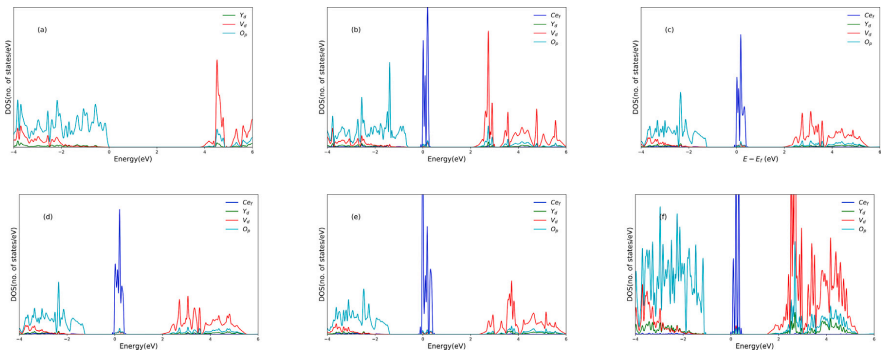

Fig. 3. Partial density of states of the pure (a), and doped configurations (b–f) based on HSE06$^{15\%}$ functional. The (f) is a 2 × 1 × 2 supercell.

semi-local functionals in this section. Fig. 3 depicts partial density states (PDOS) of all four configurations calculated using only HSE06$^{15\%}$ XC functional. In this figure, except Fig. 3(f) that is a 2 × 1 × 2 supercell, all other structures are basic unit cells of the YVO_4 (Fig. 1(a)). This is done to keep the computational cost as minimal as possible, and the fact that increasing cell size only increases the number of states at the corresponding energy level without affecting the peak locations and band width.

The Fig. 3 shows that the O-*2p* is the sole constituent of VBM and V-*3d* orbitals lies at the conduction CBM, and the localized Ce-*4f* states lie between aforementioned orbitals. Of course the localized behavior of *4f* electrons can be related to its position according to Aufbau rule. The *4f* orbital is shielded by *5s* & *5p* from the nucleus's side and *5d* & *6s* from the outer side. This position makes *4f* electrons to act like an atomic orbital, and this is why *4f* orbitals form an almost identical structure in all configurations. Nevertheless, the narrower shape and higher peak of the *4f* in Fig. 3(f) is due to lower concentration of impurity and larger size of the cell. Moreover, since the overall composition of VBM and CBM remains unchanged during doping one can deduce that the doping does not affect the overall contribution of atoms to electronic structure. On the contrary, doping does affect the band width. A quick comparison between pure structure (Fig. 3(a)) and the doped structures prove the reduction of O-*2p* → V-*3d* band width. In the figure, the smallest band width belongs to Y1 configuration with the value of 2.61 eV, while the largest band width belongs to Y4 configuration that is 3.61 eV. In any case there is a clear reduction of band width in doped structures compared to pure structure where the band width was 3.75 eV. The average band width reduction is 0.76 eV and the closest value to it belongs to Y3 configuration (0.73 eV).

Aside from the band width reduction, the figure also shows the shift of VBM to lower energies when doping occurs. This behavior can be explained by comparing elemental PDOS of pure structure with doped ones in Fig. 4. The appearance of Ce-*p* around −15 eV and broadening of Y-*p* around −17 eV in doped structures are the main cause of the down shifting of VBM. To clarify, as there are more states in lower energies at Ce-*p*, electrons tend to fill them up first. Moreover, the broadness of Y-*p* creates even more states to be filled around −17 eVs that shift down the VBM even further. This explanation can be reinforced through comparison of Y1 VBM (Fig. 4(b)) with other doped systems. The VBM states stay at higher energy level in Y1, (∼ −0.6089 eV), because the Y-*p* states has not been broadened as much as others. As the VBM shifts down to lower energies the CBM states also shift down. The amount in which the CBM states shift is comparable to downward shift of VBM as it can be seen in all unit cell doped structures. Nonetheless, the largest CBM shift belongs to 6.25% doped structure (Fig. 4(f)), which is mainly caused due to bigger size of supercell. The higher number of ions in each supercell can be interpreted as higher number of charge carrier which in turn pushes the VBM to higher energies; in addition, lower Ce^{3+} concentration leads to less number states of Ce-*p* at −15 eV which may lead to lesser pull effect on Fermi level. The same is true about CBM level in this structure, since there are higher number of states available for V_d the CBM is pushed slightly toward Ce-*4f* states. Adding this shift with total shift of band width due to existence of Ce-*p* and broadness of Y-*p*, results in large shift of CBM in this structure toward VBM. This is the main reason this structure has the shortest band width (2.6256 eV) after Y1 configuration despite the fact that Y-*p* is well broadened (Fig. 4(f)).

Table 5
Static dielectric constants.

	$\epsilon_{xx} = \epsilon_{yy}$	ϵ_{zz}
Exp. (15 °C) [40]	3.7818	4.6164
PBE	3.9357	4.8122
AM05	3.9831	4.8643
PBEsol	4.023856	4.909342
HSE06$^{15\%}$	3.9760	4.7346

3.2. Optical properties

Table 5 shows the static dielectric constant values for several XC functionals. The table shows close results, except for PBEsol. If we consider the experimental results as the reference, both the AM05 and the HSE06$^{15\%}$ are in good agreement. This is important since the AM05 functional in terms of computational expense is comparable to the LDA and the PBE while it has produced close results both to HSE06 and experimental. It should be added that the static dielectric constant for the hybrid functional cannot be directly calculated in VASP. As a result, the values shown in Table 5 are actually derived from the frequency dependant dielectric function of HSE06$^{15\%}$, where the static dielectric constant considered to be $\epsilon(0)$.

The optical properties of the Ce^{3+}-doped YVO_4 with different XCs and the pure host are compared in Fig. 5. In the figure, the main two properties under study are absorption coefficient, α, and refractive index, n. Both of these properties are relevant in laser host applications as both are directly related to the luminescence and birefringence of a crystal. It should be added that the AM05 functional is employed to carry out all the optical calculations for this figure, and the number of bands for dielectric function calculations were set to 540. Finally, both doped and pure systems have the 2 × 1 × 2 supercell structure to ease the comparison. The available configurations are shown in the legend of Fig. 5 as Y1 to Y4. The naming convention is associated with the position of Ce^{3+} ion in the host material as it is shown in Fig. 1(a). As we can see in Fig. 5(a), the refractive index undergoes a sudden drop

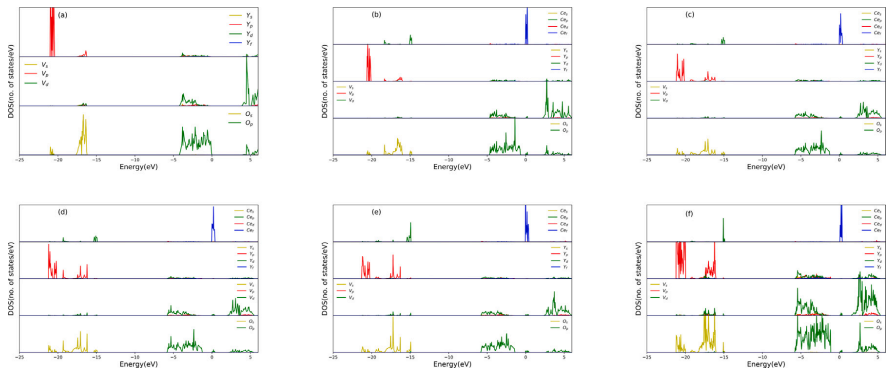

Fig. 4. Elemental partial density of states of the pure (a), and doped configurations (b–f) based on HSE06$^{15\%}$ functional. The (f) is a 2 × 1 × 2 supercell.

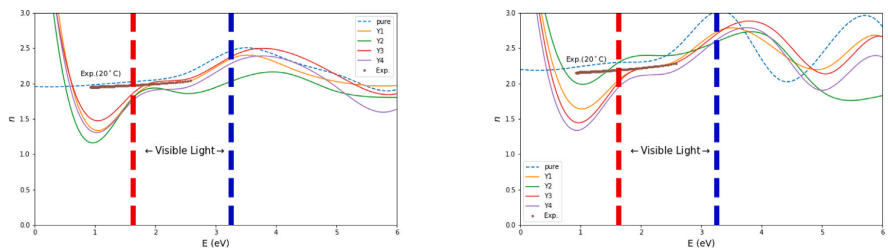

(a) Refractive index in xx-direction

(b) Refractive index in zz-direction

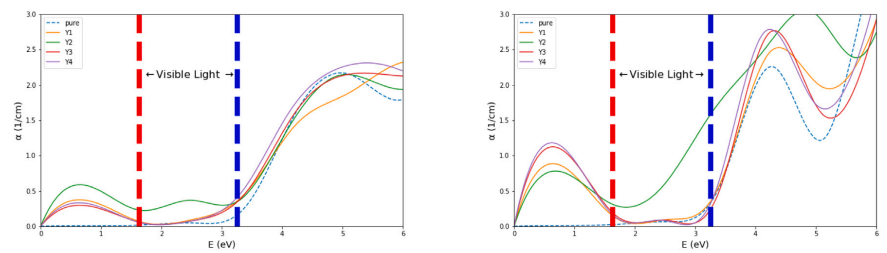

(c) Absorption coefficient in xx-direction

(d) Absorption coefficient in zz-direction

Fig. 5. Absorption coefficient & refractive index of pure YVO_4 & Ce^{3+}-doped YVO_4 for 2 × 1 × 2 supercell with the AM05 functional. The experimental values for refractive indices in both directions are taken from Shi et al. [39].

in the infrared region in both directions. The appearance of the well is only visible in doped structures, which suggests it is due to existence of impurity. At the xx-direction, from the deepest to the shallowest the order of the well is Y2, Y4, Y1, and Y3, respectively. While the order in the zz-direction organized as Y4, Y3, Y1, and Y2. Then in visible light region onward, the curves of all configurations follow the same pattern as pure structure curve with Y3 configuration curve being the closest in xx-direction and to some extent in zz-direction. It should be added that the curves of doped structures are blue shifted with 0.2–0.4 eV in xx and with 0.4–0.6 eV in zz direction. In absorption coefficient curves (Fig. 5(c & d)) however, no blue shift occurs in the infrared and in the visible light region. However, we do see a peak at infrared region, the order of peaks from the highest to lowest in xx-direction is Y2, Y1, Y4, Y3 and in zz-direction is Y4, Y3, Y1, Y2. In case of Y2 we observe a second peak in visible region in xx-direction and a rapid upward trend in zz-direction. One other anomaly that exists in doped structure curves is the starting value for the refractive indices. This can be seen in the infrared region of Fig. 5(a & b), where the value of doped systems asymptotically increases as we approach zero on the x-axis. The blue dashed lines in Fig. 5 belongs to pure crystal, and it is the only curve in the figure that starts from a reasonable value.

To overcome the observed anomaly in the previous figures, the HSE06$^{15\%}$ calculations are presented in Fig. 6. Additionally, two different doping concentrations are presented to visualize the effect of concentration. The AM05 curve of the pure system is also included in the same figure to compare the results between the AM05 and

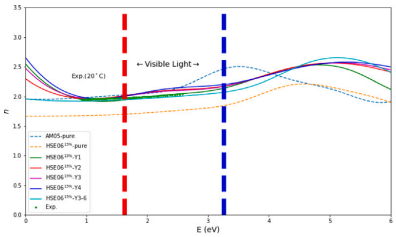

(a) Refractive index in xx-direction

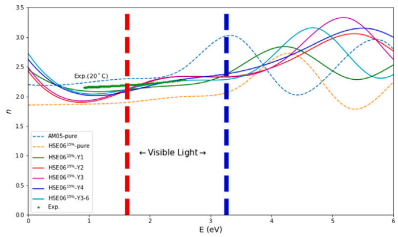

(b) Refractive index in zz-direction

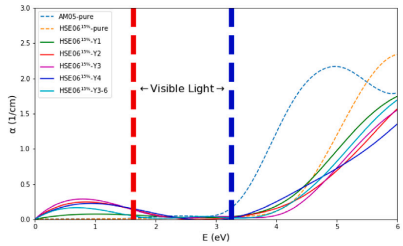

(c) Absorption coefficient in xx-direction

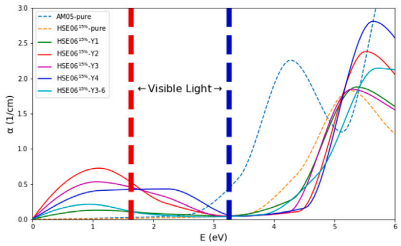

(d) Absorption coefficient in zz-direction

Fig. 6. Absorption coefficient & refractive index of pure YVO_4 & Ce^{3+}-doped YVO_4 with the AM05 and the HSE06$^{15\%}$ functionals. The experimental values for refractive indices in both directions are taken from Shi et al. [39]. Note: The plots of the full spectrum between 0–50 eV is available in Appendix A.

the HSE06$^{15\%}$ functional. In this figure, the pure systems and 6.25% concentration system are in $2 \times 1 \times 2$ supercell with 540 number of bands, and the rest of the doped systems are kept in a basic unit cell with 180 number of bands. The pure curve of HSE06$^{15\%}$ is blue shifted close to 1 eV in both refractive indices and absorption coefficients. Nevertheless, the HSE06$^{15\%}$ pure system follow a gradual almost linear upward trend up until the end of visible region and then experience a peak in UV region while the same peak occurs right at the end of visible region for AM05 curve. In doped structures, there is a sudden jump of value with respect to pure structures at $E = 0$ for refractive indices in both directions, Fig. 6(a & b). It should be also mentioned that the system with 6.25% doping has the lowest value (= 1.95) among the doped systems of refractive index at $E = 0$ in xx-direction while it possess the highest value in zz-direction (= 2.73). Right after this sudden jump we observe a downward trend in the infrared region of both directions of n in doped systems, although the trend is more pronounced in zz-direction. The highest deviation between configuration also occurs at the infrared region, and specifically at around $E = 0$. While the deviation in xx-direction is $\Delta n_{xx} = 0.69$, the value for $\Delta n_{zz} = 0.30$. The last point here is the experimental values of the pure structure that are plotted in the range of 0.92 to 2.58 eV. The measurement is carried out by Shi et al. at room temperature (20 °C) [39]. As we see in both directions the slope of the experimental curve agrees with both AM05 and HSE06$^{15\%}$ functionals in the designated range, although the agreement is more accurate in zz-direction. Moreover, it should be added that the experimental curve is much closer to the AM05 curve in both directions. However, towards the end of the experimental curve the AM05 curve starts to gain an upward momentum while the HSE06$^{15\%}$ curve remains more or less parallel with the experimental curve throughout the designated range, which may suggest further deviation of the AM05 curve from experimental curve if the range was larger. In case of absorption coefficients, there is no absorption in the infrared and visible region for the pure structures. However, the absorption occurs in all doped structures in the infrared region and visible regimes of xx-, and zz-directions (Fig. 6(c & d)). The absorption peaks occur specifically in the infrared region in both directions with the exception of the Y4 configuration in zz-direction, where it has broadened between the infrared and the visible regions. The peaks do not follow any specific order, hence, it is different in each direction. However, just like the refractive indices the curves follow the same pattern in xx-direction with Y1 having the lowest peak as it had the smallest O-$2p$ → V-$3d$ gap. Right after Y1, the Y3 with 6.25% concentration has the lowest peak as it had the smallest gap after Y1 as well. The remaining configurations do not follow the band width order. In zz-direction the peaks are more prominent and broader, and the peak order does not follow the band width order with the exception of the Y1 and Y3 with 6.25% concentration as we have seen in xx-direction. Hence, the absorption figures suggest that the band width of related configuration has greater effect on absorption than concentration of the impurity. We can see this in the infrared region of both directions, where the peak of Y1 with 25% concentration is lower than the 6.25% concentration structure. Since the band width variation is due to impurity configuration, one can infer that configuration selection can be effective in absorption tuning.

4. Discussion

Based on the results in this work we have observed that not only concentration percentage and cell size change the band width but also the location of the impurity changes the band width. As we discussed earlier this is mainly due to configuration dependent broadness of Y-p. The most notable effect of this, is the shrinkage of band width at Y1 configuration where the band width shrunk 1.14 eV. At the same time the Y2, Y3 and Y4 configuration each shrunk 0.70, 0.73 eV and 0.17 eV, respectively. One other effect of impurity configuration was on formation energy, where we found a maximum variation, $|\Delta E_{form}| =$ 0.051 eV, among Y3 and Y4 configurations. Nevertheless, the effect

of impurity concentration is recorded to be much higher in which the formation energy dropped to −3.43 eV. The overall effects of configuration on optical properties are more visible in zz-direction than xx-direction. The refractive index curve in zz-direction follow the same pattern from the infrared to near UV region and then starts to deviate from each other. Moreover, the absorption coefficient peaks are more prominent and deviated from each other in this direction (Fig. 6(d)). The difference in peaks between four configurations with 25% concentration is, $\Delta\alpha_{zz}$ = 0.61 cm^{-1}. Aside from the peaks, there is a clear difference between broadness of these configurations. According to the α_{xx} and α_{zz} curves the range of the broadness has direct association with concentration of the impurity than the configuration. As we can see in Fig. 6(c & d) the 6.25% concentration has a range of (0, ≈2) in xx- and (0, ≈2.6) in zz-direction. This is while the broadness difference in α_{xx} between the 25% configurations is negligible and the broadness in α_{zz} is as low as ≈0.16 eV.

It should be mentioned that the AM05 proved to yield results with good agreement either with previous calculation or experiment while keeping the same computational cost as PBE. Even though this work is not a generic study on efficiency and accuracy of AM05, it is recommendable instead of PBE functional for future studies of pure and maybe doped YVO_4, and might be applicable for other insulators as well. The areas where the AM05 failed were the electronic and the optical properties of the doped YVO_4. The anomaly in refractive index and absorption coefficient in the infrared region and possible misleading trends in the visible light region begs for application of hybrid or post-DFT calculations. This can be seen through a comparison of doped systems of the AM05 and the HSE06$^{15\%}$ calculations. Even at a high Ce^{3+} concentration, 25%, the refractive index should begin at lower value. To better gauge the estimated value of Ce^{3+}-doped YVO_4, and because experimental data for Ce^{3+}-doped YVO_4 refractive index is not available, the Yb-doped YVO_4 values are taken as the reference. The refractive index for 8% and 15% doped Yb^{3+} for xx- and zz-directions are 2.021, 2.023 and 2.253, 2.250, respectively [41]. Therefore, the AM05 functional obviously miscalculate the refractive index of Ce^{3+}-doped crystal with a large margin, which reinforces the usage of the HSE06$^{15\%}$ functional specifically in calculation of optical and electronic properties of systems with defect. On the other hand, finding the optimal HSE06 parameter proved to be effective as we have demonstrated here (Fig. 6), thus, in case higher accuracy is needed the tightening of convergence threshold would be sufficient to obtain more accurate results.

5. Conclusion

In summary, it was found that the configuration of impurity has indeed impact on the electronic structure, formation energy, and optical properties of the host crystal. The most notables are the variation of the band width and broadness of the absorption coefficient curve. The Y3 configuration is identified as the most stable configuration since it possesses the lowest formation energy and the closest value to average shrinkage of the band width. In the case of optical properties, the results demonstrate that doping is most effective in the infrared and the ultraviolet regions for both absorption and refractive index as compared to the visible region. Last but not least, doping concentration increases the absorption, specifically in the infrared region. In addition, we showed that the AM05 functional fail to capture the optical properties of the doped system as well as band gap value in the host system. However, the application of AM05 on YVO_4 and other Orthovanadate and maybe for other wide band gap materials seems to be an appropriate choice as both structural and optical properties of the host material are captured with good accuracy. Nonetheless, it is shown that a HSE06$^{15\%}$ solves the issue of the anomaly in refractive index and absorption coefficient while obtaining high accuracy results for structural properties. Additionally, further improvement of the results is achievable by selecting tighter convergence thresholds for the hybrid calculations.

CRediT authorship contribution statement

Amin Mirzai: Conceptualization, Methodology, Software, Formal analysis, Investigation, Data curation, Writing, Visualization, Supervision, Project administration. **Solveig Melin:** Review. **Aylin Ahadi:** Funding acquisition.

Declaration of competing interest

The authors declare the following financial interests/personal relationships which may be considered as potential competing interests: Aylin ahadi reports financial support was provided by Knut and Alice Wallenberg Foundation.

Data availability

Data will be made available on request.

Acknowledgments

This work is supported by the Knut and Alice Wallenberg Foundation through grant no. : KAW-2016.0081. The simulations were performed using computational resources provided by the Swedish National Infrastructure for Computing (SNIC) at UPPMAX, Uppsala university, at the NSC, Linköping University, and at the PDC, Royal institute of technology.

Appendix A. Supplementary data

Supplementary material related to this article can be found online at https://doi.org/10.1016/j.commatsci.2022.111741.

References

[1] E. Whittaker, (RWG) wyckoff. Crystal structures. Vol. 3.(2nd edn). New york, London, sydney (interseience publishers), 1965, viii+ 981 pp. illus. Price:£ 10s., Mineral. Mag. J. Mineral. Soc. 35 (275) (1966) 1022–1024.
[2] Y. Li, H. Jiang, T. Ni, T. Zhang, Z. Tao, Y. Zeng, Diode-pumped nd: YVO 4/Nd: YLF laser at 488 nm, Laser Phys. 21 (4) (2011) 677–679.
[3] R.A. Fields, M. Birnbaum, C.L. Fincher, Highly efficient nd:YVO4 diode-laser end-pumped laser, Appl. Phys. Lett. 51 (23) (1987) 1885–1886, http://dx.doi.org/10.1063/1.98500.
[4] Y. Li, Y. Zheng, Q. Wang, C.C. Zhang, Synthesis of luminescent YVO4:Eu3+ submicrometer crystals through hydrogels as directing agents, Mater. Chem. Phys. 135 (2) (2012) 451–456.
[5] P. Dorenbos, The 5d level positions of the trivalent lanthanides in inorganic compounds, J. Lumin. 91 (3) (2000) 155–176.
[6] R. Yongfeng, Z. Shouchao, L. Shuhua, L. Guanghui, L. Wenrun, L. Jingwang, Growth and spectrum properties of Ce: YVO4 single crystal, J. Rare Earths 25 (2007) 122–124.
[7] A. Jayaraman, G. Kourouklis, G. Espinosa, A. Cooper, L. Van Uitert, A high-pressure Raman study of yttrium vanadate (YVO4) and the pressure-induced transition from the zircon-type to the scheelite-type structure, J. Phys. Chem. Solids 48 (8) (1987) 755–759.
[8] V. Panchal, D. Errandonea, A. Segura, P. Rodriguez-Hernandez, A. Muñoz, S. Lopez-Moreno, M. Bettinelli, The electronic structure of zircon-type orthovanadates: Effects of high-pressure and cation substitution, J. Appl. Phys. 110 (4) (2011) 043723.
[9] H. Rajendra, C. Pandurangappa, Luminescence investigation of a cerium-doped yttrium vanadate phosphor, Luminescence 35 (3) (2020) 341–346.
[10] Y. Wang, S. Wang, Z. Wu, W. Li, Y. Ruan, Photoluminescence properties of ce and eu co-doped YVO4 crystals, J. Alloys Compd. 551 (2013) 262–266.
[11] S. Wang, P. Wang, Y. Ruan, Y. Wang, S. Zhang, Photoluminescence characteristics and energy transfer phenomena in Ce^{3+}-doped YVO_4 single crystal, Sci. Eng. Compos. Mater. 28 (1) (2021) 205–214.
[12] Z. Huang, J. Feng, W. Pan, Theoretical investigations of the physical properties of zircon-type YVO4, J. Solid State Chem. 185 (2012) 42–48.
[13] X. Wang, I. Loa, K. Syassen, M. Hanfland, B. Ferrand, Structural properties of the zircon-and scheelite-type phases of YVO 4 at high pressure, Phys. Rev. B 70 (6) (2004) 064109.
[14] P. Borlido, J. Schmidt, A.W. Huran, F. Tran, M.A. Marques, S. Botti, Exchange-correlation functionals for band gaps of solids: benchmark, reparametrization and machine learning, Npj Comput. Mater. 6 (1) (2020) 1–17.

[15] P. Scharoch, M. Winiarski, An efficient method of DFT/LDA band-gap correction, Comput. Phys. Comm. 184 (12) (2013) 2680–2683.
[16] J.P. Perdew, M. Levy, Physical content of the exact Kohn-Sham orbital energies: band gaps and derivative discontinuities, Phys. Rev. Lett. 51 (20) (1983) 1884.
[17] L.J. Sham, M. Schlüter, Density-functional theory of the energy gap, Phys. Rev. Lett. 51 (20) (1983) 1888.
[18] L. Hedin, New method for calculating the one-particle Green's function with application to the electron-gas problem, Phys. Rev. 139 (1965) A796–A823.
[19] F. Aryasetiawan, O. Gunnarsson, The GW method, Rep. Progr. Phys. 61 (3) (1998) 237.
[20] G. Kotliar, S.Y. Savrasov, K. Haule, V.S. Oudovenko, O. Parcollet, C.A. Marianetti, Electronic structure calculations with dynamical mean-field theory, Rev. Modern Phys. 78 (2006) 865–951.
[21] R. Gillen, S.J. Clark, J. Robertson, Nature of the electronic band gap in lanthanide oxides, Phys. Rev. B 87 (12) (2013) 125116.
[22] M. Cococcioni, S. de Gironcoli, Linear response approach to the calculation of the effective interaction parameters in the LDA + U method, Phys. Rev. B 71 (2005) 035105.
[23] S.A. Tolba, K.M. Gameel, B.A. Ali, H.A. Almossalami, N.K. Allam, The DFT + U: Approaches, accuracy, and applications, Density Funct. Calc.-Recent Prog. Theory Appl. (2018) 3–30.
[24] A.V. Krukau, O.A. Vydrov, A.F. Izmaylov, G.E. Scuseria, Influence of the exchange screening parameter on the performance of screened hybrid functionals, J. Chem. Phys. 125 (22) (2006) 224106.
[25] G. Kresse, J. Furthmüller, Efficiency of ab-initio total energy calculations for metals and semiconductors using a plane-wave basis set, Comput. Mater. Sci. 6 (1) (1996) 15–50.
[26] P.E. Blöchl, Projector augmented-wave method, Phys. Rev. B 50 (24) (1994) 17953.
[27] J.P. Perdew, K. Burke, M. Ernzerhof, Generalized gradient approximation made simple, Phys. Rev. Lett. 77 (1996) 3865–3868.
[28] R. Armiento, A.E. Mattsson, Functional designed to include surface effects in self-consistent density functional theory, Phys. Rev. B 72 (2005) 085108.
[29] G.I. Csonka, J.P. Perdew, A. Ruzsinszky, P.H.T. Philipsen, S. Lebègue, J. Paier, O.A. Vydrov, J.G. Ángyán, Assessing the performance of recent density functionals for bulk solids, Phys. Rev. B 79 (2009) 155107.
[30] H.J. Monkhorst, J.D. Pack, Special points for Brillouin-zone integrations, Phys. Rev. B 13 (12) (1976) 5188.
[31] M.A.L. Marques, J. Vidal, M.J.T. Oliveira, L. Reining, S. Botti, Density-based mixing parameter for hybrid functionals, Phys. Rev. B 83 (2011) 035119.
[32] J.P. Perdew, M. Ernzerhof, K. Burke, Rationale for mixing exact exchange with density functional approximations, J. Chem. Phys. 105 (22) (1996) 9982–9985, http://dx.doi.org/10.1063/1.472933.
[33] C.G. Van de Walle, J. Neugebauer, First-principles calculations for defects and impurities: Applications to III-nitrides, J. Appl. Phys. 95 (8) (2004) 3851–3879.
[34] B.C. Chakoumakos, M.M. Abraham, L.A. Boatner, Crystal structure refinements of zircon-type MVO4 (M=Sc, Y, Ce, Pr, Nd, Tb, Ho, Er, Tm, Yb, Lu), J. Solid State Chem. 109 (1) (1994) 197–202.
[35] S. G., K. V., V. G., Optical properties of orthovanadates, and periodates studied from first principles theory, Mater. Chem. Phys. 163 (2015) 376–386.
[36] P. Deák, M. Lorke, B. Aradi, T. Frauenheim, Optimized hybrid functionals for defect calculations in semiconductors, J. Appl. Phys. 126 (13) (2019) 130901.
[37] C. Zhi-Peng, W. Yu-Hua, Z. Jia-Chi, A novel yellow emitting phosphor Dy^{3+}, Bi^{3+} co-doped YVO_4 potentially for white light emitting diodes, Chin. Phys. B 19 (5) (2010) 057803.
[38] M.R. Dolgos, A.M. Paraskos, M.W. Stoltzfus, S.C. Yarnell, P.M. Woodward, The electronic structures of vanadate salts: cation substitution as a tool for band gap manipulation, J. Solid State Chem. 182 (7) (2009) 1964–1971.
[39] H.-S. Shi, G. Zhang, H.-Y. Shen, Measurement of principal refractive indices and the thermal refractive index coefficients of yttrium vanadate, J. Synth. Cryst. 30 (1) (2001) 85–88.
[40] M.V. Jacob, J. Mazierska, J. Krupka, Dielectric properties of yttrium vanadate crystals from 15 K to 295 K, J. Electroceram. 15 (3) (2005) 237–241.
[41] M. Soharab, I. Bhaumik, R. Bhatt, A. Saxena, A.K. Karnal, P.K. Gupta, Effect of Yb^{3+} doping on the refractive index and thermo-optic coefficient of YVO4 single crystals, Appl. Opt. 56 (6) (2017) 1682–1688.

Paper IV

Amin Mirzai, Aylin Ahadi

First-principle study of luminescence & electronic properties of Ce-doped Y_2SiO_5

The Journal of Chemical Physics

Accepted – available online: 28-10-2023

DOI: 10.1063/5.0165432

First-principles study of luminescence & electronic properties of Ce-doped Y_2SiO_5*

Amin Mirzai† and Aylin Ahadi
Lund University, Department of Mechanical Engineering Sciences, Division of Mechanics, Materials, and Component Design, P.O. Box 118, SE-221 00 Lund, Sweden

The transition of energy from the 4f to the 5d state is a fundamental element driving various applications, such as phosphors and optoelectronic devices. The positioning of the 4f ground states and the 5d excited states significantly influences this energy shift. In our research, we delve into the placement of these states utilizing a hybrid DFT combined with spin-orbit coupling (SOC) via the supercell method. Additionally, we scrutinize the transition energy, applying the constrained density functional theory (cDFT) approach in conjunction with the ΔSCF method. Our study illustrates that the synergy of cDFT and SOC generates a discrepancy of about 2% for Ce1 and 4% for Ce2 when comparing the calculated results to experimental data. Moreover, We have determined the positions of the 4f ground states to be 2.73 eV above the Valence Band Maximum (VBM) for Ce1 and 2.70 eV for Ce2. We also note a tight correlation between the 5d levels identified in the experimental data and the theoretical outcomes derived from wave function calculations at the CASPT2 (Complete Active Space with Second-order Perturbation Theory) accuracy level.

I. INTRODUCTION

The performance of optoelectronic devices and phosphors hinges on the optical and electronic attributes of both host materials and activators. Numerous applications, including displays [1], white LEDs [2], depend on the effectiveness of these phosphors and activators. Lanthanides (Ln) stand out as preferred activators, owing to their distinctive electronic structure and the transition from $4f$ to $5d$ levels. This specific transition generates a notable yet broad peak in both absorption and emission spectra. The form and intensity of these peaks heavily rely on the host lattice, affecting the energy difference between the Ln dopants' lowest $4f^n$ level and the first $4f^{n-1}5d$ level, as reported by Qin et al. [3] Consequently, the precise positioning of the Ln $4f$ and $5d$ levels is crucial, influencing intensity, energy transitions, Ln valence, luminescence, and charge carrier trapping properties [4, 5]. This underlines the importance of accurately understanding the $4f$ and $5d$ levels' locations in Ln ions for the creation of efficient optoelectronic devices and phosphors.

A prominent optical material is $Y2SiO_5$ (YSO) doped with Rare-Earth (RE) ions, particularly Ce-doped YSO, recognized for its scintillation properties. Its luminescence has been thoroughly probed, both experimentally [6, 7] and theoretically[8]. However, previous theoretical investigations into Ce-doped YSO using the *ab initio* model potentials (AIMPs) method encounter limitations due to their dependence on empirical data and the accompanying computational expenses [9, 10]. This reliance restricts the AIMP model's adaptability to various host materials and RE ions. Given YSO doped with RE's significant potential as an optical material, it is essential to delve into fresh theoretical avenues. Such strategies must efficiently and precisely discern luminescent characteristics, ensuring their broad material applicability without compromise.

RE ions in inorganic compounds are typically excited from $4f \rightarrow 5d$ using either quantum chemistry methods or solid-state methods. Quantum chemical techniques, such as coupled-cluster (CC) [11] and complete active space self-consistent field (CASSCF) [12], are highly accurate but are often used for finite-sized solids and molecules due to their computational cost. Time-dependent density functional theory (TDDFT [13]), despite its success in closed-shell molecules, is still not well-tested for larger molecules and solids, especially those with open shells [14]. Furthermore, TDDFT has only been applied to systems with defects using clusters to approximate infinite solids [14]. Many-body perturbation theory (MBPT) based on GW approximation is another solid-state technique that corrects the Kohn-Sham eigenvalues of a traditional DFT with quasi-particle corrections [15]. GW + BSE correction of MBPT is currently the best approach for studying the optical properties of solids [16]. However, its application is limited to small molecules and high-symmetry solids due to its computational cost. Therefore, running calculations for defect studies using supercell sizes is not feasible [17]. Additionally, it is not possible to calculate forces on atoms in solids using this approach.

To address the limitations of DFT for calculating excitation processes and to overcome the limitations that are offered by the aforementioned excitation approaches, we employ the constrained DFT (cDFT) [18, 19]. This method is an adaptation of generic DFT that partially mitigates its shortcomings, enabling the calculation of excitation processes [18]. Although cDFT does not offer excitonic effects by itself, it has proven to be an effective approach for simulating neutral excitation in molecular and solid systems [17, 20]. It has also been used in high-throughput studies of Ln scintillators, as demonstrated in the works of Canning et al. [19] and Jia et al. [16, 17].

* Corresponding author
† Department of Mechanical Engineering Sciences, Division of Mechanics, Materials, and Component Design, Lund University P.O. Box 118, SE-221 00, Sweden; amin.mirzai@mek.lth.se

In this paper, we aim to determine the energy transitions of the Ce^{3+} ion doped in YSO host through a complete *ab initio* technique. To enhance the accuracy of our calculations, we include the Heyd–Scuseria–Ernzerhof (HSE [21]) functional with the Spin-Orbit Coupling (SOC) effect. It has been demonstrated that electronic property predictions with the screened hybrid functional can be comparable to $GW_0@LDA+U$ calculations [22]. Additionally, we construct a supercell of 1x2x1 relative to the host unit cell to minimize impurity-impurity interactions. The relative energy levels of the 4f and 5d states of Ce^{3+} are identified through a combination of cDFT and hybrid functional calculations. Once the energy levels are determined, we employ the ΔSCF method to obtain the 4f→5d transition in the Ce^{3+} ion.

II. THEORY & METHOD

The initial atomic positions used in this study were obtained from our previous work [23], in which we characterized the two distinct spectroscopic sites present in YSO. These sites, known as site1 (Y/Ce1) and site2 (Y/Ce2), are each surrounded by 7 and 6 oxygen atoms (Figure 1), respectively. These sites with the aforementioned coordination number (CN) belong to X2-YSO crystallographic form, the other form being X1-YSO has CN numbers of 9 and 7 [23]. The X2-YSO has a stronger luminescent intensity in comparison with X1-phase, and thus it is more crucial for practical application and luminescent efficiency [24]. The calculations are carried out by employing pseudopotential plane-wave DFT methodology as implemented in the Vienna Ab initio Software Package (VASP) [25]. The Ce: $5d^14f^1$, Y: $4s^24p^64d^15s^2$, Si: $3s^23p^2$, and O:$2s^22p^4$ electrons are treated as valence electrons, whereas the core electrons and electron-ion interactions are determined using the projected augmented wave (PAW) method [26]. The contribution due to exchange and correlation is expressed by the generalized gradient approximation (GGA) theory as described by Perdew-Burke-Ernzerhof (PBE) [27], and the partial occupancy of orbitals was determined using the tetrahedron method with Blöchl corrections [28]. The cut-off energy was set to, 520 eV, while the k-point set for the unit cell was selected to be 4×8×6. The convergence threshold was set to $1\times\ 10^{-8}$ eV, and the force criterion for geometry optimization was 0.00001 eV/Å.

In order to tune the HSE parameters a series of Gamma-point only calculations were performed. These calculations are based on the PBE pre-optimized unit cell of the pure system. First, the percentage of exact exchange α, according to Equation 1, was varied to reach the optimal level, which in this case means obtaining a band gap value similar to the experimental band gap. Once, the approximate percentage of exact exchange is set, the screening parameter ω is tuned. In the end, an HSE calculation with sufficiently dense k-mesh was chosen to validate the band gap result and tuned parameters. The subsequent HSE calculations are conducted based on the tuned parameters.

$$E_{xc}^{HSE} = \alpha E_x^{HF,SR}(\omega) + (1-\alpha)E_x^{PBE,SR}(\omega) + E_x^{PBE,LR}(\omega) + E_c^{PBE} \quad (1)$$

As Figure 2 shows the SOC plays an important role in the identification of the energy levels especially if we are dealing with heavy elements such as Ln, due to this fact we have included the SOC effect. The SOC effect is documented here using the implemented method in VASP. The SOC is most effective in the vicinity of the core region, so the implementation of SOC in VASP is only considered within the PAW spheres [30]. So, the contribution of SOC is included using the following perturbed Hamiltonian (zeroth-order-regular approximation):

$$\tilde{H}_{SO} = \sum_{ij} |p_i\rangle \langle\phi_i|H_{SO}|\phi_j\rangle \langle p_j|, \quad (2)$$

and the H_{SO} is given below according to the zeroth-order-regular approximation:

$$H_{SO}^{\alpha\beta} = \frac{\hbar^2}{(2m_ec)^2}\frac{K(r)}{r}\frac{dV(r)}{dr}\overrightarrow{\sigma}^{\alpha\beta}\overrightarrow{L}. \quad (3)$$

The α and β denote spin up and spin down, and the angular momentum operators $\overrightarrow{L}$ are defined as $\overrightarrow{L} = \overrightarrow{r} \times \overrightarrow{p}$. The $V(r)$ is the spherical part of the effective all electronic potential within the PAW sphere, and its relation with $K(r)$ is

$$K(r) = (1 - \frac{V(r)}{2m_ec^2})^{-2}, \quad (4)$$

where m_e is the effective mass of the particle and c is the speed of light. Besides, in VASP inclusion of SOC effects coincides with the inclusion of relativistic effects. The core electrons are treated fully relativistic and the effect for valence electrons is considered through scalar relativistic approximation [31].

A. Ground State

To simulate a dopant in a periodic lattice, we use the supercell approach with periodic boundary conditions. We construct a 1×2×1 supercell based on the pre-optimized unit cell of the host crystal and then replace one of the Y^{3+} sites by a Ce^{3+} ion. Such supercell contains 128 atoms, and a Ce^{3+} doping concentration of 3.125%. This doping concentration of Ce^{3+} is usually higher than the experiments. However, the distance between these Ce^{3+} ions in the periodic cells are greater than 12 Å, which is sufficiently large to reduce the possibility of interaction between impurities. We then relax the atomic positions while keeping the cell dimensions fixed. Once the supercell is relaxed, we perform a ground-state calculation to determine the position of the Ce-*4f*

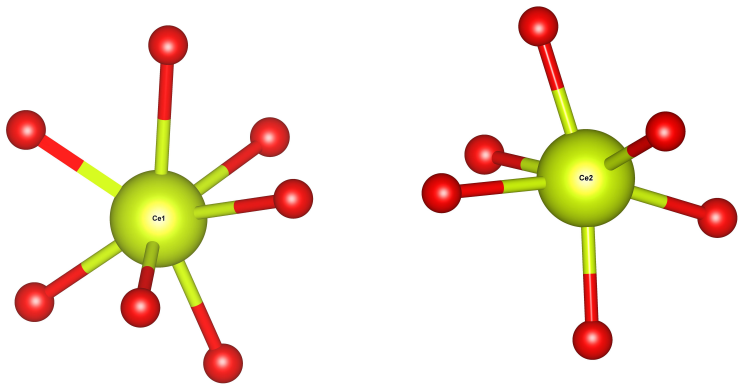

FIG. 1. Schematic view of impurity sites in X2-YSO. Site1 with coordination number 7, and site2 with coordination number 6.

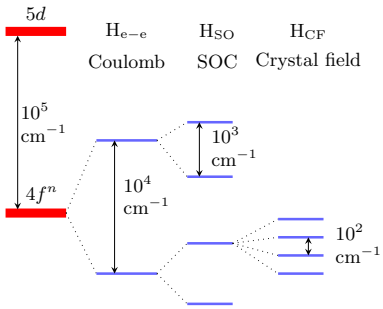

FIG. 2. The source and magnitude of the energy level splittings in $4f^n \rightarrow 5d$ configuration. The figure is adapted from reference [29].

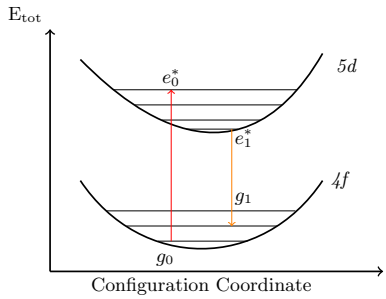

FIG. 3. Configuration coordinate diagram

level relative to the valence band maximum (VBM) of the host material. The occupied 4f level is typically very localized and atomic in nature and has almost no bandwidth, so the VBM-4f gap is well-defined. Nevertheless, a modified HSE calculation was performed to improve the positioning of levels. The cut-off energy is kept at 520 eV, and the conjugate gradient algorithm is used to relax the system. The sampling of the Brillouin zone was done by implementing the Γ-point only kpoint grid. A convergence threshold of 1×10^{-6} eV was used to reach self-consistency.

B. Excited State

Two distinct methods are employed for calculating excited states. The first is the constrained occupancy approach. This method begins by calculating the ground states. The energy eigenvalues are then analyzed to identify levels with 4f and 5d character. To mimic the effect of a photon removing an electron from valence 4f and transferring it to 5d, the 4f levels are manually emptied, and the lowest-lying 5d-like band is filled. Kohn-Sham (KS) eigenvalues and total energies for ground and excited states are subsequently determined. Since KS eigenvalues cannot replace optical transition levels [32, 33], only the difference between total energies (ΔSCF) of these two states is considered for energy transition. Absorption energy is obtained using ΔSCF, represented as E_{abs} = e_0^* - g_0 in Figure 3. Later, the constraint on occupancy is lifted, allowing the perturbed lattice to relax due to a change in its electronic configuration. This relaxation pertains only to atomic positions, leaving the lattice vectors unaltered. This state, depicted in Figure 3, is denoted as g_1, and the emission energy is calculated as $E_{ems} = e_1^*$ - g_1 . The Stokes shift is determined by subtracting the absorption energy from the emission energy.

In the latter approach, a relaxed Ce-doped 1x2x1 supercell, acquired during ground state calculations, un-

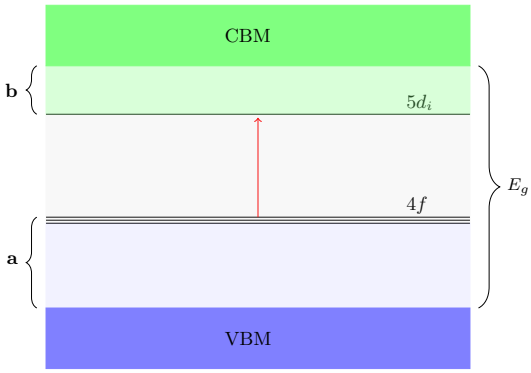

FIG. 4. The transition energy: The host valence band maximum of the corresponding cell is subtracted from occupied 4f eigenvalue ($\mathbf{a} = 4f - VBM_{host}$). Then 5d eigenvalues that are obtained from +1-charged supercell calculation are subtracted from the host conduction band minimum of the corresponding cell ($\mathbf{b} = CBM_{host} - 5d$). Lastly, the two values are subtracted from the calculated host band gap, E_g=7.4013 eV. $4f \rightarrow 5d = E_g$ - **a** - **b**.

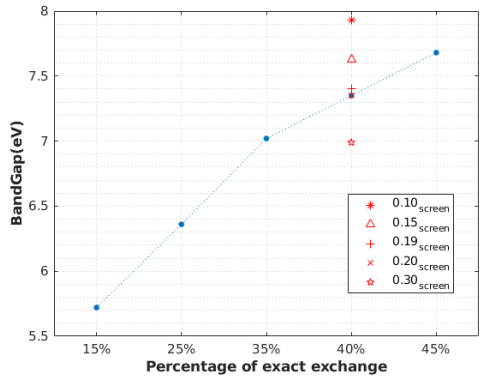

FIG. 5. Tuning of HSE parameters based on the experimental band gap. The data points are extracted from Gamma-point only calculations. As can be seen in the figure, the experimental band gap gets reproduced at $\alpha = 40\%$ exact exchange and $\omega = 0.19$ screening.

dergoes two separate HSE calculations for each Ce site. Initially, a neutral HSE calculation is conducted to determine the ground state location of 4f states when a 4f level is occupied. Additionally, a modified HSE functional relaxes a mono-positively charged supercell structure of Ce-doped YSO. This process, which adheres to the Frank-Condon principle [34], reveals the electronic structure of excited states at the conduction level and ascertains the location of low-lying 5d states. The next step involves obtaining the 4f $\rightarrow$ 5d transition energies by analyzing the 4f eigenvalues from a neutral calculation and subtracting them from the valence band edge of the corresponding host cell, expressed as **a** = 4f - VBM_{host}. Additionally, the 5d eigenvalues of the Ce impurity are identified by evaluating the mono-positively charged calculation. The crystal field effect eliminates the degeneracy of the 5d levels, as depicted in Figure 7 (b & d), allowing the determination 4f to $5d_i$ where i is the indices for different 5d orbital orientations.

Before determining the transition energies, the $5d_i$ eigenvalues are subtracted from the corresponding host conduction band minimum (CBM), expressed as **b** = CBM_{host} - $5d_i$. Finally, the transition energies between 4f$\rightarrow 5d_i$ are computed by subtracting **a** and **b** from the experimental or modified band gap energy of the host in its primitive cell, expressed as $4f \rightarrow 5d_i = E_g$ - **a** - **b**. This entire process is visually outlined in Figure 4.

As we mentioned earlier the KS eigenvalues are not considered true states of the system, however, since we only consider their energy difference and we subtract these energy differences from the KS band gap, one should end up with a true value that can be considered as true transition energy between 4f & 5d states.

TABLE I. Band gap of C2/c Y_2SiO_5. *This study:* *.

Material	Method	Band gap (eV)
Y_2SiO_5	Exp.	7.4 [35]
Y_2SiO_5	Exp.	7.4 [36]
Y_2SiO_5	PBE	4.82 [10]
Y_2SiO_5	PBE*	4.819
Y_2SiO_5	mBJ	6.14 [10]
Y_2SiO_5	HSE*	7.40

III. RESULTS & DISCUSSION

In the initial stage of our study, we diligently fine-tuned the parameters of the HSE functional to match the experimental band gap, which are tabulated in Table I. Our parameter optimization process is presented in Figure 5, which reveals that the optimal value for the fraction of HF exact exchange α is 0.40, while the screening value μ is 0.19. Notably, these values were derived from a Gamma-point only HSE calculation, and we subsequently validated them using a kpoint mesh of 1×3×2.

The information provided in Table II illustrates the variation in bond lengths at site1 and site2. This change in bond length during excitation can be understood through the Franck-Condon Principle [37, 38], which explains that during an electronic transition such as ionization, the nuclear arrangement of the molecule initially remains largely unchanged due to the nuclei's significantly greater mass compared to electrons. This results in the electronic transition happening quicker than the nuclei's response. However, post-transition, the nucleus has to realign itself to the new electronic configuration, a process that involves vibration, and a rhythmic motion of the

atoms in the molecule relative to each other. This motion can bring about a change in the bond length. Moreover,

TABLE II. Bond lengths (in Å) of Ce^{3+} at site1 & site2 in ground and excited states.

Bond length	site1 - gr.	site1-exc.	site2-gr.	site2-exc.
Ce-O_1	2.32	2.29	2.297	2.219
Ce-O_2	2.49	2.46	2.411	2.368
Ce-O_3	2.71	2.70	2.373	2.307
Ce-O_4	2.38	2.32	2.390	2.335
Ce-O_5	2.49	2.50	2.385	2.326
Ce-O_6	2.44	2.40	2.391	2.337
Ce-O_7	2.45	2.28		

when a transition from the 4f to the 5d states occurs, electrons are moved from the inner 4f shell to the more external 5d shell in an atom's electronic configuration. In such a scenario, bond length generally decreases. The underpinning reason for this decrease is the alterations in the orbital overlap's nature and magnitude, along with the differences in shielding and penetration abilities between 4f and 5d electrons [39]. This explanation supports the data in Table II, where the bond length has almost decreased in all cases in both sites except for the Ce-O_5 at the site1.

Figure 6 displays the projected density states of pure YSO using the modified HSE functional, which results in a band gap value that is identical to experimental measurements. The dominant states at the VBM are O_p orbitals, whereas Y_d orbitals are the main constituents of the CBM.

In the lower section of Figure 6, we observe the effects of SOC on the electronic structure of YSO. The band gap calculated without SOC yields a value of 7.40130, while the inclusion of the SOC effect slightly enlarges the band gap to 7.42130. This difference corresponds to an increase of 20 meV. Notwithstanding the small alteration in the band gap energy, the constitution of the VBM and CBM remains essentially invariant, with a minor shift ascribed to SOC effects. This limited shift is predominantly attributable to the constituent elements of the system. Neither silicon nor oxygen, being lightweight elements, produce a significant SOC effect. Concurrently, the heaviest atom in the system, Yttrium (Y), doesn't have a noticeable impact on the SOC effect since it is still categorized as a light element according to Russell-Saunders coupling theory, where it states elements with Z < 40 is considered as light [40]. Consequently, the cumulative effect of SOC on the physical properties of pure YSO is deemed insignificant.

Table III presents the calculated absorption and emission energies, as well as the Stokes shift. The calculations were performed on a YSO standard unit cell with 64 atoms, as it has been demonstrated by Jia et al. [41] that the energy difference between cells with 64 atoms and 128 atoms is negligible. Even though the compound studied by Jia et al. is Lu_2SiO_5 (LSO), the structure

TABLE III. Calculated total energies, absorption, and emission energies of $Ce : Y_2SiO_5$ based on cDFT approach.

	Site1 (eV)	Site2 (eV)
E_{g_0}	-746.058	-745.744
$E_{e_0^*}$	-741.929	-741.868
E_{g_1}	-746.058	-745.744
$E_{e_1^*}$	-742.121	-742.346
E_{abs}	4.130	3.876
E_{abs}[6]	3.41	3.30
E_{ems}	3.938	3.398
E_{ems}[6]	3.12	2.73
Stokes shift	0.191	0.478

of the cell is identical (C2/c). Thus, we opted to use the 64 atoms cell for the cDFT approach as it is a more cost-effective option.

The results show larger calculated values for absorption and emission at both sites, compared to the experimental values. The discrepancy between the calculated and experimental values is approximately 0.7 eV for both energies at Ce1, while at Ce2, the difference is slightly smaller, around 0.5 eV. A possible reason for this mismatch is the lack of consideration of SOC in the calculations. This connection can be inferred easier by referring to Figure 2, which shows that the magnitude of the SOC effect is on the order of 1000 cm^{-1} (0.12 eV), comparable to the observed discrepancy.

It is worth noting that SOC is a relativistic correction that affects heavier atoms more significantly, and since Ce has unpaired electrons, the SOC effect on this atom is likely to be more pronounced. Hence, it is reasonable to focus on the SOC correction that corresponds to Ce, represented by E_{soc}.

In VASP, E_{soc} is defined as the energy difference between two collinear spin configurations, where the spins are oriented parallel and anti-parallel to the quantization axis. The quantization axis is defined by the direction of the external magnetic field or the preferred orientation of the magnetic moments in the system. Thus, by calculating E_{soc}, we can account for the effect of SOC on the electronic and magnetic properties of the system, and it is defined as follows:

$$E_{soc} = \sum_{ij} E_{soc}^{ij}, \tag{5}$$

E_{soc}^{ij} can be expanded as,

$$E_{soc}^{ij} = \delta_{R_i R_j}\delta_{l_i l_j} \sum_{nk} \omega_k f_{nk} \sum_{\alpha\beta} \langle \tilde{\psi}_{nk}^{\alpha} | \tilde{p}_i \rangle \langle \phi_i | H_{soc}^{\alpha\beta} | \phi_j \rangle \langle \tilde{p}_j | \tilde{\psi}_{nk}^{\beta} \rangle , \tag{6}$$

where, ω_k is k-point weights, f_{nk} is the Fermi weights, ϕ_i are the partial waves of an atom centered at R_i, $\tilde{\psi}_{nk}^{\alpha}$ is the α Spinor-component of the pseudo-orbital where its band-index is n and Bloch-vector is k [30].

We observed two distinct values of E_{soc} for the absorption and emission processes. So, we applied them separately to account for the differences. The calculated SOC effects for Ce1 during absorption and emission processes are E_{soc}=**-0.65396** and E_{soc}=**-0.77685** eV, respectively. Similarly, the E_{soc} for Ce2 during absorption and emission processes are E_{soc}=**-0.65397** and E_{soc}=**-0.77850** eV, respectively. The SOC-corrected values of absorption and emission energy are listed in Table IV, and they are obtained by adding the corresponding E_{soc} energy to the absorption and emission energies presented in Table III.

The corrected values exhibit an excellent agreement between experimental and calculated results, particularly at Ce1. For Ce1, the discrepancy for both absorption and emission is around 0.05 eV higher than the experiment, whereas for Ce2, we observe a larger difference at the order of 0.10 eV lower than the experiment. It is worth mentioning that these comparisons are made with one experiment only, and if we compare the calculated absorption energy with the average of experiments listed in Table V for Ce1, E_g=3.48 eV, then the discrepancy becomes almost zero. However, this is not the case for Ce2, as the average absorption energy for experiments at this site is 3.31 eV, while the calculated value is 3.22 eV, indicating a difference of 0.09 eV.

TABLE IV. The SOC-corrected values of absorption and emission energies. The updated values are achieved by adding E_{soc} to the corresponding energies in Table III. *This study:* *, Exp. [6].

	Site1 (eV)	Site2 (eV)
E_{abs}*	3.47	3.22
E_{abs}[6]	3.41	3.30
E_{ems}*	3.16	2.62
E_{ems}[6]	3.12	2.73
Stokes shift	0.314	0.602

Figure 7, shows the Density of States (DOS) for the Ce-doped YSO. The main composition of the VBM and the CBM is constituted of O_p and Y_d orbitals, respectively, a configuration similar to that of pure YSO. The Partial DOS (PDOS) at ground state for Ce-doped YSO is depicted in subfigures (a) and (b) of Figure 7.

The location of the 4f states within the band gap, as indicated by Zhou et al. [10], contrasts with our observations. Zhou et al. reported the 4f states to be 4.78 eV away from the VBM, a different finding compared to our analysis. However, the current results align closely with the findings of Ning et al. [42], who utilized the AIMPs approach on Ce: LSO. Their research identified the 4f - VBM gap as 2.81 and 3.07 for Ce1 and Ce2, respectively. In a related study, Vedda et al. [43] conducted experiments on Ce: LSO, ascertaining the 4f - VBM gap to be within the range of 2.6 - 2.9 eV. Despite the difference in the chemical compound of the host, the host still shares similar crystal (C2/c) and site (C1) symmetries

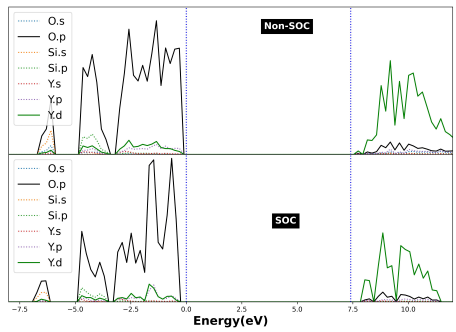

FIG. 6. PDOS of pure YSO with and without SOC.

for the Ce dopant. These consistent findings across different studies suggest that the VBM-4f gap in Ce: YSO aligns well with previous studies.

For more comprehensive comparison, the Dorenbos model can be employed. [4, 44]. The Dorenbos relation is an empirical model that is widely used to estimate the energy of 4f of trivalent and divalent Ln ions in a given host lattice based on the peak position of the lowest 4f→5d level of at least one of the Ln ions in that host. Based on this empirical approach and with the use of experimental data for Ce, and Pr-doped YSO and LSO, Kolk together with Dorenbos et al. have produced the probable location of 4f and the lowest lying 5d levels inside the band gap for all the Ln in YSO [45]. The estimated value that they have obtained for the 4f - VBM gap is around 3.53 eV. It should be added that they have not identified this value to a specific site, Ce1 or Ce2, as they mention their data for the photocurrent experiment do not show any doublet structure [45]. Lastly, the inclusion of SOC has shifted the 4f ground states by 0.20 eV at both sites. This has reduced the 4f-VBM gap down at Ce1 to 2.73 eV, and to 2.70 eV at Ce2. With this shift, the agreement with the experimental work of Vedda et al. has improved [43].

Figure 7(c & d) illustrates the mono-positively charged state of Ce-doped YSO. At this phase, all atomic positions are held consistent with the neutral Ce-doped YSO to generate an excitonic effect. This effect occurs between the hole at the VBM and an electron in one of Ce's lower 5d states, adhering to the Franck-Condon principle. These low 5d states, close to the CBM, display notable splitting due to the crystal field (CF), marked in red. A comparison of the red peaks at Ce1 and Ce2 highlights more prominent peaks or splittings at Ce2 in both SOC and non-SOC scenarios. This observation is attributed to the smaller size of Ce2 compared to Ce1. Therefore, the CF splitting is stronger at Ce2 than Ce1, which agrees with previous studies conducted using DFT+CASPT2 [8, 10].

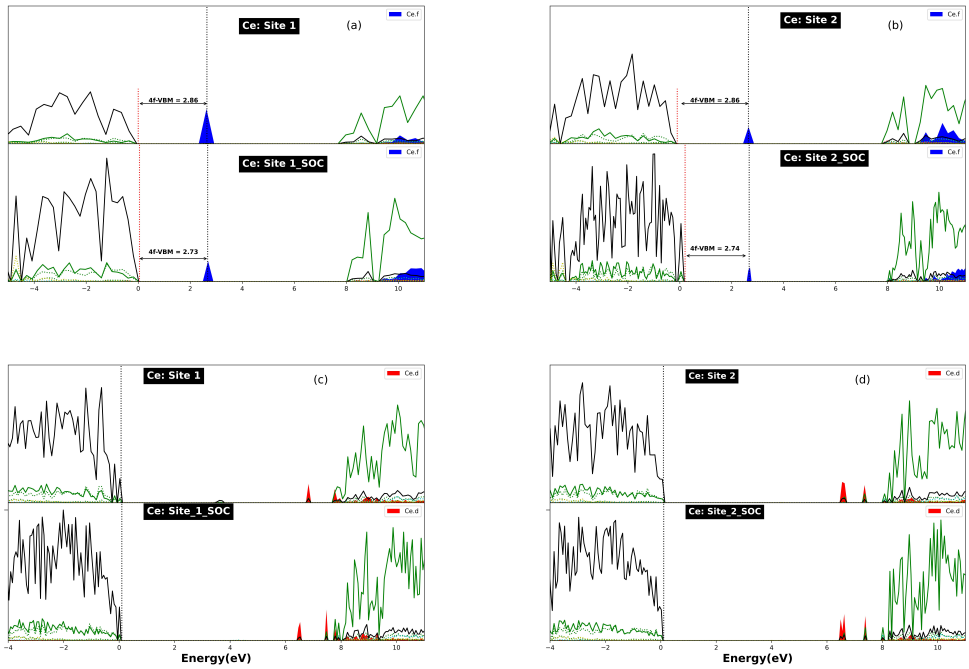

FIG. 7. Orbital projected DOS of Ce-doped YSO, at Ce1 and Ce2 in a 1x2x1 supercell. The blue-filled states indicate the 4f orbitals of the Ce^{3+} while they are occupied: (a) & (b). When 4f states are unoccupied, we can observe the 5d states in the band gap that are filled in red. The black dotted lines show the position of the Fermi level: (c) & (d).

The significant impact of SOC is evident in Figure 7 c & d, particularly in the lower section where the $5d_i$ levels undergo a downward shift towards the VBM at both sites. This shift measures 0.38 eV at Ce1 and 0.04 eV at Ce2. Interestingly, the direction of the shift for the remaining levels is not uniform at both sites. This shift, combined with the presence of SOC, results in four out of the five lowest peaks falling within the band gap. A clearer illustration of the gap between these peaks and their shifts due to SOC incorporation is provided in Figure 8. Here, the $5d_{2-i}$ levels are marked based on their relative positions to $5d_1$.

Table V outlines the transition energies from 4f to 5d in two unique sites of the YSO. Details about the calculation and methodology used for determining these energy transitions are elaborated in section II.

The table's sixth row reveals the computed value of the non-SOC but HSE functional of the supercell structure. The initial transition value at Ce1 closely aligns with the experimental value, with calculated values showing a minor difference from the experimental average for the lowest lying 5d: 0.03 at Ce1 and 0.13 at Ce2. This indicates a more precise definition of the lowest lying 5d level in both experiment and AIMPs calculation at both impurity sites.

However, the disparity between the experimental and calculated values grows for the other $5d_i$ levels, notably for the last two, $5d_4$ and $5d_5$. Here, the absence of clear, sharp peaks and the low intensity, as observed in Figure 8, complicate the measurement process. This difficulty likely accounts for the data deficiency for these two levels, precluding any comparison.

Incorporating SOC has uniformly reduced the energy of $5d_i$ levels at both sites. At Ce1, the energy shift is approximately 1600 cm^{-1} (0.2 eV), and at Ce2, it is about 1000 cm^{-1} (0.1 eV). These observations align with Wen et al.'s findings for Ce: YSO, where the shift was around 0.12 eV and 0.1 eV for Ce1 and Ce2, respectively [8]. Moreover, Ning et al. reported a similar 1000 cm^{-1} shift for both Ce: LSO sites [42]. However, a distinctive difference is noted in this study: while previous works reported an increase in 5d levels with SOC, a decline is observed here.

Overall, it is hard to state the SOC has uniformly improved all the levels as we observed in the result of cDFT approach. However, it has certainly improved the agree-

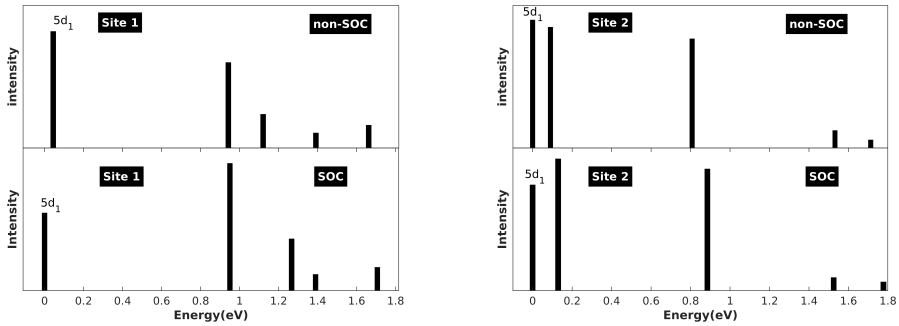

FIG. 8. Location of $5d_i$ levels with respect to lowest lying $5d_1$ of the Ce atom at Ce1 & Ce2 with and without SOC.

ment with the experimental average at $5d_2$ Ce1, and at $5d_1$, $5d_3$ Ce2.

IV. CONCLUSION

In this study, we investigated the electronic and optical properties of Ce-doped YSO, with a focus on the 4f→5d transition. We used a band gap-modified HSE functional with Gamma-point only and found that the results were in good agreement with experimental data, particularly when the SOC effect was included. Although the effect of SOC was not consistent for all $5d_i$ levels, it improved the transition energies overall, especially when using the cDFT approach. We observed a consistent overshoot in the cDFT results compared to experimental data, but this deviation was reduced with the inclusion of SOC. Specifically, the deviations between calculated values and experiments for absorption and emission were 1.75% & 1.28% at Ce1, and 2.42% and 4.02% at Ce2, respectively.

Computational time often hinders SOC+HSE calculations. Despite this, our research reveals that using the Gamma-point calculations yield results accurate enough for comparison with experimental data. Moreover, our study was conducted on a sufficiently large supercell, making it useful for large materials without compromising the environmental effect surrounding the impurity as is the case with the AIMPs approach. This approach does not require any assumptions to be made, thereby reducing one source of uncertainty.

Another constraint is the need for data to fine-tune parameters. Fore example, the DFT+U approach, which requires tuning the U parameter for each lanthanide to accurately simulate the location of 4f electrons in the band gap. Instead, we employed the HSE+SOC method combined with a supercell approach. This approach helped us pinpoint the location of the 4f ground states within the band gap, taking into account only the associated band gap of the host material. Consequently, we were able to simulate the doped system entirely using first principles, eliminating the need for any pre-existing data. Our findings were closely aligned with prior calculations and experimental data for Ce-doped LSO, despite the comparatively larger deviation (around 0.7 eV) from the empirical model developed through the Dorenbos model for Ce-doped YSO and LSO. Notably, our methodology showed the most consistent agreement with two distinct studies on Ce-doped LSO, both theoretically and experimentally. This outcome implies that our approach may be applicable to other lanthanides and host materials, even in the absence of significant prior knowledge.

In conclusion, our simpler approach, compared to wave function methods like AIMPs, could be considered as a reliable alternative for evaluating phosphors and identifying optical properties in laser materials, even without prior data. It holds promise for high-throughput phosphors applications, though its applicability to other Ln groups and host materials still awaits confirmation.

V. ACKNOWLEDGEMENTS

This work is supported by the Knut and Alice Wallenberg Foundation through grant no.: KAW-2016.0081. The simulations were performed using computational resources provided by the Swedish National Infrastructure at the NSC, Linköping University, and at the PDC, Royal Institute of Technology.

TABLE V. Transition energies, $4f \rightarrow 5d_i$. The procedure for the calculated value in this table is depicted in Figure 4. *This study: *.*

			$4f \rightarrow 5d_i$=1-5(eV)				
Ion	Site	Method	1	2	3	4	5
Ce^{3+}	Ce1	Exp.[6]	3.41	4.03	4.54	-	-
Ce^{3+}	Ce1	Exp.[46]	3.55	4.19	4.68	-	-
Ce^{3+}	Ce1	Exp.[47]	3.48	4.13	4.72	-	-
Ce^{3+}	Ce1	Exp_{avg}	3.48	4.11	4.65	-	-
Ce^{3+}	Ce1	CASPT2[8]	3.41	4.03	4.46	5.75	6.35
Ce^{3+}	Ce1	HSE*	3.511	4.45	4.64	4.92	5.21
Ce^{3+}	Ce1	HSE + SOC*	3.27	4.21	4.53	4.65	4.97
Ce^{3+}	Ce1	CASPT2+SOC[8]	3.53	4.16	4.59	5.89	6.49
Ce^{3+}	Ce2	Exp.[6]	3.30	3.80	-	-	-
Ce^{3+}	Ce2	Exp.[46]	3.32	3.78	4.79	-	-
Ce^{3+}	Ce2	Exp.[47]	3.31	3.79	4.78	-	-
Ce^{3+}	Ce2	Exp_{avg}	3.31	3.79	4.78	-	-
Ce^{3+}	Ce2	CASPT2[8]	3.44	3.64	3.91	6.29	7.09
Ce^{3+}	Ce2	HSE*	3.44	3.50	4.22	4.85	5.21
Ce^{3+}	Ce2	HSE + SOC*	3.30	3.43	4.15	4.79	5.09
Ce^{3+}	Ce2	CASPT2+SOC[8]	3.52	3.76	4.04	6.42	7.21

[1] G. Zhu, Z. Ci, Q. Wang, Y. Wen, S. Han, Y. Shi, S. Xin, and Y. Wang, J. Mater. Chem. C **1**, 4490 (2013).

[2] Y. Zhang, Y. Dong, J. Xu, and B. Wei, physica status solidi (a) **214**, 1600731 (2017).

[3] X. Qin, X. Liu, W. Huang, M. Bettinelli, and X. Liu, Chemical Reviews **117**, 4488 (2017), pMID: 28240879, https://doi.org/10.1021/acs.chemrev.6b00691.

[4] P. Dorenbos, Journal of Luminescence **135**, 93 (2013).

[5] A. H. Krumpel, E. van der Kolk, D. Zeelenberg, A. J. J. Bos, K. W. Krämer, and P. Dorenbos, Journal of Applied Physics **104**, 073505 (2008), https://aip.scitation.org/doi/pdf/10.1063/1.2955776.

[6] W. Chewpraditkul, C. Wanarak, T. Szczesniak, M. Moszynski, V. Jary, A. Beitlerova, and M. Nikl, Optical Materials **35**, 1679 (2013).

[7] A. Meijerink, W. J. Schipper, and G. Blasse, Journal of Physics D: Applied Physics **24**, 997 (1991).

[8] J. Wen, C.-K. Duan, L. Ning, Y. Huang, S. Zhan, J. Zhang, and M. Yin, The Journal of Physical Chemistry A **118**, 4988 (2014), pMID: 24953347, https://doi.org/10.1021/jp5050207.

[9] Z. Barandiarán and L. Seijo, The Journal of Chemical Physics **89**, 5739 (1988), https://pubs.aip.org/aip/jcp/article-pdf/89/9/5739/9728017/5739_1_online.pdf.

[10] X. Zhou, H. Liu, Z. He, B. Chen, and J. Wu, Inorganic Chemistry **59**, 13144 (2020), pMID: 32865403, https://doi.org/10.1021/acs.inorgchem.0c01430.

[11] R. A. Friesner, Proceedings of the National Academy of Sciences **102**, 6648 (2005).

[12] B. O. Roos, P. R. Taylor, and P. E. Sigbahn, Chemical Physics **48**, 157 (1980).

[13] E. Runge and E. K. U. Gross, Phys. Rev. Lett. **52**, 997 (1984).

[14] C. E. Dreyer, A. Alkauskas, J. L. Lyons, A. Janotti, and C. G. Van de Walle, Annual Review of Materials Research **48**, 1 (2018), https://doi.org/10.1146/annurev-matsci-070317-124453.

[15] G. Onida, L. Reining, and A. Rubio, Rev. Mod. Phys. **74**, 601 (2002).

[16] Y. Jia, A. Miglio, S. Poncé, X. Gonze, and M. Mikami, Phys. Rev. B **93**, 155111 (2016).

[17] Y. Jia, A. Miglio, S. Poncé, M. Mikami, and X. Gonze, Phys. Rev. B **96**, 125132 (2017).

[18] B. Kaduk, T. Kowalczyk, and T. Van Voorhis, Chemical Reviews **112**, 321 (2012), pMID: 22077560, https://doi.org/10.1021/cr200148b.

[19] A. Canning, A. Chaudhry, R. Boutchko, and N. Grønbech-Jensen, Phys. Rev. B **83**, 125115 (2011).

[20] J. Cai, W. Jing, J. Cheng, Y. Zhang, Y. Chen, M. Yin, Y.-Y. Yeung, and C.-K. Duan, Phys. Rev. B **99**, 125107 (2019).

[21] J. Heyd and G. E. Scuseria, The Journal of Chemical Physics **121**, 1187 (2004), https://pubs.aip.org/aip/jcp/article-pdf/121/3/1187/10861621/1187_1_online.pdf.

[22] R. Gillen, S. J. Clark, and J. Robertson, Phys. Rev. B **87**, 125116 (2013).

[23] A. Mirzai, A. Ahadi, S. Melin, and P. Olsson, Mechanics of Materials **154**, 103739 (2021).

[24] S. Saha, P. S. Chowdhury, and A. Patra, The Journal of Physical Chemistry B **109**, 2699 (2005), pMID: 16851277, https://doi.org/10.1021/jp0462106.

[25] G. Kresse and J. Furthmüller, Computational Materials Science **6**, 15 (1996).

[26] P. E. Blöchl, Physical Review B **50**, 17953 (1994).

[27] J. P. Perdew, K. Burke, and M. Ernzerhof, Phys. Rev. Lett. **77**, 3865 (1996).

[28] P. E. Blöchl, O. Jepsen, and O. K. Andersen, Phys. Rev. B **49**, 16223 (1994).

[29] M. Weissbluth, *Atoms and molecules* (Elsevier, 2012).

[30] S. Steiner, S. Khmelevskyi, M. Marsmann, and G. Kresse, Phys. Rev. B **93**, 224425 (2016).
[31] J. Hafner, Journal of Computational Chemistry **29**, 2044 (2008), https://onlinelibrary.wiley.com/doi/pdf/10.1002/jcc.21057.
[32] R. Stowasser and R. Hoffmann, Journal of the American Chemical Society **121**, 3414 (1999), https://doi.org/10.1021/ja9826892.
[33] A. Savin, C. Umrigar, and X. Gonze, Chemical Physics Letters **288**, 391 (1998).
[34] J. Coon, R. DeWames, and C. Loyd, Journal of Molecular Spectroscopy **8**, 285 (1962).
[35] L. Muresan, Y. Karabulut, A. Cadis, I. Perhaita, A. Canimoglu, J. Garcia Guinea, L. Barbu Tudoran, D. Silipas, M. Ayvacikli, and N. Can, Journal of Alloys and Compounds **658**, 356 (2016).
[36] X. Zhang, L. Zhou, Q. Pang, J. Shi, and M. Gong, The Journal of Physical Chemistry C **118**, 7591 (2014), https://doi.org/10.1021/jp412702g.
[37] J. Franck and E. G. Dymond, Trans. Faraday Soc. **21**, 536 (1926).
[38] E. Condon, Phys. Rev. **28**, 1182 (1926).
[39] J. Su, F. Wei, W. H. E. Schwarz, and J. Li, The Journal of Physical Chemistry A **116**, 12299 (2012), pMID: 23148711, https://doi.org/10.1021/jp305035y.
[40] H. N. Russell and F. A. Saunders, The Astrophysical Journal **61**, 38 (1925).
[41] Y. Jia, A. Miglio, M. Mikami, and X. Gonze, Phys. Rev. Mater. **2**, 125202 (2018).
[42] L. Ning, L. Lin, L. Li, C. Wu, C.-k. Duan, Y. Zhang, and L. Seijo, J. Mater. Chem. **22**, 13723 (2012).
[43] A. Vedda, M. Nikl, M. Fasoli, E. Mihokova, J. Pejchal, M. Dusek, G. Ren, C. R. Stanek, K. J. McClellan, and D. D. Byler, Phys. Rev. B **78**, 195123 (2008).
[44] P. Dorenbos, Phys. Rev. B **85**, 165107 (2012).
[45] E. van der Kolk, P. Dorenbos, C. W. E. van Eijk, S. A. Basun, G. F. Imbusch, and W. M. Yen, Phys. Rev. B **71**, 165120 (2005).
[46] V. Jary, A. Krasnikov, M. Nikl, and S. Zazubovich, physica status solidi (b) **252**, 274 (2015), https://onlinelibrary.wiley.com/doi/pdf/10.1002/pssb.201451234.
[47] V. Babin, V. Laguta, M. Nikl, J. Pejchal, A. Yoshikawa, and S. Zazubovich, Optical Materials **103**, 109832 (2020).